

Preliminary Results on the Structural Significance of Alkali-Silica Reaction in Massive Reinforced Concrete Structures



Victor Saouma
Mohammad Hariri-Ardebili
Wiwat Puatatsananon
Yann Le Pape

October 2014

DOCUMENT AVAILABILITY

Reports produced after January 1, 1996, are generally available free via US Department of Energy (DOE) SciTech Connect.

Website: <http://www.osti.gov/scitech/>

Reports produced before January 1, 1996, may be purchased by members of the public from the following source:

National Technical Information Service
5285 Port Royal Road
Springfield, VA 22161
Telephone: 703-605-6000 (1-800-553-6847)
TDD: 703-487-4639
Fax: 703-605-6900
E-mail: info@ntis.fedworld.gov
Website: <http://www.ntis.gov/help/ordermethods.aspx>

Reports are available to DOE employees, DOE contractors, Energy Technology Data Exchange representatives, and International Nuclear Information System representatives from the following source:

Office of Scientific and Technical Information
PO Box 62
Oak Ridge, TN 37831
Telephone: 865-576-8401
Fax: 865-576-5728
E-mail: report@osti.gov
Website: <http://www.osti.gov/contact.html>

This report was prepared as an account of work sponsored by an agency of the United States Government. Neither the United States Government nor any agency thereof, nor any of their employees, makes any warranty, express or implied, or assumes any legal liability or responsibility for the accuracy, completeness, or usefulness of any information, apparatus, product, or process disclosed, or represents that its use would not infringe privately owned rights. Reference herein to any specific commercial product, process, or service by trade name, trademark, manufacturer, or otherwise, does not necessarily constitute or imply its endorsement, recommendation, or favoring by the United States Government or any agency thereof. The views and opinions of authors expressed herein do not necessarily state or reflect those of the United States Government or any agency thereof.

Light Water Reactor Sustainability Program

Preliminary Results on the Alkali-Silica Reaction in Massive Reinforced Concrete Structures: Numerical Simulations of Coupled Moisture Transport and Heat Transfer and Structural Significance of Internal Expansion

Victor Saouma ¹
Mohammad Hariri-Ardebili ¹
Wiwat Puatatsananon ¹
Yann Le Pape

October 2014

¹ University of Colorado, Boulder CO 80309-0428

OAK RIDGE NATIONAL LABORATORY
P.O. Box 2008
Oak Ridge, Tennessee 37831-6285
managed by
UT-Battelle, LLC
for the
US DEPARTMENT OF ENERGY
under contract DE-AC05-00OR22725

CONTENTS

	Page
LIST OF FIGURES	vii
LIST OF TABLES	ix
1 COUPLED THERMAL/MOISTURE DIFFUSION	3
1.1 Material Formulation	3
1.1.1 Heat Diffusion	4
1.1.1.1 Governing Differential Equation	4
1.1.1.2 Thermal Conductivity	4
1.1.1.3 Thermal Capacity	5
1.1.1.4 Boundary Conditions	7
1.1.2 Moisture Diffusion	10
1.1.2.1 Moisture Capacity	11
1.1.2.1.1 Adsorption Isotherm	12
1.1.2.1.2 Moisture Capacity	14
1.1.2.2 Moisture Diffusivity	15
1.1.2.3 Final Algorithm for Moisture Diffusion into Concrete	17
1.1.3 Coupled Heat Transfer and Moisture Diffusion Analysis	17
1.2 Finite Difference Implementation	23
1.2.1 Discretization	24
1.2.1.1 Linear Parabolic Differential Equation	24
1.2.1.2 Nonlinear Parabolic Partial Differential Equation	24
1.2.2 Boundary Conditions	27
1.2.2.1 No flux Boundary Condition	28
1.2.2.2 Concentration Boundary Condition	28
1.2.2.3 Nonlinear Boundary Condition	28
1.2.3 Material Models	29
1.2.3.1 Linear parabolic partial differential equation	29
1.2.3.2 Nonlinear parabolic partial differential equation	31
1.2.4 Problem Formulation	31
1.2.4.1 Heat Transfer Analysis	32
1.2.4.2 Heat Transfer and Moisture Diffusion Analysis	32
1.2.4.3 Coupled Heat Transfer and Moisture Diffusion Analysis	33
1.3 Problem Validation	39
1.3.1 Validation case 1: 2D Transient Heat Conduction and Convection	39
1.3.1.1 Problem Description	39
1.3.1.2 Numerical Solution	39

1.3.2	Validation case 2: 2D Transient Heat Conduction, Convection and Surface Irradiation	40
1.3.2.1	Problem Description	40
1.3.2.2	Numerical Solution	41
1.3.3	Validation case 3: Coupled Heat and Moisture Diffusion Analysis Model	41
1.3.3.1	Problem Description	41
1.3.3.2	Numerical Solution	42
1.4	USER'S MANUAL	49
1.4.1	Program Operation	49
1.4.2	Input File Preparation	49
1.4.2.1	Sheet 1: Input	52
1.4.2.2	Sheet 2: Define b.c.	53
1.4.2.3	Sheet 3: Xi's Model	53
1.4.2.4	Sheet 4: Mensi's Model	53
1.4.2.5	Sheet 5: Bazant's Model	53
1.4.2.6	Sheet 6: Experimental Result T	53
1.4.2.7	Sheet 7: Experimental Result H	56
1.4.2.8	Sheet 8: Output and Plot	56
1.4.3	Output	56
1.4.3.1	Output files	56
1.4.3.2	Matlab plots	56
1.4.3.3	Figure files	61
2	FINITE ELEMENT SIMULATIONS OF ASR EXPANSION	62
2.1	Introduction	62
2.2	Case Study I: RC Panel	62
2.2.1	Material Properties	63
2.2.1.1	Concrete panel properties	64
2.2.1.2	Cushion ring properties	65
2.2.1.3	Steel rebar properties	65
2.2.1.4	ASR model properties	66
2.2.2	Structural Assessment of the RC Panel	70
2.2.2.1	Model P1	72
2.2.2.2	Model P2	73
2.2.2.3	Model P3	74
2.2.2.4	Model P4	75
2.2.2.5	Summary and Observations	77
2.3	Case Study II: Bending Beam	79
2.3.1	Material Properties	79
2.3.1.1	Concrete properties	80
2.3.1.2	Steel properties	81
2.3.1.3	ASR model properties	81
2.3.2	Assessment of Beam	82
2.3.2.1	Model B1	82
2.3.2.2	Model B2	86
2.3.2.3	Model B3	89
2.3.2.4	Model B4	92

2.3.2.5	Model B5	92
2.3.2.6	Model B6	93
2.3.2.7	Model B7	97
2.3.2.8	Observations	100

LIST OF FIGURES

Figures	Page
1.1 Thermal Conductivity of Concrete	6
1.2 Thermal Capacity of Concrete	8
1.3 Heat Transfer Analysis in Concrete	9
1.4 Heat Transfer Analysis in Concrete	11
1.5 Effect of the water to cement ratio on the moisture capacity, (Xi, Bažant, Molina and Jennings 1994)	14
1.6 Molecular Diffusion in terms of Humidity	15
1.7 Surface Diffusion	16
1.8 Algorithm for moisture diffusion analysis	18
1.9 Moisture Diffusivity of Concrete	21
1.10 Coupling between moisture and thermal diffusion models	22
1.11 Tridiagonal Matrix	25
1.12 ADI Method	26
1.13 Discretization of 2D Nonlinear Parabolic Partial Differential Equation using ADI Method and Iteration Using Old Value Method	27
1.14 The heterogeneous model for computing the diffusivity between two nodes which have different material's properties.	30
1.15 Algorithms of Heat Transfer Analysis	32
1.16 Flowchart of Heat Transfer+Moisture Diffusion Analysis	33
1.17 Discretization of 2D Moisture Diffusion Equation using ADI Method	34
1.18 Determination of $\frac{\partial H}{\partial W}(H)$	35
1.19 Determination of Humidity Diffusivity D_h	36
1.20 Numerical solution of the coupled heat/moisture diffusion	37
1.21 Algorithm for Coupled Heat and Moisture Diffusion Analysis using ADI Method	38
1.22 Validation case 1: 2D Transient Heat Conduction and Convection	39
1.23 Temperature distribution of the ceramic strip at a time 12 seconds	40
1.24 Validation case 2: 2D Transient Heat Conduction, Convection and Surface Irradiation	41
1.25 General view of MAQBETH mock-up (left) and cylindrical steel reinforcement (right) (Ranc et al. 2003)	42
1.26 Geometrical characteristics of MAQBETH mock-up (concrete hollow cylinder) (a), schematic description of experimental conditions (b) (Ranc et al. 2003)	43
1.27 Scheme of axisymmetrical numerical model	44
1.28 Experimental and numerical profiles of temperature as a function of the distance from the left concrete surface at different times.	45

1.29	Experimental and numerical profiles of temperature as a function of the distance from the left concrete surface at different times.	46
1.30	Experimental and numerical profiles of relative humidity as a function of the distance from the left concrete surface at different times.	47
1.31	Experimental and numerical profiles of relative humidity as a function of the distance from the left concrete surface at different times.	48
1.32	How to run htmc code	50
1.33	Input.xls file	51
1.34	Sheet 2: Define b.c.	54
1.35	Sheet 6: Experimental Result of Temperature	55
1.36	Sheet 6: Experimental Result of Relative Humidity	57
1.37	Sheet 6: How to prepare the input for saving the result at specified time step in Sheet 8: Output and Plot	58
1.38	Example of the output files generated htmc	59
1.39	Example of the Matlab plots generated by htmc code	60
2.1	Schematic view of the actual NPP, its idealized cylinder, and the cutted segment	62
2.2	General view of the RC panel	63
2.3	Elevation view of panel in x-z plane	63
2.4	Plane view of the test setup at UTK	64
2.5	Concrete cushion ring for the test at UTK	64
2.6	Design chart for tensile strength adopted from Raphael (1984)	66
2.7	Experimental test by Multon et al.; specimens kept in air at 100% RH and 38°C	69
2.8	Fitted curve to the data points based on measurement in parallel direction	69
2.9	Fitted curve to the data points based on measurement in perpendicular direction	69
2.10	Comparison of expansion curves with different asymptotic strains and same latency and characteristics times	70
2.11	3D finite element model of the RC panel	71
2.12	3D finite element model of the reinforcement for panel	71
2.13	Comparison of the deformed and un-deformed shapes of the panel	71
2.14	Spatial location of index points and layers of the panel	72
2.15	Response of model P1 at Index-1 (blue dotted line) and Index-2 (solid red line)	73
2.16	Response of model P2 at Index-1 (blue dotted line) and Index-2 (solid red line)	74
2.17	Response of model P3 at Index-1 (blue dotted line) and Index-2 (solid red line)	75
2.18	Non-concurrent maximum and minimum stresses in rebars for model P3	76
2.19	Stress at the most critical rebars in x and y directions for model P3	76
2.20	Response of model P4 at Index-1 (blue dotted line) and Index-2 (solid red line)	77
2.21	Non-concurrent maximum and minimum stresses in rebars for model P4	78
2.22	General view, dimensions and boundary condition of the three-point bending beam	79
2.23	Reinforcements in the beam, y-z plan view	80
2.24	Reinforcements in the beam, x-z plan view	80
2.25	Different steps towards shear test on ASR-affected beam	83
2.26	3D finite element model of the beam	83
2.27	3D finite element model of the rebars in beam	84
2.28	3D finite element model of the half beam with extra support beam	84
2.29	Spatial location of index points and index rebars in the beam model	84

2.30	Simplified analytical solution for beam	85
2.31	Finite element response of the beam B1 for two load combinations	85
2.32	Response of the beam B1 at three index points; Incremental displacement	86
2.33	Stress at the two index longitudinal rebars for half-beam B1; Under incremental displacement	86
2.34	Response of the beam B2 at three index points; Under ASR expansion	87
2.35	Response of ASR-affected beam B2 at three index points; Under incremental displacement	88
2.36	Stress at the two index longitudinal rebars for beam B2; Under ASR expansion	88
2.37	Stress at the two index longitudinal rebars for beam B2; Under incremental displacement	89
2.38	Deformed shape of the beam at the end of ASR expansion, model B2	89
2.39	Response of the beam B3 at three index points; Under ASR expansion	90
2.40	Response of ASR-affected beam B3 at three index points; Under incremental displacement	90
2.41	Stress at the two index longitudinal rebars for beam B3; Under ASR expansion	91
2.42	Stress at the two index longitudinal rebars for beam B3; Under incremental displacement	91
2.43	Response of the beam B4 at three index points; Incremental load (traction)	92
2.44	Stress at the two index longitudinal rebars for half-beam B4; Under incremental load (traction)	93
2.45	Progressive failure in beam Model B4 under incremental load (traction)	94
2.46	Response of the beam B5 at three index points; Incremental load (traction)	95
2.47	Stress at the two index longitudinal rebars for half-beam B5; Under incremental load (traction)	95
2.48	Degradation of Young's modulus and tensile strength with ASR expansion	95
2.49	Response of the beam B6 at three index points; Under ASR expansion	96
2.50	Response of ASR-affected beam B6 at three index points; Under incremental load (traction)	96
2.51	Stress at the two index longitudinal rebars for beam B6; Under ASR expansion	97
2.52	Stress at the two index longitudinal rebars for beam B6; Under incremental load	97
2.53	Response of the beam B7 at three index points; Under ASR expansion	98
2.54	Response of ASR-affected beam B7 at three index points; Under incremental load (traction)	98
2.55	Stress at the two index longitudinal rebars for beam B7; Under ASR expansion	99
2.56	Stress at the two index longitudinal rebars for beam B7; Under incremental load (traction)	99
2.57	Load-displacement curves for nonlinear beam models	100
2.58	Stress distribution in bottom rebar for nonlinear models	101
2.59	Stress distribution in top rebar for nonlinear models	101

LIST OF TABLES

Tables	Page
1.1 V_{ct} and N_{ct} for different type of concrete	12
1.2 V_{ag} of various pore structure of aggregate	13
1.3 n_{ag} of various pore structure of aggregate	13
1.4 Governing Differential Equations	23
1.5 Diffusion Coefficients and Boundary Conditions in Each Diffusion Process	23
1.6 Variable and Coefficients of Diffusion Process	25
1.7 Validation Summary of Case 1	40
1.8 Validation Summary of Case 2	41
1.9 Parameter used in the moisture diffusivity of concrete model proposed by Bazant and Najjar (1972)	42
1.10 List of the m-file which read the specific sheet in the <code>input.xls</code> file	52
2.1 General characteristics of concrete panel	64
2.2 Concrete mixture for the RC panel.	65
2.3 General characteristics of rebar #11	66
2.4 General parameters of the ASR model used in RC panel	67
2.5 Concrete mixture models used in the literature for AAR and ASR tests	68
2.6 Different types of the models for the panel	70
2.7 Comparison of the panel models based on linear elastic material	78
2.8 General characteristics of concrete for beam	80
2.9 General characteristics of rebar #4	81
2.10 General parameters of the ASR model for beam	81
2.11 Different types of the models for the beam	82

EXECUTIVE SUMMARY

Cases of alkali-silica reaction (ASR) in nuclear generating stations have been reported in Japan (Takatura et al. 2005) and in Canada at Gentilly 2 NPP (Tcherner and Aziz 2009). More recently, in the United States, the NRC issued Information Notice (IN) 2011-20, “Concrete Degradation by Alkali Silica Reaction”, on November 18, 2011, to provide the industry with information related to the ASR identified at Seabrook. Considering that US commercial reactors in operation enter the age within which ASR degradation can be visually detected and that numerous non nuclear industries (transportation, energy production) have already experienced ASR in a large majority of the States, the susceptibility and significance of ASR for nuclear concrete structures must be addressed in the perspective of license renewal and LTO beyond 60 years.

Because of exposure, dimension and reinforcement ratio differences, the evaluation of the structural significance of ASR on affected concrete in nuclear power plants can not be fully transposed from the experience gained on transportation infrastructure or concrete dams. Temperature and moisture content vary significantly in nuclear plant concrete components: For example, concrete located in the vicinity of the reactor is affected by relatively high temperature, gamma and neutron irradiation and is or is not subjected to drying depending on the presence of a liner or a membrane, while below grade retaining structures are subjected to moderate temperature but may be susceptible to ground water ingress. In addition, the absence of shear reinforcement (i.e., in the through thickness direction), in class I safety-related nuclear structures, is permitted by ACI 318 (Building Code Requirements for Reinforced Concrete). It results in an absence of confinement that favors out-of-plane expansion of ASR-affected structures. The shear bearing capacity relies primarily on plain concrete. The residual shear capacity (accidental design scenario) of potentially ASR-affected structures like the biological shield building, the containment building and the fuel handling building will depend on two competitive mechanisms: (1) the extent of the micro-cracking easing the propagation of shear fracture and (2) the relative in-plane confinement-induced compression in the direction of the reinforcement potentially limiting the propagation of such fracturing. While this question remains unresolved, further investigation is needed to determine the potential impact of ASR on the structural resistance of nuclear structures. Also, accessibility to the potential ASR-affected areas in safety-related concrete structures is by essence limited and ASR may develop primarily in the bulk of the structures because of existing humidity and temperature profiles. The need to develop reliable condition assessment and subsequent prognosis methodologies is imminent.

This report presents the first steps toward the numerical modeling of ASR affected structures in nuclear power plant. It is divided in two separate parts.

The first part deals with coupled moisture transport and head transfer in concrete. A fully coupled scheme is developed following the approach proposed by Bazant and Thonguthai (1978), Bažant and Thonguthai (1979). The finite difference implementation is described in details, and three validation problems are presented: In particular, the modeling of CEA concrete mockup MAQBETH (large scale heated reinforced concrete experiment) is analyzed and modeled.

The second part is devoted to the modeling of ASR-affected structural under iso-thermal and iso-hygric conditions. The purpose of the analysis is to study the effects of lateral constraints on the development of ASR swelling and damage, and subsequently, on the residual bearing capacity of the aged structures. Linear and nonlinear models developed by Saouma and Perotti (2006) are tested. Two structures of interest are tested: a reinforced concrete panel similar initially designed by the University of Tennessee at Knoxville and large-scale bridge girder beam similar to those tested at the University of Texas at Austin. Different boundary conditions are tested providing insightful results for understanding the behavior of reinforced concrete structures in nuclear power plants.

1 COUPLED THERMAL/MOISTURE DIFFUSION

Concrete is a multiphase materials. Its porous network made of capillary pores is filled partly with an ionic solution and partly with gas. The degree of saturation in the porosity varies over time. At early age, water consumption results from the chemical reactions with anhydrous cement to form new hydrates; Later, the materials interacts with its environment: moisture transport resulting from wetting, drying or wetting-drying cycles causes the evolution of the internal moisture content. Moisture transport in concrete being a rather slow process, the moisture content in massive concrete structures is rarely uniform within such structures.

Concrete mechanical properties (strength, elasticity) and dimensional change (shrinkage, creep, thermal expansion) are highly dependent on the internal humidity and the temperature of the materials. As mentioned before, temperature and moisture transient spatial fields are generally not uniform in massive structures. Moisture transport characteristic time is comparable to the operation duration or the designed life: i.e. several decades. It takes several years to bring an ordinary concrete standard cylinder to moisture equilibrium in a controlled environment at 20°C and 50% relative humidity; A thick wall of about 3-4 feet thick made of the same material would reach the equilibrium after more than a century. Temperature also affects concrete properties and influence greatly the kinetics of moisture transport. Hence, any concrete structural analysis should begin with a correct description of the temperature and moisture content in time and in space before evaluating the stress-strain fields.

Inside the containment building, temperature is generally above 20°C and concrete can be exposed to long-term steady-state temperatures. Irradiation-induced energy deposition can also be a source of heat generation in concrete. The present American Society of Mechanical Engineers Pressure Vessel and Piping Code (ASME Code) limits the temperature of 65°C with local exception up to about 90°C. Other class-I safety related structures may be subjected to lower temperatures. Thus, coupled moisture transport and heat transfer cannot be ignored in nuclear structures. This chapter addresses the part of the project focusing on the nonlinear coupled heat-moisture diffusion in concrete up to temperatures of about 200°C. It does not explicitly addresses ASR expansion, it simply seeks to develop a numerical model that will predict both temperature and moisture, key input parameters for a subsequent ASR expansion.

1.1 MATERIAL FORMULATION

This section addresses the material formulation which forms the underpinning of the developed finite difference code presented in the next section. Heat transfer and moisture transport are addressed separately before being coupled.

1.1.1 HEAT DIFFUSION

1.1.1.1 Governing Differential Equation

The governing 2D-heat transfer differential equation is given by

$$\frac{\partial}{\partial x} \left(k(x, y) \frac{\partial T}{\partial x} \right) + \frac{\partial}{\partial y} \left(k(x, y) \frac{\partial T}{\partial y} \right) + Q = \rho(x, y) C(x, y) \frac{\partial T}{\partial t} \quad (1.1)$$

where

k thermal conductivity of concrete in $W/m^{\circ}C$

T temperature in $^{\circ}C$

t time in *sec*

Q rate of heat per unit volume generated within the body W/m^3

ρC thermal capacity of concrete

ρ density in kg/m^3

C specific heat of concrete in $J/kg^{\circ}C$

Given that heat transfers occurs through

1. solar radiation;
2. heat convection caused by wind;
3. heat irradiation between concrete surface and environment;

Each one of them will be separately reviewed for concrete as boundary conditions. in the following, mathematical relations given by codes or from the literature to calculate the thermal properties of concrete are reported. These relation shall not replace data obtained from the experimental characterization of a specific concrete when available.

1.1.1.2 Thermal Conductivity

ASCE The American Society of Civil Engineers has proposed the relationships for concrete thermal conductivity at high-temperature for normal-strength concrete as follows ASCE (1992); For siliceous aggregate concrete,

$$k = \begin{cases} -0.000625T + 1.5 & \text{for } 20^{\circ}C \leq T \leq 800^{\circ}C \\ 1.0 & \text{for } T > 800^{\circ}C \end{cases} \quad (1.2)$$

For carbonate aggregate concrete,

$$k = \begin{cases} 1.355 & \text{for } 20^{\circ}C \leq T \leq 293^{\circ}C \\ -0.001241T + 1.7162 & \text{for } T > 293^{\circ}C \end{cases} \quad (1.3)$$

Kodur et al. (2004) The relationship proposed by ASCE (1992) has been modified for high-strength concrete by Kodur et al. (2004). For siliceous aggregate concrete,

$$k = 0.85(2 - 0.0011T) \text{ for } 20^{\circ}C \leq T \leq 1000^{\circ}C \quad (1.4)$$

and for carbonate aggregate concrete,

$$k = \begin{cases} 0.85(2 - 0.0013T) & \text{for } 20^{\circ}C \leq T \leq 300^{\circ}C \\ 0.85(2.21 - 0.002T) & \text{for } T > 300^{\circ}C \end{cases} \quad (1.5)$$

Eurocode (2004) has developed relationships for both normal- and high-strength concretes, and for all types of aggregates Eurocode (2004) as follows;

Upper limit :

$$k = 2 - 0.2451 \left(\frac{T}{100} \right) + 0.0107 \left(\frac{T}{100} \right)^2 \quad \text{for } 20^\circ C \leq T \leq 1200^\circ C \quad (1.6)$$

Lower limit :

$$k = 1.36 - 0.136 \left(\frac{T}{100} \right) + 0.0057 \left(\frac{T}{100} \right)^2 \quad \text{for } 20^\circ C \leq T \leq 1200^\circ C \quad (1.7)$$

Kim (2003) The thermal conductivity of concrete k adopted is the one of Kim et al. (2003) (in $W/m^\circ C$)

$$k = \lambda_H \lambda_{S/A} \lambda_T \lambda_{AG} k_{ref} \quad (1.8)$$

$$\lambda_H = 0.9 [1.62 - 1.54 (w/c)] + 0.2H \quad (1.9)$$

$$\lambda_{S/A} = 0.86 + 0.36 (S/A) \quad (1.10)$$

$$\lambda_T = 1.05 - 0.0025T \quad (1.11)$$

$$\lambda_{AG} = 0.293 + 1.01AG \quad (1.12)$$

and

- H Relative humidity
- AG Aggregate volume aggregate
- S/A Fine aggregate fraction
- w/c Water to cement ratio
- T temperature

We can summarize the thermal conductivity of concrete used in Eq.1.51 in Fig. 1.1

1.1.1.3 Thermal Capacity

Thermal capacity of the concrete is the product of specific heat(C) and density of concrete (ρ).

ASCE (1992) The American Society of Civil Engineers has proposed the relationships for concrete thermal capacity at high-temperature for normal-strength concrete as follows ASCE (1992); For siliceous aggregate concrete, (ρC in $\frac{MJ}{m^3^\circ C}$)

$$\rho C = \begin{cases} 0.005T + 1.7 & \text{for } 20^\circ C \leq T \leq 200^\circ C \\ 2.7 & \text{for } 200^\circ C \leq T \leq 400^\circ C \\ 0.013T - 2.5 & \text{for } 400^\circ C \leq T \leq 500^\circ C \\ 10.5 - 0.013T & \text{for } 500^\circ C \leq T \leq 600^\circ C \\ 2.7 & \text{for } T > 600^\circ C \end{cases} \quad (1.13)$$

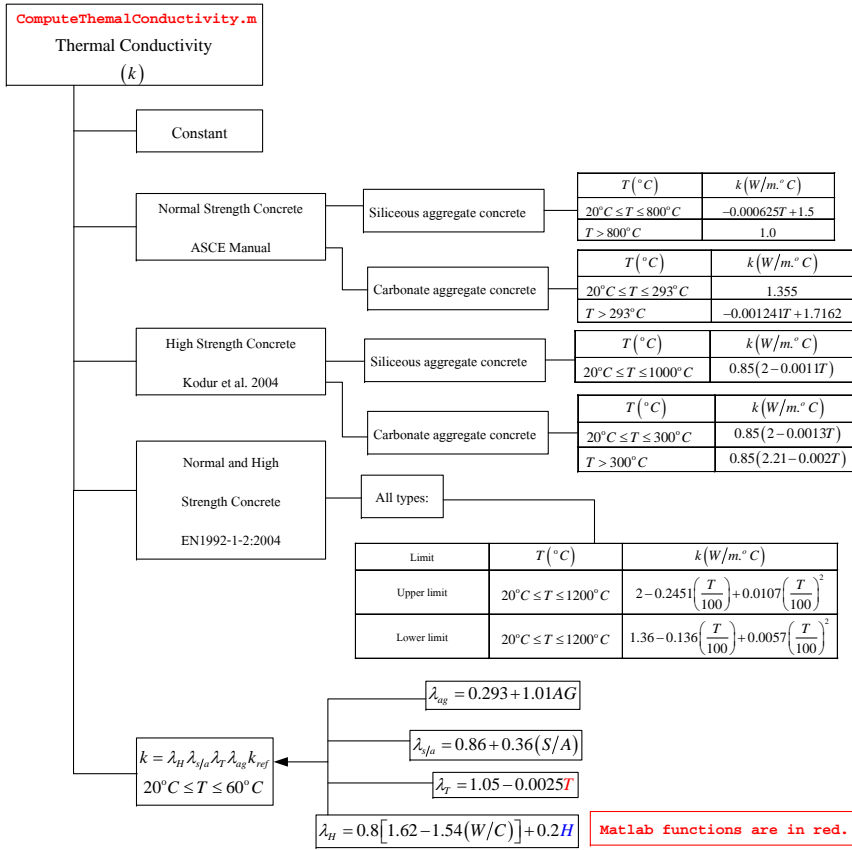


Fig. 1.1. Thermal Conductivity of Concrete

and for carbonate aggregate concrete, (ρC in $\frac{MJ}{m^3 \circ C}$)

$$\rho C = \begin{cases} 2.566 & \text{for } 20^\circ C \leq T \leq 400^\circ C \\ 0.1765T - 68.034 & \text{for } 400^\circ C \leq T \leq 410^\circ C \\ 25.00671 - 0.05043T & \text{for } 410^\circ C \leq T \leq 445^\circ C \\ 2.556 & \text{for } 445^\circ C \leq T \leq 500^\circ C \\ 0.01603T - 5.44881 & \text{for } 500^\circ C \leq T \leq 635^\circ C \\ 0.16635T - 100.90225 & \text{for } 635^\circ C \leq T \leq 715^\circ C \\ 176.07343 - 0.22103T & \text{for } 715^\circ C \leq T \leq 785^\circ C \\ 2.566 & \text{for } T > 785^\circ C \end{cases} \quad (1.14)$$

Kodur et al. (2004) The relationship proposed by ASCE (1992) has been modified for high-strength

concrete by Kodur et al. (2004). For siliceous aggregate concrete, (ρC in $\frac{MJ}{m^3 \cdot ^\circ C}$)

$$\rho C = \begin{cases} 0.005T + 1.7 & \text{for } 20^\circ C \leq T \leq 200^\circ C \\ 2.7 & \text{for } 200^\circ C \leq T \leq 400^\circ C \\ 0.013T - 2.5 & \text{for } 400^\circ C \leq T \leq 500^\circ C \\ 10.5 - 0.013T & \text{for } 500^\circ C \leq T \leq 600^\circ C \\ 2.7 & \text{for } 600^\circ C \leq T \leq 635^\circ C \end{cases} \quad (1.15)$$

and for carbonate aggregate concrete, (ρC in $\frac{MJ}{m^3 \cdot ^\circ C}$)

$$\rho C = \begin{cases} 2.45 & \text{for } 20^\circ C \leq T \leq 400^\circ C \\ 0.026T - 12.85 & \text{for } 400^\circ C \leq T \leq 475^\circ C \\ 0.0143T - 6.295 & \text{for } 475^\circ C \leq T \leq 650^\circ C \\ 0.1894T - 120.11 & \text{for } 650^\circ C \leq T \leq 735^\circ C \\ -0.263T + 212.4 & \text{for } 735^\circ C \leq T \leq 800^\circ C \\ 2.0 & \text{for } 800^\circ C \leq T \leq 1000^\circ C \end{cases} \quad (1.16)$$

Eurocode Eurocode has developed relationships for both normal- and high-strength concretes, and for all types of aggregates Eurocode (2004) as follows; The equation for density of concrete (ρ ($\frac{kg}{m^3}$)) is given by

$$\rho = \begin{cases} \rho_{ref} & \text{for } 20^\circ C \leq T \leq 115^\circ C \\ \rho_{ref} \left(1 - \frac{0.02(T-115)}{85} \right) & \text{for } 115^\circ C \leq T \leq 200^\circ C \\ \rho_{ref} \left(0.98 - \frac{0.03(T-200)}{200} \right) & \text{for } 200^\circ C \leq T \leq 400^\circ C \\ \rho_{ref} \left(0.95 - \frac{0.07(T-400)}{800} \right) & \text{for } 400^\circ C \leq T \leq 1200^\circ C \end{cases} \quad (1.17)$$

where ρ_{ref} is reference concrete density at $20^\circ C$ and the equation for specific heat of concrete (C ($\frac{J}{kg \cdot ^\circ C}$)) is given by

$$C = \begin{cases} 900 & \text{for } 20^\circ C \leq T \leq 100^\circ C \\ 900 + (T - 100) & \text{for } 100^\circ C \leq T \leq 200^\circ C \\ 1000 + \left(\frac{T-200}{2} \right) & \text{for } 200^\circ C \leq T \leq 400^\circ C \\ 1100 & \text{for } 400^\circ C \leq T \leq 1200^\circ C \end{cases} \quad (1.18)$$

We can summarize the thermal capacity of concrete used in Eq.1.51 as in Fig. 1.2. Finally, we can summarize the heat transfer analysis used in Eq.1.51 as in Fig. 1.3

1.1.1.4 Boundary Conditions

For the rate of heat transferred by the surrounding air to or from the concrete surface is the sum of the energy rates due to convection, solar radiation and surface irradiation as the follows:

Conduction: is governed by

$$q_c = q_a, \quad \text{at the boundary} \quad (1.19)$$

q_c is the rate of heat transfer by conduction which is defined by

$$q_c = -k \left(\frac{\partial T}{\partial x} n_x + \frac{\partial T}{\partial y} n_y \right) \quad (1.20)$$

where n_x and n_y are the direction cosine of the unit outward normal to the boundary surface.

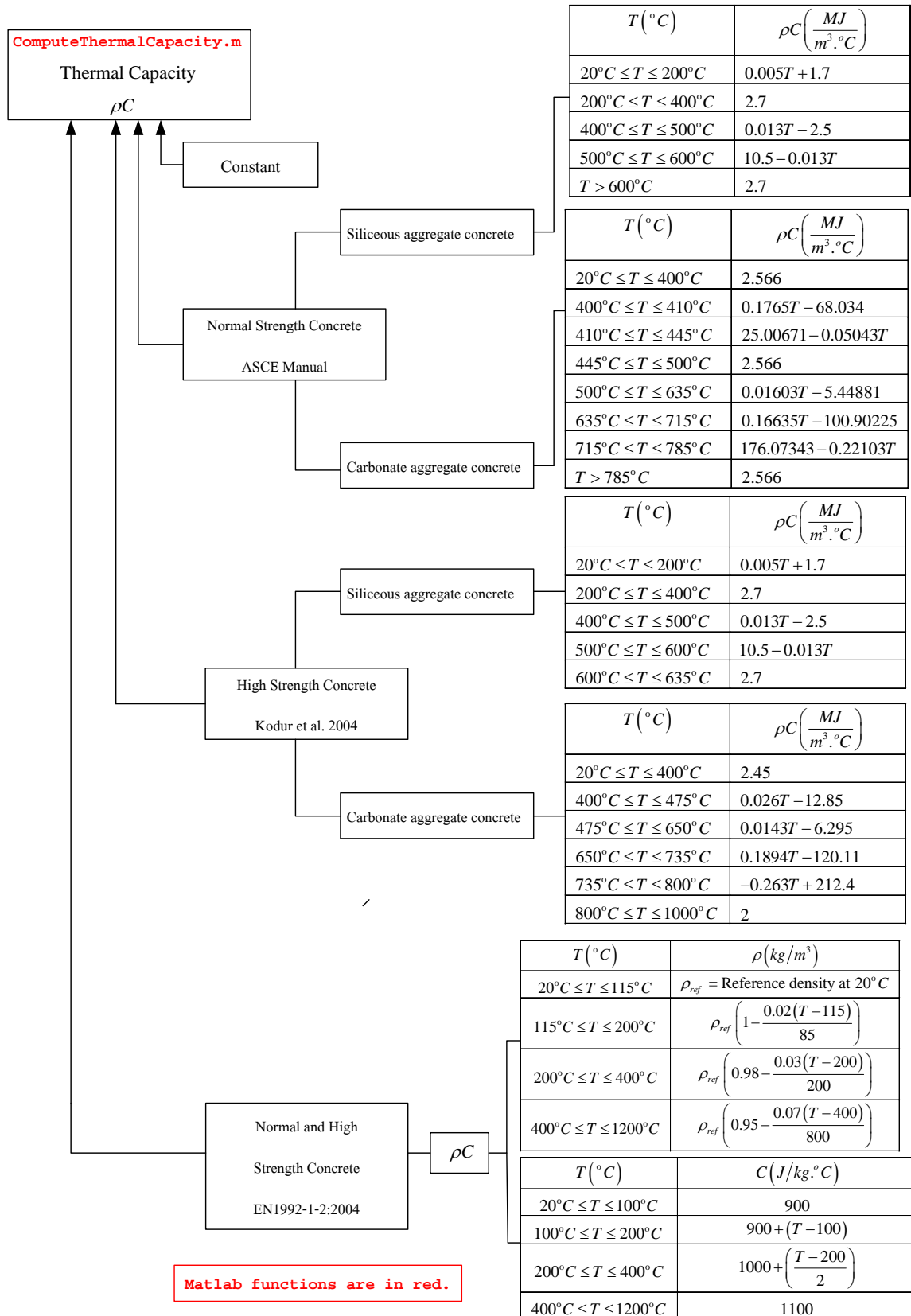


Fig. 1.2. Thermal Capacity of Concrete

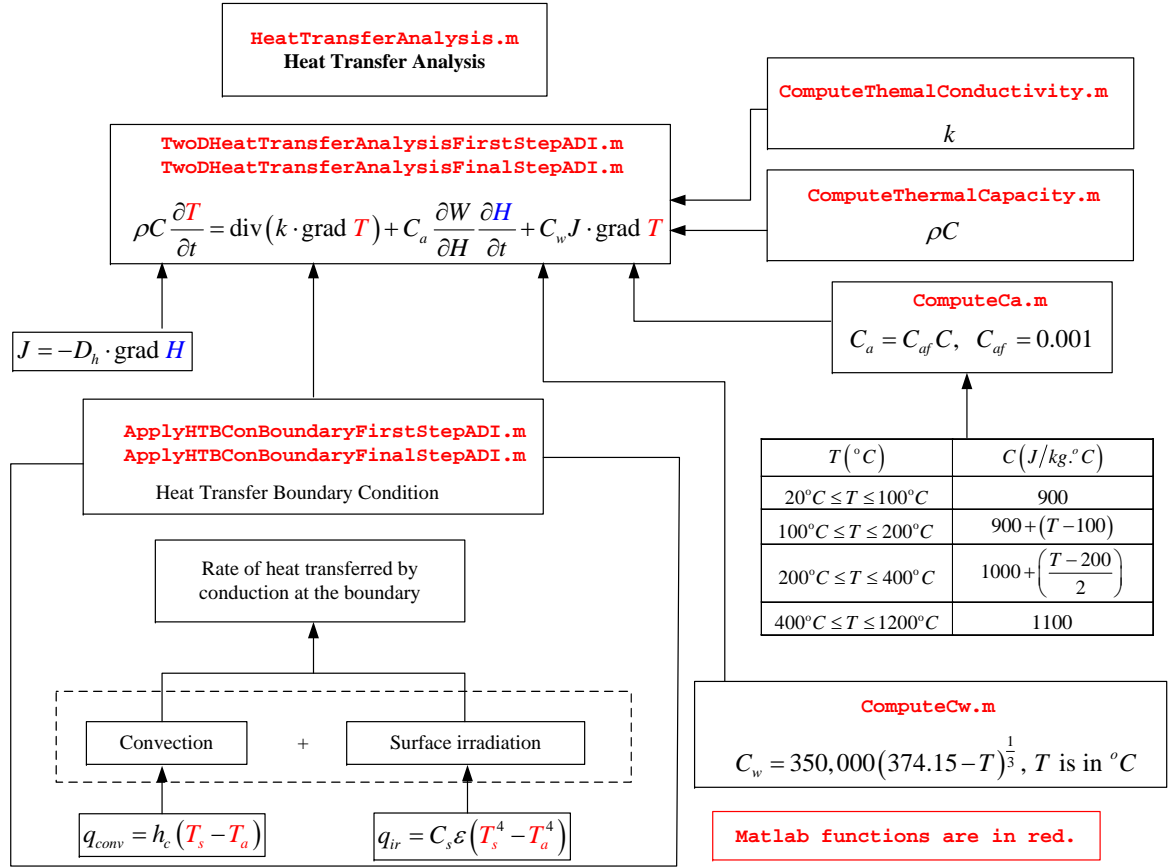


Fig. 1.3. Heat Transfer Analysis in Concrete

Convection Convection is the heat transfer due to the moving air contacts at the concrete surface at difference temperature. It is expressed by Newton's law of cooling as (Kreider and Rabl 1994):

$$q_{conv} = h_c(T_s - T_a) \quad (1.21)$$

where

- h_c convection coefficient $W/m^2 \cdot ^{\circ}C$
- T_s temperature of the concrete surface $^{\circ}C$
- T_a temperature of the surrounding air $^{\circ}C$

For the convection over the planes, the convection coefficient is a function of the length of the surface in the direction of the flow L and the wind speed v . It is given by (Kreider and Rabl 1994):

1. if $vL < 15 \text{ ft}^2/\text{s}$ or $1.4 \text{ m}^2/\text{s}$

$$h_c = 0.35 \left(\frac{v}{L} \right)^{1/2} \quad [\text{US unit}] \quad (1.22)$$

$$h_c = 2.0 \left(\frac{v}{L} \right)^{1/2} \quad [\text{SI unit}] \quad (1.23)$$

2. if $vL > 15 \text{ ft}^2/\text{s}$ or $1.4 \text{ m}^2/\text{s}$

$$h_c = 0.54 \left(\frac{v^4}{L} \right)^{1/5} \quad [\text{US unit}] \quad (1.24)$$

$$h_c = 6.2 \left(\frac{v^4}{L} \right)^{1/5} \quad [\text{SI unit}] \quad (1.25)$$

Thermal Irradiation : between the concrete surface and the surrounding air can be given by Stefan-Boltzman law as

$$q_{ir} = C_s \epsilon (T_s^4 - T_a^4) \quad (1.26)$$

where

C_s Stefan-Boltzman constant = $5.677 \times 10^{-8} \text{ W/m}^2 \text{ K}^4$

ϵ emissivity coefficient of concrete

T_s concrete surface temperature in *Kelvin*

T_a surrounding air temperature in *Kelvin*

Fig. 1.4 highlights the heat transfer procedure in the developed Matlab based code.

1.1.2 MOISTURE DIFFUSION

Many properties of concrete depend very strongly on the moisture content in the concrete. The study for moisture distribution in the concrete is very important, especially for the time-dependent analysis of the concrete, such as shrinkage, creep, fire resistance, and durability. To study the moisture diffusion, first, the moisture diffusion equation will be formulated, and then its parameters will be described separately. This section is adapted from Xi, Bažant and Jennings (1994) and Ababneh et al. (2002). Moisture flux may be expressed through two alternative formulations:

Gradient of water content:

$$J = -D_w \nabla(W_e) \quad (1.27)$$

$$\frac{\partial W}{\partial t} = \frac{\partial(W_e + W_n)}{\partial t} = -\text{div}(J) = \text{div}(D_w \nabla W_e) \quad (1.28)$$

Gradient of pore relative humidity:

$$J = -D_h \nabla(H) \quad (1.29)$$

$$\frac{\partial W}{\partial t} = \frac{\partial W}{\partial H} \frac{\partial H}{\partial t} = -\text{div}(J) = \text{div}(D_h \nabla H) \quad (1.30)$$

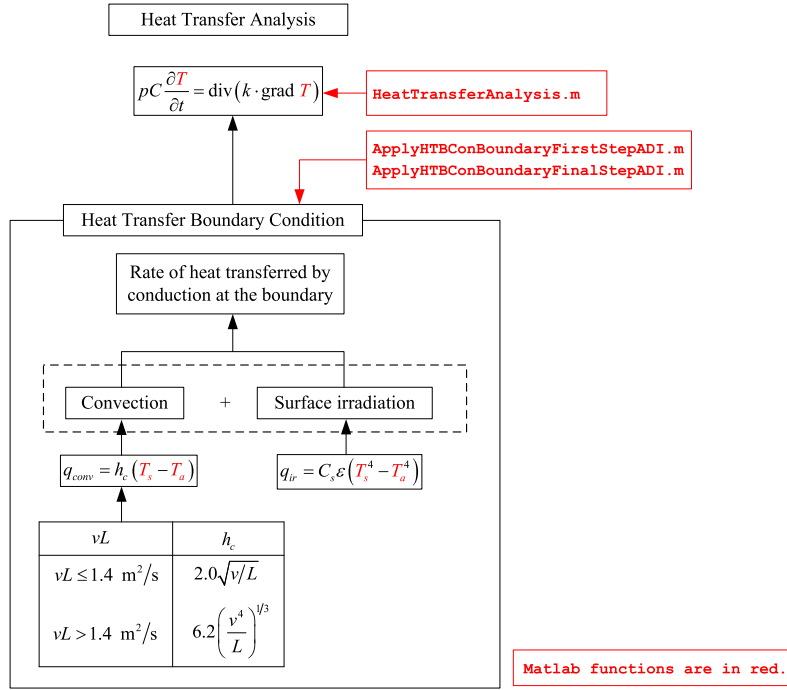


Fig. 1.4. Heat Transfer Analysis in Concrete

where

- H = Pore relative humidity
- W = Total water content (for unit volume of material)
- W_e = Evaporable water
- W_n = Non-evaporable or chemically bound water
- D_w = Moisture diffusivity
- D_h = Permeability or humidity diffusivity

Two material parameters must first be identified: a) Moisture capacity $\frac{\partial W}{\partial H}$ and Diffusivity D_h . Both parameters are expressed in terms of pore relative humidity H , thus Eq. 1.54 is nonlinear.

1.1.2.1 Moisture Capacity

The moisture capacity, $\frac{\partial W}{\partial H}$ is defined as the derivative of the total water content W with respect to the pore relative humidity H . For concrete, it can be determined based on the multiphase and multiscale model (Xi et al. 2000) where the concrete is considered to be a two phase material, aggregate representing one phase and cement paste representing another. It is given by (Ababneh et al. 2002)

$$\frac{\partial W}{\partial H} = f_{agg} \left(\frac{\partial W}{\partial H} \right)_{agg} + f_{cp} \left(\frac{\partial W}{\partial H} \right)_{cp} \quad (1.31)$$

where

- f_{agg} = weight percentages of the aggregate
 f_{cp} = weight percentages of the cement paste
 $\left(\frac{\partial W}{\partial H}\right)_{agg}$ = moisture capacity of aggregate
 $\left(\frac{\partial W}{\partial H}\right)_{cp}$ = moisture capacity of cement paste

The moisture capacity $\frac{\partial W}{\partial H}$ is a function of the total water content W and the pore relative humidity H , which will be defined later in section 1.1.2.1.2. The total water content at the constant temperature is called adsorption isotherm.

1.1.2.1.1 Adsorption Isotherm

In order to determine the adsorption isotherm we first need to evaluate

$$W = \frac{CkV_mH}{(1 - kH)[1 + (C - 1)kH]} \quad (1.32)$$

where

- $C = \exp\left(\frac{C_0}{T}\right)$, $C_0 = 855$
 $H = \frac{p}{p_s}$ where p_s is the pressure at saturation
 $T =$ Absolute temperature
 $W =$ Quantity of vapour absorbed at pressure p
 (grams of water/gram of cement)
 $V_m =$ Monolayer capacity: mass of adsorbate required to cover
 the adsorbant with a single molecular layer
 $k =$ Constant

which is defined in terms of V_m and k as follows:

Monolayer Capacity V_m has to be separately determined for cement past and aggregates.

Cement Paste is determined from

$$V_m = V_t(t)V_{wc}(w/c)V_{ct}(ct)V_T(T) \quad (1.33)$$

$$V_t(t) = \begin{cases} 0.068 - \frac{0.22}{t} & \text{for } t > 5 \text{ days} \\ V_t(5) & \text{if } t \leq 5 \text{ days} \end{cases} \quad (1.34)$$

$$V_{wc}(w/c) = \begin{cases} 0.85 + 0.45\frac{w}{c} & \text{for } 0.3 < w/c < 0.7 \\ V_{wc}(0.3) & \text{if } w/c \leq 0.3 \end{cases} \quad (1.35)$$

and $V_{ct}(ct)$ is given by Table 1.1, $V_T(T) = 1$ at room temperature.

Table 1.1. V_{ct} and N_{ct} for different type of concrete

	Concrete Type			
	1	2	3	4
V_{ct}	0.9	1.0	0.85	0.6
N_{ct}	1.1	1.0	1.15	1.5

Aggregates: (Xi 1995) is determined from

$$V_m = 0.00647V_{ag} \quad (1.36)$$

The monolayer capacity of aggregate depends on aggregates used. It can be determined based on the the pore structure of various aggregates as shown in Table 1.2

Table 1.2. V_{ag} of various pore structure of aggregate

Pore structure of aggregate	V_{ag}
dense	0.05-0.1
porous	0.1-0.04

Parameter k can be determined from the number of adsorped layers at the saturated state n . Again, we differentiate between cement paste and aggregates

Cement Paste from

$$n = N_t(t)N_{wc}(w/c)N_{ct}(ct)N_T(T) \quad (1.37)$$

$$N_t(t) = \begin{cases} 2.5 + \frac{15}{t_e} & \text{for } t > 5 \text{ days} \\ 5.5 & \text{if } t \leq 5 \text{ days} \end{cases} \quad (1.38)$$

$$N_{wc}(w/c) = \begin{cases} 0.33 + 2.2\frac{w}{c} & \text{for } 0.3 < w/c < 0.7 \\ N_{wc}(0.3) & \text{if } w/c \leq 0.3 \\ N_{wc}(0.7) & \text{if } w/c \geq 0.7 \end{cases} \quad (1.39)$$

$N_{ct}(ct)$ is given by Table 1.1, and $N_T(T) = 1$ at room temperature.

Aggregate (Xi 1995) from

$$n = 4.063n_{ag} \quad (1.40)$$

This parameter depends on aggregates used and can be determined based on the the pore structure of various aggregates as shown in Table 1.3

Table 1.3. n_{ag} of various pore structure of aggregate

Pore structure of aggregate	n_{ag}
dense	1.0-1.5
porous	1.7-2.0

Finally, k is determined from

$$k = \frac{\left(1 - \frac{1}{n}\right) C - 1}{C - 1} \quad (1.41)$$

1.1.2.1.2 Moisture Capacity

(Xi, Bažant, Molina and Jennings 1994) is the derivative of the moisture content W in Eq. 1.32 with respect to the pore relative humidity. As a result, we obtain

$$\frac{\partial W}{\partial H} = \frac{CkV_m + Wk[1 + (C - 1)kH] - Wk(1 - kH)(C - 1)}{(1 - kH)[1 + (C - 1)kH]} \quad (1.42)$$

From Fig. 1.5 we identify two points, first the moisture capacity drops, then it remains constant and finally

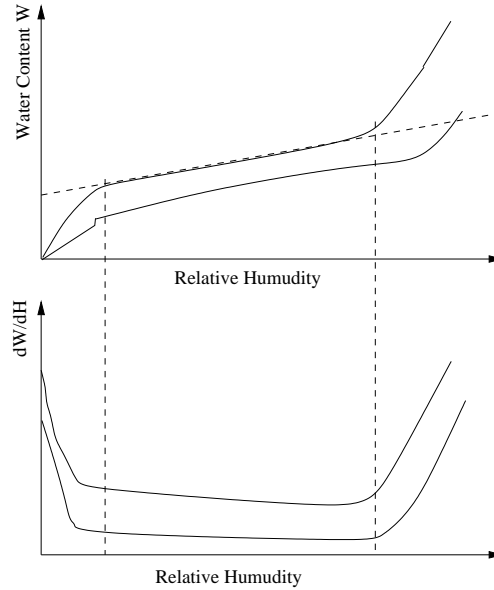


Fig. 1.5. Effect of the water to cement ratio on the moisture capacity, (Xi, Bažant, Molina and Jennings 1994)

it increases. The physical meaning of Fig. 1.5 can be explained as the follows.

1. At first point the adsorbent reaches its monolayer capacity, above which the moisture capacity does not decrease steeply with increasing H .
2. At the second point, it corresponds to initial point of capillary condensation where moisture capacity increases.

Cement Paste, $\left(\frac{\partial W}{\partial H}\right)_{cp}$ To determine the moisture capacity of cement paste used in eq. 1.31, n , k , V_m , and W of cement paste in Eq.1.37, 1.41, 1.33 and 1.32, respectively are first determined and then substitute into Eq. 1.42.

Aggregate, $\left(\frac{\partial W}{\partial H}\right)_{agg}$ To determine the moisture capacity of aggregate used in eq. 1.31, n , k , V_m , and W of aggregate in Eq.1.40, 1.41, 1.36 and 1.32, respectively are first determined and then substitute into Eq. 1.42.

1.1.2.2 Moisture Diffusivity

The moisture diffusivity of concrete used in the analysis of moisture diffusion in concrete can be selected from the following proposed models.

Ababneh (2002) The humidity diffusion coefficient of concrete depends on both the humidity diffusion coefficients of cement paste and aggregate. It can be evaluated based on composite theory (Christensen 1979) as follows (Ababneh et al. 2002):

$$D_h = D_{Hcp} \left(1 + \frac{g_i}{\frac{1-g_i}{3} + \frac{1}{\frac{D_{Hagg}}{D_{Hcp}} - 1}} \right) \quad (1.43)$$

where

- D_h = humidity diffusion coefficient of concrete
- D_{Hcp} = humidity diffusion coefficient of cement paste
- D_{Hagg} = humidity diffusion coefficient of aggregate
- g_i = the volume fraction of aggregate

Humidity Diffusion Coefficient of Cement Paste D_{Hcp} The humidity diffusion coefficient of cement paste is strongly influenced by the pore structure of the concrete. There are three distinct transport mechanisms which may occur:

Molecular diffusion (ordinary diffusion). Molecular diffusion process can be shown in Fig. 1.6: From Fig. 1.6, we can explain the behavior of this mechanism as follows.

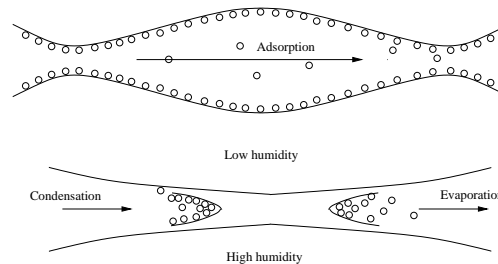


Fig. 1.6. Molecular Diffusion in terms of Humidity

1. At low relative humidity, field force of pore wall captures water molecules to form the first layer. Other molecules continue to move, and as the humidity increases, more layers of water molecules cover the pore walls. Thus space available for vapor inside the macropore decreases. Force field in the wall weakens and then the mean free path is reduced.
2. At high humidity, the adsorbed water will form a meniscus at a neck, and the neck is then completely filled. Then water molecules condense at one end of the neck, while at the other end they evaporate. This condensation/evaporation strongly accelerate the diffusion process.

This diffusion process will dominate when the mean free path of the water vapor (800A at 25°C) is small compared to diameter of macropore (usually 50 nm to 10 μm). Pores of this

size are few in concrete, hence the molecular diffusion or ordinary diffusion occurs only occasionally in concrete. It is not the dominant mechanism.

Knudsen diffusion Mesopores (25 to 500Å) and Micropores (< 25Å) comprise the largest portion of concrete pores. In this case collision between molecules and against pore walls is the main diffusion mechanism. There is some similarity with molecular diffusion, but in Knudsen diffusion, the diffusion resistance is related to pore size.

Surface diffusion In parallel pore walls, the water molecule never escape the force field of the pore surface. The transport involves a thermally activated process with jumps between the adsorption sites. In general, it is insignificant unless most of the water is adsorbed water. Hence, it is significant in concrete only at very low humidity.

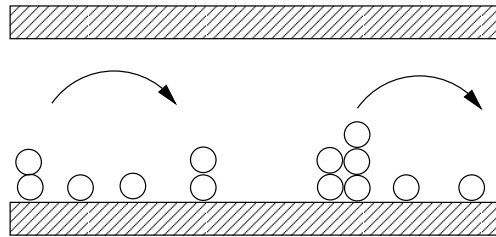


Fig. 1.7. Surface Diffusion

The developed model will not treat each mechanism separately, but it will predict the general combined trend. At low humidity, pore volume, surface force field, and mean free path, all decrease. These effects may offset each others and the effective diffusivity for all mechanisms becomes constant. At high humidity capillary condensation occurs, and thus diffusion resistance decreases. An empirical model, which captures those trends is proposed:

$$D_{Hcp} = \alpha_h + \beta_h [1 - 2^{-10\gamma_h(H-1)}] \quad (1.44)$$

$$\alpha_h = 1.05 - 3.8 \frac{w}{c} + 3.56 \left(\frac{w}{c} \right)^2 \quad (1.45)$$

$$\beta_h = -14.4 + 50.4 \frac{w}{c} - 41.8 \left(\frac{w}{c} \right)^2 \quad (1.46)$$

$$\gamma_h = 31.3 - 136 \frac{w}{c} + 162 \left(\frac{w}{c} \right)^2 \quad (1.47)$$

where α_h , β_h and γ_h are coefficients calibrated from test data. All of them are strongly affected by the water to cement ratio w/c . Curing time is negligible.

Humidity Diffusion Coefficient of Aggregates D_{Hagg} Since the pores in the aggregates are discontinuous, the value of the humidity diffusion coefficient of aggregate in eq.1.43 is negligible compared with the one of cement paste. Therefore, in the computation it can be neglected (Ababneh et al. 2002).

Mensi The moisture diffusivity of concrete proposed by Mensi et al. (1988) is given by

$$D(C) = Ae^{BC} \quad (1.48)$$

where A and B are constants. C is the free water content in l/m^3 which is a function of relative humidity in concrete (H) as given by

$$C = C_0.H \quad (1.49)$$

where C_0 is constant.

Bazant The moisture diffusivity of concrete proposed by Bazant and Thonguthai (1978) is given by

$$D_h(H) = D_1 \left(\alpha_D + \frac{1 - \alpha_D}{1 + \left(\frac{1-H}{1-0.75} \right)^n} \right) \quad (1.50)$$

where $D_1 = 3.10 \times 10^{-10} \text{ m}^2/\text{s}$; $\alpha_D \in [0.025 : 0.1]$ and $n = 6$.

1.1.2.3 Final Algorithm for Moisture Diffusion into Concrete

The algorithm for the moisture diffusion into the concrete is summarized in Fig. 1.8.

1.1.3 COUPLED HEAT TRANSFER AND MOISTURE DIFFUSION ANALYSIS

The question of moisture transport - heat transfer coupling was addressed by the pioneer work of Luikov (1975). Several available published models were derived from his work. In particular, Bažant et al. (1981) showed that the governing differential equation for heat transfer in concrete could be written as follows:

$$\rho C \frac{\partial T}{\partial t} = -\text{div} \mathbf{q} + C_w \mathbf{J} \cdot \nabla T + C_a \frac{\partial W}{\partial H} \frac{\partial H}{\partial t} \quad (1.51)$$

where

ρ	Density in kg/m^3
T	Temperature in $^\circ\text{C}$
W	water (moisture) content (for unit volume of material)
H	pore relative humidity
C	Specific heat of concrete in $\text{J}/\text{kg}^\circ\text{C}$
C_a	heat absorption of free water
C_w	mass density and isobaric (constant pressure) heat capacity of liquid water
$\frac{\partial W}{\partial H}$	Moisture capacity
\mathbf{J}	Moisture flux, $-D_h \nabla H$
\mathbf{q}	Heat flux, $k \nabla T$

The mass density and isobaric (constant pressure) heat capacity of liquid water C_w ($10^6 \text{ J}/\text{kg}$) is given by

$$C_w = 350,000 \left(\frac{374.15 - T_K}{T_C} \right)^{\frac{1}{3}} \quad (1.52)$$

where T_K is temperature in K and T_C is temperature in $^\circ\text{C}$. It has been mentioned in Bažant et al. (1981) that the heat absorption of free water C_a can be neglected because it contributes much less than C . However, in this model we assume it to be as follows;

$$C_a = C_{af} C \quad (1.53)$$

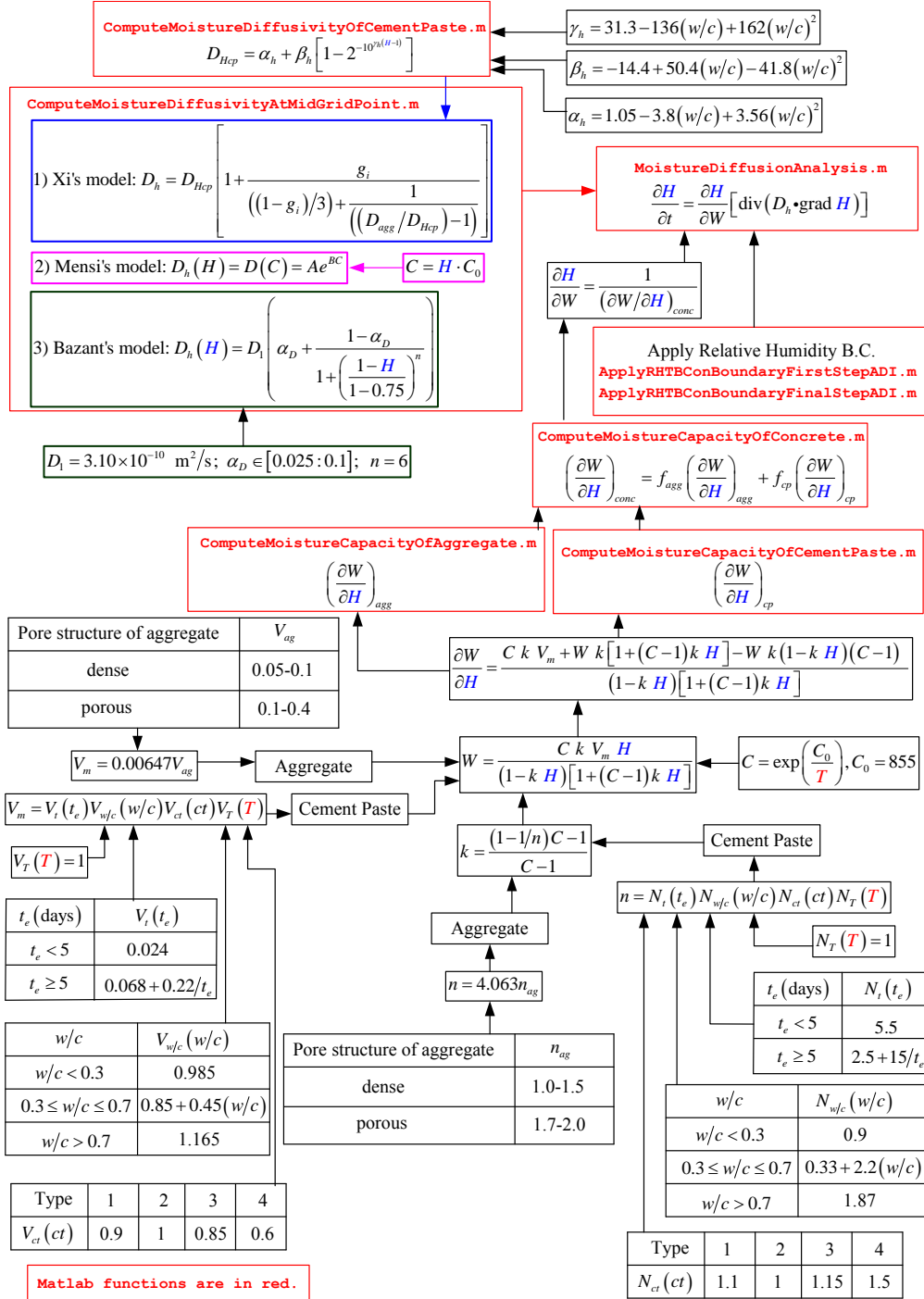


Fig. 1.8. Algorithm for moisture diffusion analysis

where C_{af} is a constant = 0.001 We note that the second term in Eq. 1.51 accounts for heat convection due to the movement of water which is significant only for very rapid heating.

The moisture balance equation given by Xi, Bažant and Jennings (1994) and Ababneh et al. (2002) is modified by accounting for the moisture transfer due to heat gradient (Tariku et al. 2010) and the addition of the relative humidity due to evaporable water released into the pore by dehydration of the cement paste Bažant et al. (1981):

$$\frac{\partial H}{\partial t} = \frac{\partial H}{\partial W} [\text{div} \mathbf{J} + \text{div} (D_{ht} \nabla T)] + \frac{\partial H}{\partial W} \frac{\partial W_d}{\partial t} \quad (1.54)$$

where

- W water (moisture) content (for unit volume of material)
- H (Moisture) Pore relative humidity = $\frac{P_v}{P_{vs}}$
- P_v Vapour pressure
- P_{vs} Saturation vapour pressure = $P_{atm} \cdot e^{\left(\frac{4871.3(T-100)}{373.15T}\right)}$ Benoit et al. (2012) (T is Temperature in K)
- P_{atm} Standard atmospheric pressure = 101,325 Pa
- W_d Total mass of free evaporable water released into the pore by dehydration of the cement paste
- T Temperature in $^{\circ}C$
- D_h Permeability or humidity diffusivity
- D_{ht} Humidity diffusivity under the influence of a temperature gradient
- $\alpha_{D,ht}$ thermal gradient coefficient
- \mathbf{J} Moisture flux, $-D_h \nabla H$

$$D_h = \begin{cases} D_{h,0} f_1(T) & \text{for } T \leq 95^{\circ}C \\ D_{h,0} f_1(95^{\circ}C) f_2(T) & \text{for } T > 95^{\circ}C \end{cases} \quad (1.55)$$

$D_{h,0}$ has been given in Sect. 1.1.2.2.

It has been mentioned in Bažant et al. (1981) that the thermal gradient contribution term $\text{div} (D_{ht} \nabla T)$ to eq. 1.54 is very small. Approximately, $D_{ht} \approx 0$. However in this model, it is assumed to be

$$D_{ht} = \alpha_{D,ht} D_h \quad (1.56)$$

where $\alpha_{D,ht}$ is a constant.

$$f_1(T) = e^{\frac{Q}{R} \left(\frac{1}{T_{ref}} - \frac{1}{T} \right)} \quad \text{for } T \leq 95^{\circ}C \quad (1.57)$$

in which T is absolute temperature (K), Q is activation energy for water migration along the adsorption layers in the necks, and R is gas constant.

$$f_2(T) = e^{\frac{T-95}{0.881+0.214(T-95)}} \quad \text{for } T > 95^{\circ}C \quad (1.58)$$

and the amount of dehydrate water W_d per m^3 of concrete is given by

$$W_d = W_H^{105} f_d(T) \quad (1.59)$$

in which W_H^{105} is hydrate water content at $105^{\circ}C$. Dehydration of the hydrate water begins at about $120^{\circ}C$.

$f_d(T)$ is a function of the weight loss of the concrete due to heat. The function of W_H is given by

$$W_H(t_e) = 0.21c \left(\frac{t_e}{\tau_e + t_e} \right), \tau_e = 23 \text{ days} \quad (1.60)$$

where c is mass of (anhydrous) cement per m^3 of concrete and t_e is the equivalent hydration period which is given by

$$t_e = \int \beta_H \beta_T dt \quad (1.61)$$

$$\beta_H(H) = \frac{1}{1 + (3.5 - 3.5H)^4} \quad (1.62)$$

$$\beta_T(T) = e^{\frac{Q_h}{R} \left(\frac{1}{T_{ref}} - \frac{1}{T} \right)} \quad (1.63)$$

where

t actual time
 Q_h activation energy of hydration
 $\frac{Q_h}{R} = 2700^\circ K$

We can summarize the moisture diffusivity of concrete used in Eq.1.54 by using moisture diffusivity of concrete $D_{h,0}$ given in Sect. 1.1.2.2 with the effect of temperature given in Eq.1.55 as in Fig. 1.9 The interaction between the two diffusion models is illustrated by Fig. 1.10.

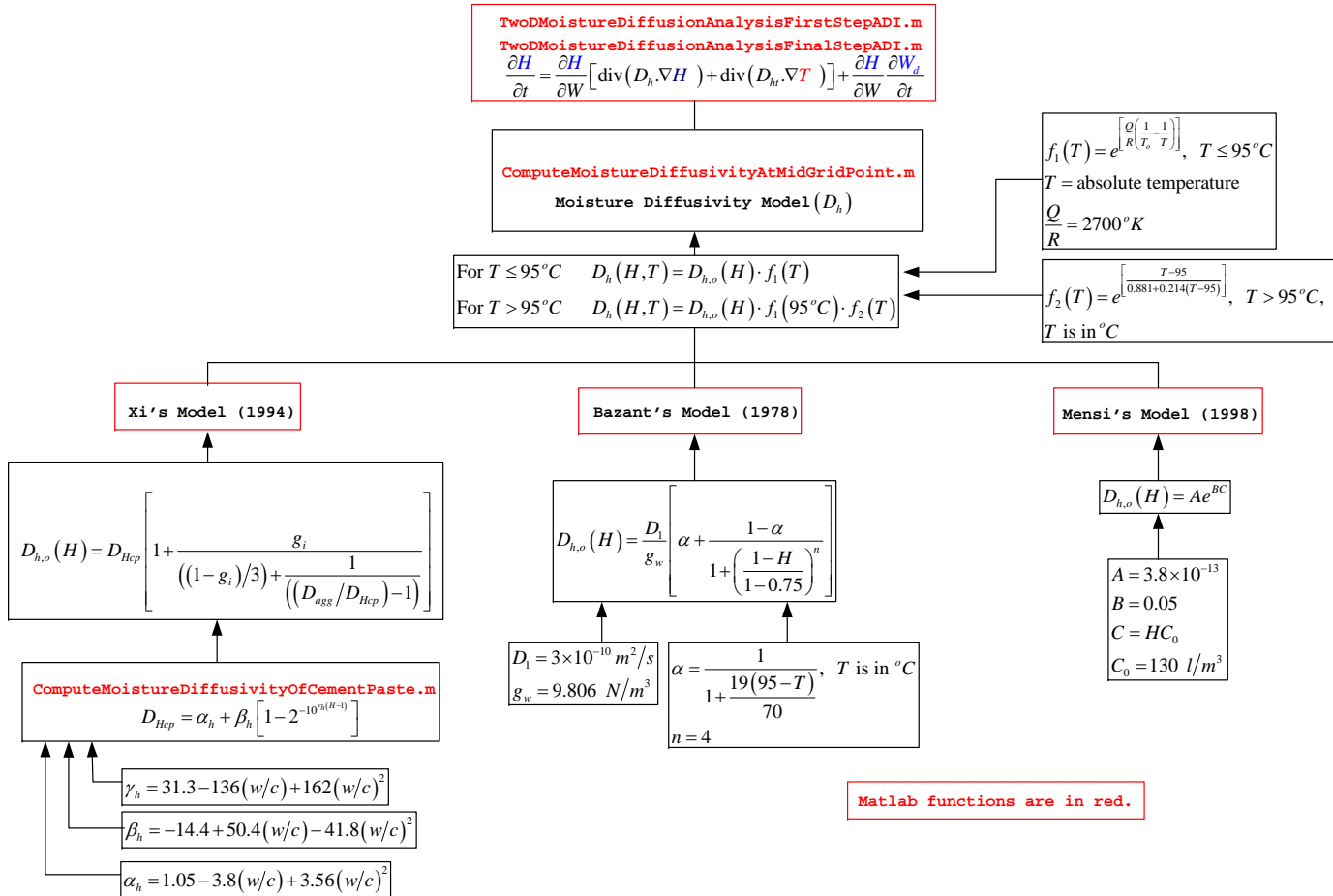


Fig. 1.9. Moisture Diffusivity of Concrete

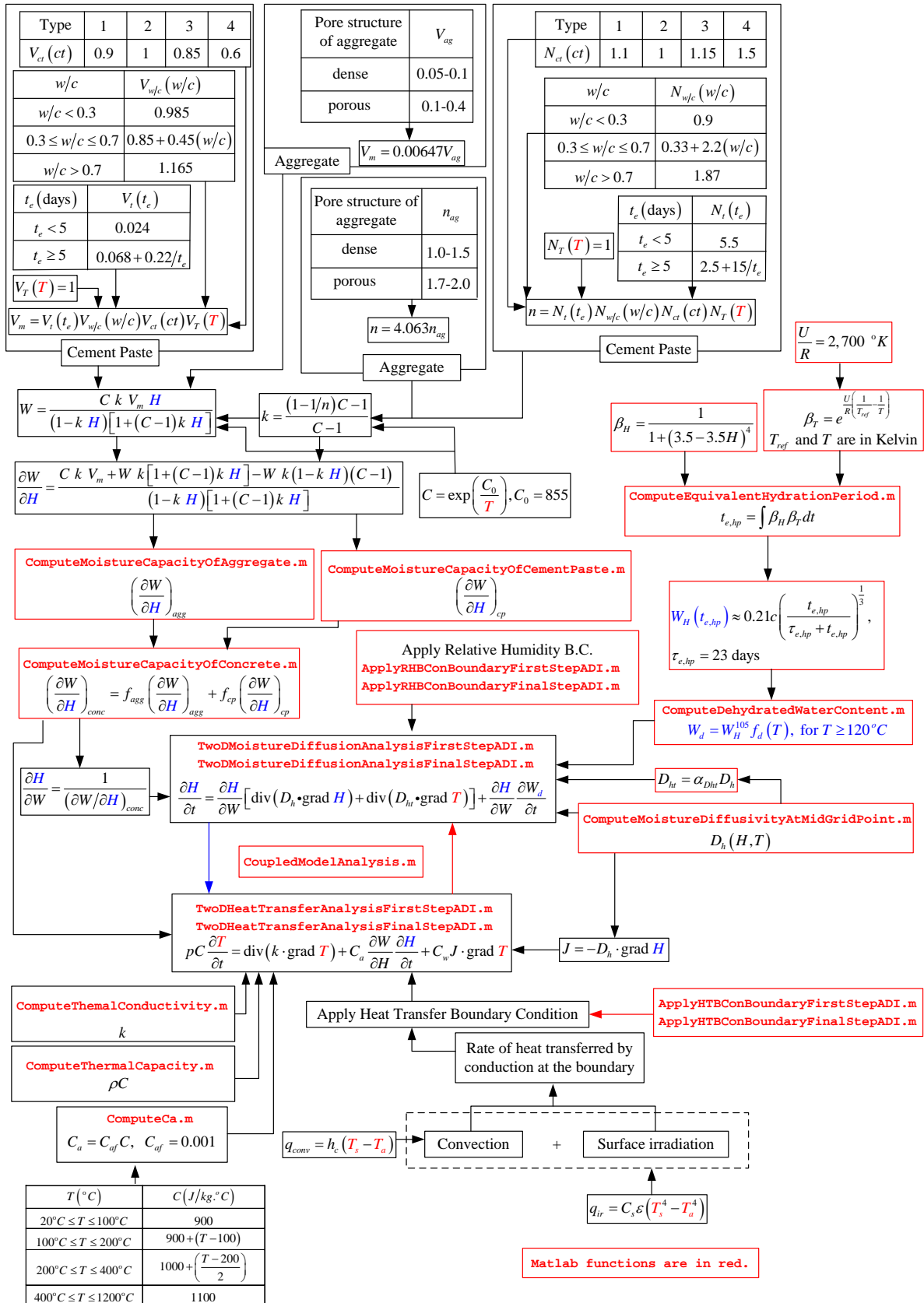


Fig. 1.10. Coupling between moisture and thermal diffusion models

1.2 FINITE DIFFERENCE IMPLEMENTATION

As shown in the previous chapter, we can summarize all of the governing equations in Table 1.4 and their diffusion coefficients and boundary conditions in Table 1.5.

Table 1.4. Governing Differential Equations

Process	Differential Equations	Primary Variable
Heat Transfer	$\frac{\partial T}{\partial t} = \frac{1}{\rho C} \text{div}(k \cdot \nabla T) + Q$	T
Moisture Diffusion	$\frac{\partial H}{\partial t} = \frac{\partial H}{\partial W} \text{div}(D_h \cdot \nabla H)$	H

NOTE: T = Temperature inside the concrete (Kelvin), H = Pore Relative Humidity inside the concrete (%), t = Time, n = Normal direction to the surface, h_c = Convection coefficient, C_s = Stefan Boltzman constant, W = water content in the concrete.

Table 1.5. Diffusion Coefficients and Boundary Conditions in Each Diffusion Process

Process	Diffusion Coeff.	Binding Capacity	Boundary Conditions
Heat Transfer	$\frac{k}{\rho C}$	-	1) $T = T_a$ 2) $\frac{\partial T}{\partial n} = 0$ 3) $-k \frac{\partial T}{\partial n} = h_c(T - T_a) + C_s \epsilon (T^4 - T_a^4)$
Moisture Diffusion	$D_h(H, w/c)$	$\frac{\partial H}{\partial W}(T, H, w/c, ct, t_o)$	1) $H = H_{env}$ 2) $\frac{\partial H}{\partial n} = 0$

We note that all the governing equations are parabolic partial differential equations. To obtain solution of these problems, a finite difference method is used.

The finite difference method (Rosenburg 1969) is used when the problem cannot be solved analytically or the analytical solution becomes so involved that numerical computation is very difficult. In this approach, the problem domain is discretized so that the values of the unknown dependent variable are considered only at a finite number of nodal points in the region. If the region is discretized into m nodes, m

algebraic equations are developed by discretizing the governing equation and the boundary conditions for the problem. As a result, the problem of solving the partial differential equation over the problem domain is transformed to the problem of setting a group of algebraic equations and solving for the solutions using a suitable method.

To discretize the derivative of the partial differential equation, there are two approaches:

1. Taylor series expansion
2. Control volume approach

The details of the finite difference discretization (Rosenburg 1969) of each equation in 2D problems, follows.

1.2.1 DISCRETIZATION

1.2.1.1 Linear Parabolic Differential Equation

The governing partial differential equation for heat transfer is given by

$$\frac{\partial T}{\partial t} = \frac{1}{\rho C} \text{div}(k \cdot \nabla T) + Q \quad (1.64)$$

and we examine its discretization in 2D as follows.

For 2D problem, the differential equation is rewritten as

$$\frac{\partial T}{\partial t} = \frac{1}{\rho(x, y) \cdot C(x, y)} \left[\frac{\partial}{\partial x} \left(k(x, y) \cdot \frac{\partial T}{\partial x} \right) + \frac{\partial}{\partial y} \left(k(x, y) \cdot \frac{\partial T}{\partial y} \right) \right] + Q \quad (1.65)$$

again, subject to appropriate boundary and initial conditions. We introduce the notation

$$T(x, y, t) = T(i\Delta x, j\Delta y, n\Delta t) \quad (1.66)$$

To solve the 2D problem, an alternating direction implicit (ADI) method is used, (Rosenburg 1969).

Given the known primary variables at time n , we seek to determine their values at time $n + 1$. This is accomplished in two steps. First, the computations from time level n to $n + \frac{1}{2}$ level will be performed followed by the computations from $n + \frac{1}{2}$ to $n + 1$. For the advancement from n to $n + \frac{1}{2}$, an implicit method is used in one direction, say x and an explicit method is used in the other direction, i.e., y . As a result, the finite difference equations for any horizontal row on which the value of j is constant form a tridiagonal matrix, Fig. 1.11 and their solution can be obtained by using Matlab.

Next, to advance from $n + \frac{1}{2}$ to $n + 1$ we reverse the direction of the implicit and explicit methods. As a result, the finite difference equations for any vertical column on which the value of i is constant form a tridiagonal matrix and their solution again can be obtained by Matlab. The computation process is repeated by alternately changing the directions of the implicit and explicit methods. The ADI method can be summarized in the Fig. 1.12

1.2.1.2 Nonlinear Parabolic Partial Differential Equation

From Table 1.4, the moisture diffusion problem is governed by nonlinear parabolic partial differential equations. Their governing equations can be expressed as:

$$\frac{\partial u}{\partial t} = C(u) \text{div}(D(u) \cdot \nabla u) \quad (1.67)$$

$$\begin{bmatrix}
b_1 & c_1 & 0 & 0 & 0 & 0 & 0 & 0 & 0 & 0 \\
a_2 & b_2 & c_2 & 0 & 0 & 0 & 0 & 0 & 0 & 0 \\
0 & a_3 & b_3 & c_3 & 0 & 0 & 0 & 0 & 0 & 0 \\
0 & 0 & \times & \times & \times & 0 & 0 & 0 & 0 & 0 \\
0 & 0 & 0 & \times & \times & \times & 0 & 0 & 0 & 0 \\
0 & 0 & 0 & 0 & \times & \times & \times & 0 & 0 & 0 \\
0 & 0 & 0 & 0 & 0 & \times & \times & \times & 0 & 0 \\
0 & 0 & 0 & 0 & 0 & 0 & \times & \times & \times & 0 \\
0 & 0 & 0 & 0 & 0 & 0 & 0 & a_{m-1} & b_{m-1} & c_{m-1} \\
0 & 0 & 0 & 0 & 0 & 0 & 0 & 0 & a_m & b_m
\end{bmatrix}
\begin{bmatrix}
T_1 \\
T_2 \\
T_3 \\
\times \\
\times \\
\times \\
\times \\
\times \\
\times \\
T_{m-1} \\
T_m
\end{bmatrix}
=
\begin{bmatrix}
d_1 \\
d_2 \\
d_3 \\
\times \\
\times \\
\times \\
\times \\
\times \\
\times \\
d_{m-1} \\
d_m
\end{bmatrix}$$

$a_1 = c_m = 0$

Fig. 1.11. Tridiagonal Matrix

where u is dependent variables, $D(u)$ is diffusion coefficient and $C(u)$ is an additional coefficient involved in the diffusion process.

The terms of u , $C(u)$, and $D(u)$ for the moisture diffusion process can be summarized in Table 1.6. Again, we shall examine 2D discretization of this equation.

Table 1.6. Variable and Coefficients of Diffusion Process

Process	Variable u	$C(u)$	$D(u)$
Moisture Diffusion	H	$\frac{\partial H}{\partial w}$	D_h

In 2D problem, the ADI method will again be used to discretize the governing equation:

$$\frac{\partial u}{\partial t} = C(u) \left[\frac{\partial}{\partial x} \left(D(u) \frac{\partial u}{\partial x} \right) + \frac{\partial}{\partial y} \left(D(u) \frac{\partial u}{\partial y} \right) \right] \tag{1.68}$$

The discretization procedure is illustrated by Fig.1.13

The solution of nonlinear parabolic partial differential equation hinges on the determination of old value (Rosenburg 1969). The concept of this method is as follows. Suppose that the computations are to

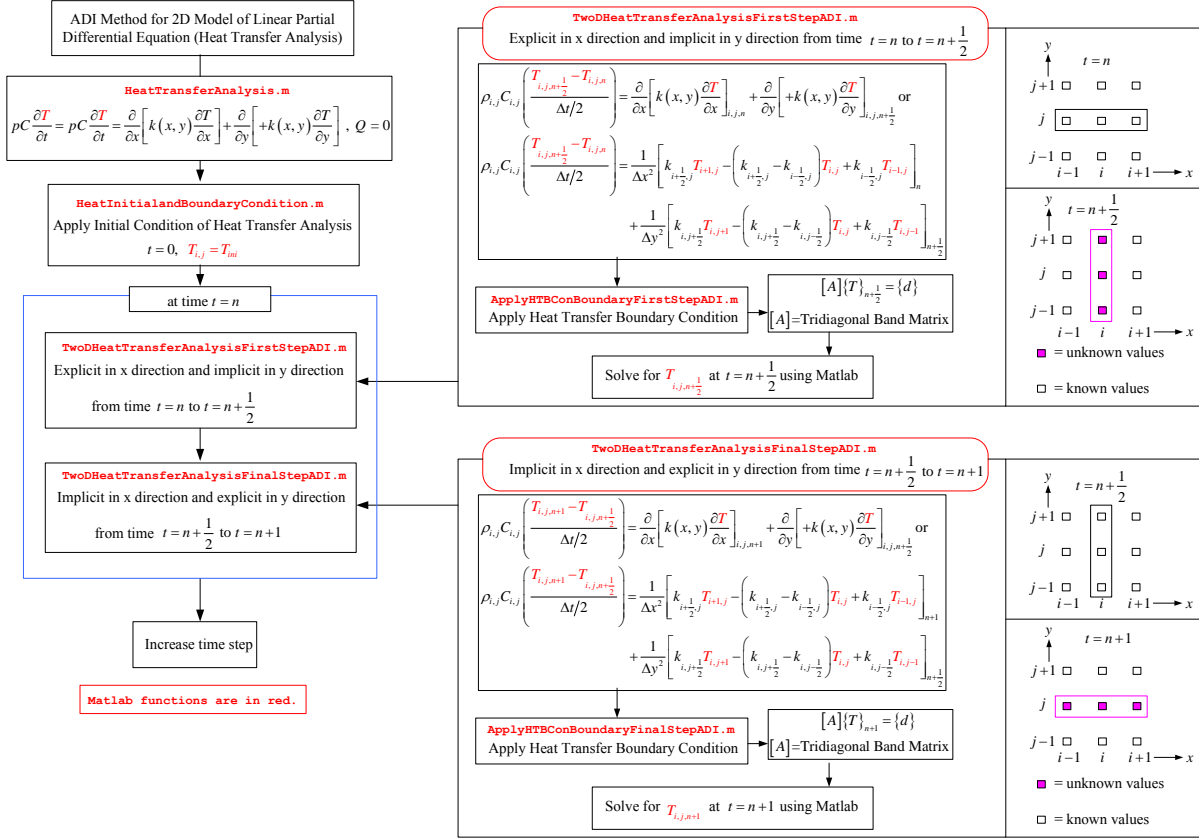


Fig. 1.12. ADI Method

advance from the n time level to the $n + 1$ time level. For 2D problem, and using the ADI method, the nonlinear coefficients, $C(u)$, $D(u)$, and $E(u)$ have to be evaluated at time $t = n + \frac{1}{2}$.

The simplest method is to obtain the nonlinear coefficients by evaluating them at old time value ($t = n$) and then use them for $t = n + \frac{1}{2}$. For example, we use $C(u_n)$ for $C(u_{n+\frac{1}{2}})$ and $D(u_n)$ for $D(u_{n+\frac{1}{2}})$. If the nonlinear coefficients do not change rapidly with u , then the result of the finite difference equations (u_{n+1}) should be close to the correct values.

The solution can be improved by evaluating the nonlinear coefficients at half time ($t = n + \frac{1}{2}$) from

$$C(u_{n+\frac{1}{2}}) = C\left(\frac{u_n + u_{n+1}^{m=1}}{2}\right) \quad (1.69)$$

$$D(u_{n+\frac{1}{2}}) = D\left(\frac{u_n + u_{n+1}^{m=1}}{2}\right) \quad (1.70)$$

$$(1.71)$$

where m is an iteration index and if $m = 1$, then $u_{i,j,n+1}^1$ is obtained from $C(u_{n+\frac{1}{2}})$ and $D(u_{n+\frac{1}{2}})$. The computations are carried on until the solution converges ($u_{i,j,n+1}^{m+1} = u_{i,j,n+1}^m$), and then the iteration process stops and the computation moves to the next time step ($t = n + 2$).

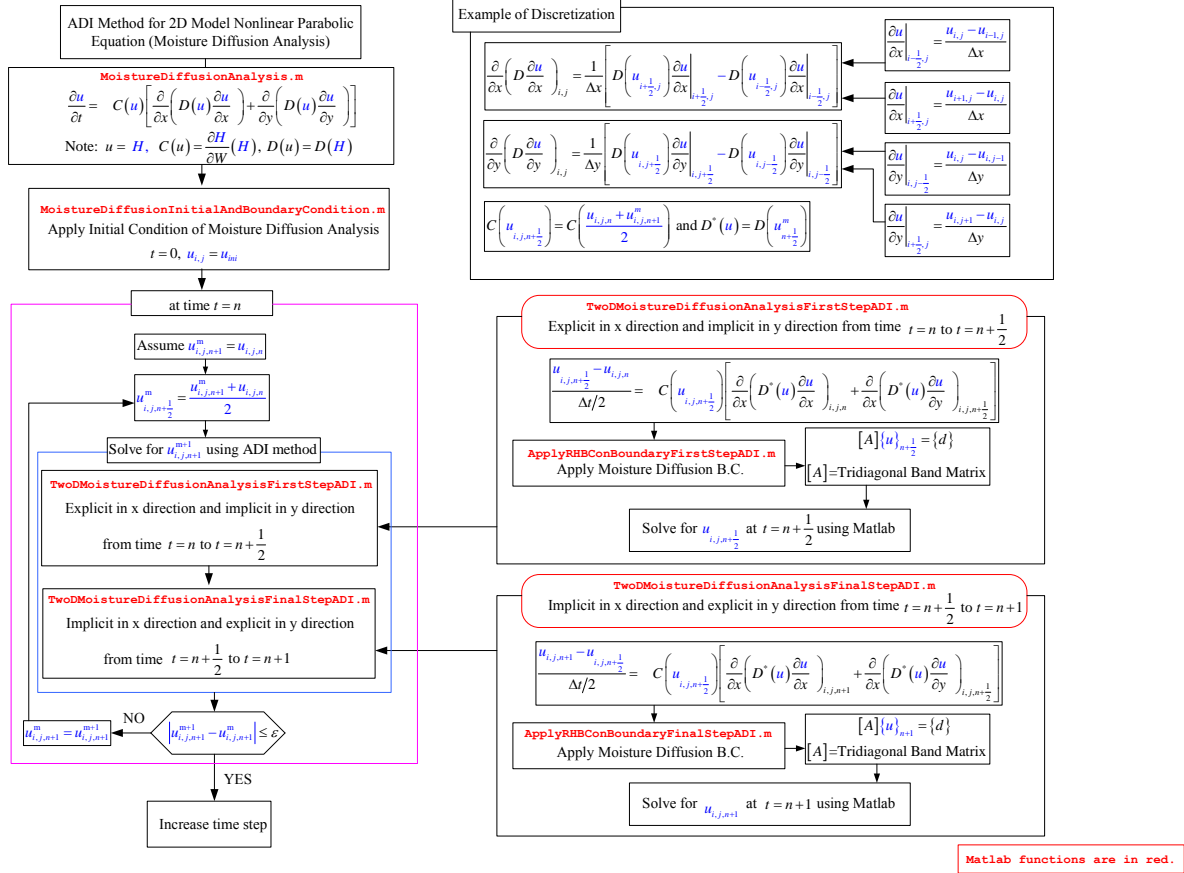


Fig. 1.13. Discretization of 2D Nonlinear Parabolic Partial Differential Equation using ADI Method and Iteration Using Old Value Method

The procedure of this iteration method for 2D nonlinear parabolic partial differential equation is summarized by Fig. 1.13.

1.2.2 BOUNDARY CONDITIONS

From Table 1.4, there are 3 types of boundary conditions which applied to the diffusion problems. They are:

No flux boundary condition: In this case, the format of the boundary condition equation is

$$\frac{du}{dx} = 0 \quad (1.72)$$

where u is T and H in the heat transfer and moisture diffusion, respectively.

Concentration boundary condition: In this case, the format of the boundary condition equation is

$$u = u_{env} \quad (1.73)$$

where u is T and H in the heat transfer and moisture diffusion, respectively and u_{env} represents the environmental concentration of the variable u .

Nonlinear boundary condition: This type of boundary condition will occur only in the heat transfer analysis. The format of this boundary condition is

$$-k \frac{dT}{dx} = h_c(T - T_a) + C_s \epsilon (T^4 - T_a^4). \quad (1.74)$$

In the next sections, we discuss in details the application of each one of those boundary conditions to 2D problems.

1.2.2.1 No flux Boundary Condition

At any row j , if we apply Eq.1.72 at one end (node $i = 1$), then to determine the value of the first derivative in Eq.1.72 at $i = 1$, we first introduce a fictitious point, x_0 outside the region then the second-order-correct dialog (Rosenburg 1969) for $\frac{du}{dx}|_1$ is given by

$$\frac{u_{2,j} - u_{0,j}}{2\Delta x} = 0 \quad (1.75)$$

or

$$u_{0,j} = -u_{2,j} \quad (1.76)$$

We then substitute the value of $u_{0,j} = -u_{2,j}$ into the right hand side of the equation in Fig. 1.12 when $i = 1$. The final results in Fig. 1.12 still be a tridiagonal matrix and can be solved by using Matlab.

1.2.2.2 Concentration Boundary Condition

At any row j , if we apply this boundary condition to Eq.1.73 at one end (for example, at node $i = 1$), then the boundary condition equation will be given by

$$u_{1,j} = u_{env} \quad (1.77)$$

We then substitute the value of $u_{1,j} = u_{env}$ into the right hand side of the equation in Fig. 1.12 when $i = 2$. The final results in Fig. 1.12 will still be a tridiagonal matrix and can be solved by using Matlab.

1.2.2.3 Nonlinear Boundary Condition

Again, considering Eq.1.74, and assuming that the nonlinear boundary condition is applied at one end, say at $i = m$, then it will cause the last equation when $i = m$ to assume the following form:

$$a_m T_{m-1,n+1} + b_m T_{m,n+1} = d_m = h + g T_{i,n+1}^4 \quad (1.78)$$

where a_m , b_m , h , and g are known constants.

This equation becomes system of nonlinear algebraic equation. Then `fsolve`, the function in Matlab, is used to solve for the solution of this problem.

1.2.3 MATERIAL MODELS

To apply the finite difference method to the diffusion problems in a heterogeneous material as concrete, we have two options:

Homogeneous material: In this model, the material's properties at every finite difference grid point are the same and equal to properties of an equivalent homogeneous concrete.

Heterogeneous material: In this model, we discretize the heterogeneity of the concrete by assigning different properties to cement matrix and concrete aggregates.

Those two material models will be considered in the discretizations of both linear and nonlinear parabolic partial differential equations.

1.2.3.1 Linear parabolic partial differential equation

As previously mentioned, the diffusivity and other material's properties depend on the location of the grid point in the finite difference analysis. Because heterogeneous models are considered only in 2D problems, the 2D heterogeneous material model will be considered first. The 2D homogeneous models will be later shown to be a special case of the heterogeneous one, the former model.

Heterogeneous material model To account for the material model, first we consider the 2D finite difference discretization of Eq. 1.65 using control volume and ADI method as follows.

Going from time $t = n$ to $t = n + \frac{1}{2}$, we write:

$$\frac{\partial}{\partial x} \left[k(x, y) \frac{\partial T}{\partial x} \right]_{i, j, n + \frac{1}{2}} + \frac{\partial}{\partial y} \left[k(x, y) \frac{\partial T}{\partial y} \right]_{i, j, n} = \frac{1}{\alpha(x, y)} \frac{\partial T}{\partial t} \Big|_{i, j, n + \frac{1}{2}} \quad (1.79)$$

Assuming that $Q = 0$ and $\alpha(x, y) = \rho(x, y) \cdot C(x, y)$, then we rewrite the previous equation as

$$\begin{aligned} & \frac{\partial}{\partial x} \left[k_{i+\frac{1}{2}, j} \frac{\partial T}{\partial x} \Big|_{i+\frac{1}{2}, j} - k_{i-\frac{1}{2}, j} \frac{\partial T}{\partial x} \Big|_{i-\frac{1}{2}, j} \right]_{n+\frac{1}{2}} + \\ & \frac{\partial}{\partial y} \left[k_{i, j+\frac{1}{2}} \frac{\partial T}{\partial y} \Big|_{i, j+\frac{1}{2}} - k_{i, j-\frac{1}{2}} \frac{\partial T}{\partial y} \Big|_{i, j-\frac{1}{2}} \right]_n = \frac{1}{\alpha_{i, j, n + \frac{1}{2}}} \frac{\partial T}{\partial t} \Big|_{i, j, n + \frac{1}{2}} \end{aligned} \quad (1.80)$$

The materials properties in the above finite difference equations are $k_{i+\frac{1}{2}, j}$, $k_{i-\frac{1}{2}, j}$, $k_{i, j+\frac{1}{2}}$, $k_{i, j-\frac{1}{2}}$ and $\alpha_{i, j}$. We note from the space index that there is no difficulty to evaluate the value of $\alpha_{i, j}$. Its value is computed based on the material's property at node (i, j) . Next, the computation of the variables $k_{i+\frac{1}{2}, j}$, $k_{i-\frac{1}{2}, j}$, $k_{i, j+\frac{1}{2}}$ and $k_{i, j-\frac{1}{2}}$ will be illustrated.

First, the computation of $k_{i+\frac{1}{2}, j}$ is performed, then the rest of the diffusivity k can be computed using the same concept.

Suppose the value of k at node i, j is $k_{i, j}$, D_u at node $i + 1, j$ is $k_{i+1, j}$ and their values are not the same (because of the heterogeneity of the material). From the control volume approach, the material's properties from node i, j to node $i + 1, j$ can be shown as follows. From node i, j to node $i + \frac{1}{2}, j$,

$$k = k_{i, j}, \quad 0 \leq x \leq \frac{\Delta x}{2}. \quad (1.81)$$

And from node $i + \frac{1}{2}, j$ to node $i + 1, j$

$$k = k_{i+1,j}, \frac{\Delta x}{2} \leq x \leq \Delta x. \quad (1.82)$$

If the concentration at node i, j is $T_{i,j}$ and the concentration at node $i + 1, j$ is $T_{i+1,j}$, then the system can be summarized by Fig.1.14.

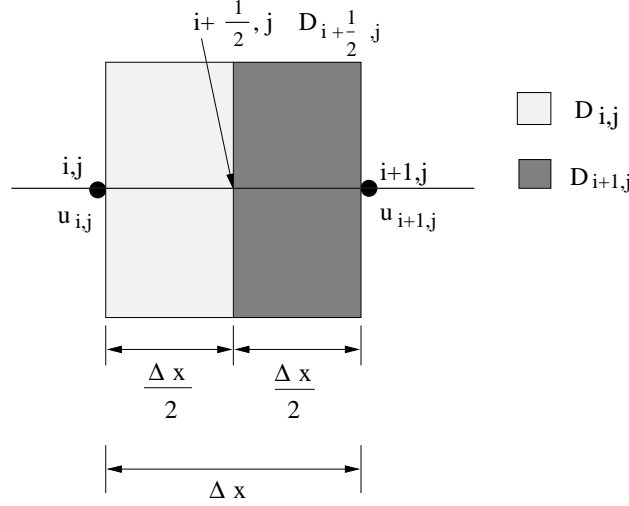


Fig. 1.14. The heterogeneous model for computing the diffusivity between two nodes which have different material's properties.

The flux of this system can be evaluated from:

$$q = -k(x) \frac{\partial T}{\partial x}$$

or

$$\frac{\partial T}{\partial x} = -\frac{q}{k(x)} \quad (1.83)$$

Suppose that we have the other system which has the same grid size and same concentration at the end nodes as the system shown in Fig.1.14 but now the system has only one effective diffusivity presented at the middle of the node $(i + \frac{1}{2}, j)$ and this system produces the same flux as the system mentioned above. The flux of the new system can be determined from the following equation:

$$q = -k_{i+\frac{1}{2},j} \frac{T_{i+1,j} - T_{i,j}}{\Delta x} \quad (1.84)$$

To determine the value of the effective diffusivity $k_{i+\frac{1}{2},j}$, substitute the value of q in Eq.1.84 into Eq.1.83, resulting in

$$\frac{\partial T}{\partial x} = k_{i+\frac{1}{2},j} \frac{T_{i+1,j} - T_{i,j}}{\Delta x} \frac{1}{k(x)} \quad (1.85)$$

$$\partial T = k_{i+\frac{1}{2},j} \frac{T_{i+1,j} - T_{i,j}}{\Delta x} \frac{\partial x}{k(x)} \quad (1.86)$$

$$\int_{T_{i,j}}^{T_{i+1,j}} \partial T = k_{i+\frac{1}{2},j} \frac{T_{i+1,j} - T_{i,j}}{\Delta x} \int_0^{\Delta x} \frac{\partial x}{k(x)} \quad (1.87)$$

$$T_{i+1,j} - T_{i,j} = k_{i+\frac{1}{2},j} \frac{T_{i+1,j} - T_{i,j}}{\Delta x} \int_0^{\Delta x} \frac{\partial x}{k(x)} \quad (1.88)$$

$$k_{i+\frac{1}{2},j} = \frac{\Delta x}{\int_0^{\frac{\Delta x}{2}} \frac{\Delta x}{k_{i,j}} + \int_{\frac{\Delta x}{2}}^{\Delta x} \frac{\Delta x}{k_{i+1,j}}} \quad (1.89)$$

$$k_{i+\frac{1}{2},j} = \frac{2}{\frac{1}{k_{i,j}} + \frac{1}{k_{i+1,j}}} \quad (1.90)$$

$$k_{i+\frac{1}{2},j} = \frac{2k_{i+1,j}k_{i,j}}{k_{i+1,j} + k_{i,j}} \quad (1.91)$$

Homogeneous material model From Eq.1.91, for the case where $k_{i,j} = k_{i+1,j} = k$ (homogeneous material model), we have

$$\begin{aligned} k_{i+\frac{1}{2},j} &= \frac{2}{\frac{1}{k} + \frac{1}{k}} \\ &= k \end{aligned} \quad (1.92)$$

1.2.3.2 Nonlinear parabolic partial differential equation

In this case, the diffusivity and the other material's properties depend on the unknown variables. The material model can be applied to this problem as follows.

Heterogeneous material model From Eq. 1.91, it can also be applied to the heterogeneous model of this type of equations. For instance, the value of $D_{u_{i+\frac{1}{2},j}}$ can be determined as the following equation:

$$D_{u_{i+\frac{1}{2},j}} = \frac{2 \cdot D_u(u_{i,j}) \cdot D_u(u_{i+1,j})}{D_u(u_{i,j}) + D_u(u_{i+1,j})} \quad (1.93)$$

Homogeneous material model Suppose that the material is homogeneous and that the diffusivity at each finite different node is a function of variable u . To evaluate the value of the diffusivity at the node which is in between two nodes those have different values of variable u , for instance, between node i, j and $i + 1, j$, the diffusivity at node $i + \frac{1}{2}, j$ has to be computed using the average value of u as

$$D_{u_{i+\frac{1}{2},j}} = D_u\left(\frac{u_{i,j} + u_{i+1,j}}{2}\right) \quad (1.94)$$

1.2.4 PROBLEM FORMULATION

Problem formulation for the deterioration of reinforced concrete structures will now be presented. In particular, we shall discuss the formulation for

1. Heat transfer
2. Heat and moisture diffusion

Each formulation will be separately presented.

1.2.4.1 Heat Transfer Analysis

For the heat transfer analysis alone, the numerical process is summarized by Fig. 1.15.

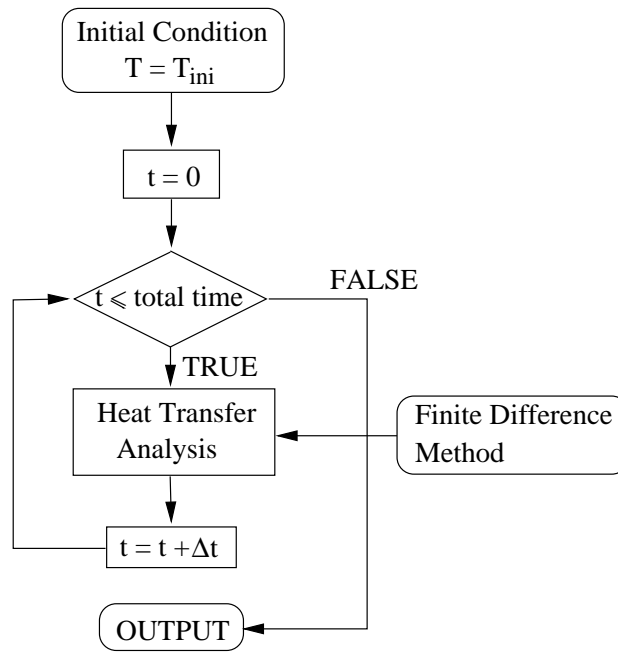


Fig. 1.15. Algorithms of Heat Transfer Analysis

Discretization The finite different discretization of heat transfer analysis is illustrated by Fig. 1.12 for 2D problem.

1.2.4.2 Heat Transfer and Moisture Diffusion Analysis

The moisture diffusion into the concrete structure depends strongly on the temperature inside the concrete. Since the outside temperature always changes, it's necessary to perform the heat transfer analysis in the simulation of moisture diffusion into the concrete structure. The numerical process of the moisture diffusion can be summarized by Fig. 1.16.

Discretization: The discretization of the governing differential equations of the heat transfer problem using finite difference method was already discussed in the previous section. For moisture diffusion equation, the finite difference discretization of the nonlinear parabolic partial differential equation, as discussed in Section 1.2.1.2, is as follows

2D Problem: By using ADI finite different method, as illustrated in Fig. 1.13, the discretization of 2D moisture diffusion is described by Fig. 1.17.

Material Model: In the moisture diffusion equation concrete's properties, i.e. moisture diffusivity D_h and moisture capacity $\frac{\partial H}{\partial W}$, are functions of relative humidity. The material models can be applied to compute each concrete's properties in moisture diffusion analysis as follows.

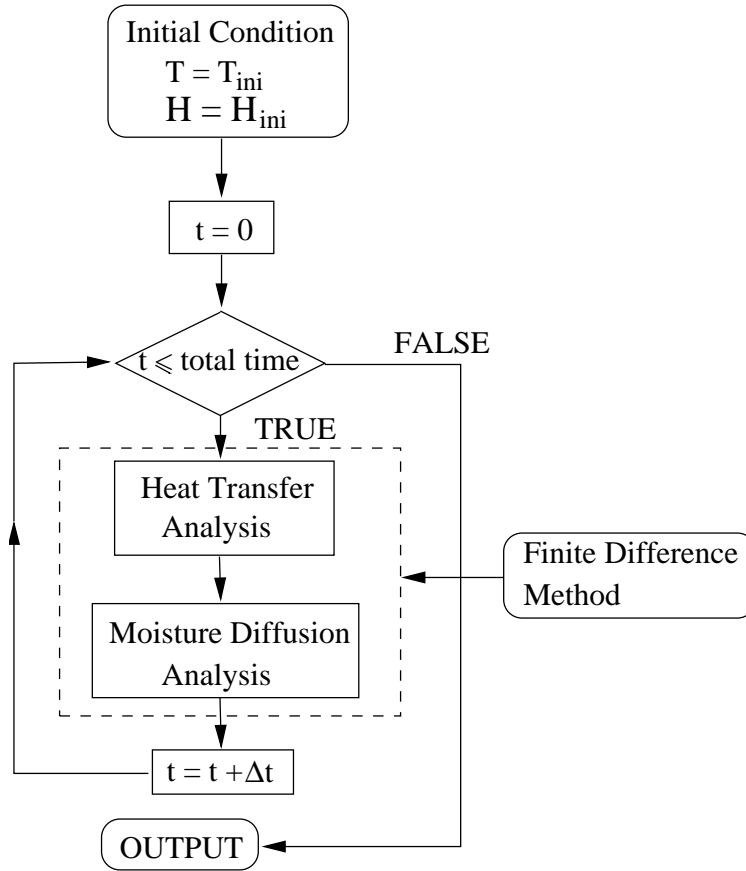


Fig. 1.16. Flowchart of Heat Transfer+Moisture Diffusion Analysis

$\frac{\partial H}{\partial W}(H)$: The determination of moisture capacity $\frac{\partial H}{\partial W}(H)$ in each material model is illustrated by Fig. 1.18.

Moisture Diffusivity $D_h(H)$: The determination of moisture capacity $D_h(H)$ in each material model is illustrated by Fig. 1.19.

Algorithm: Since the moisture diffusion equation is a nonlinear partial differential equation, to solve for the solution in the next time step the iteration using old value as shown in Fig. 1.13 is used.

1.2.4.3 Coupled Heat Transfer and Moisture Diffusion Analysis

The numerical finite-difference based solution of this problem is based on the model of Tamsir and Sivastava (2011) and is illustrated in Fig. 1.20

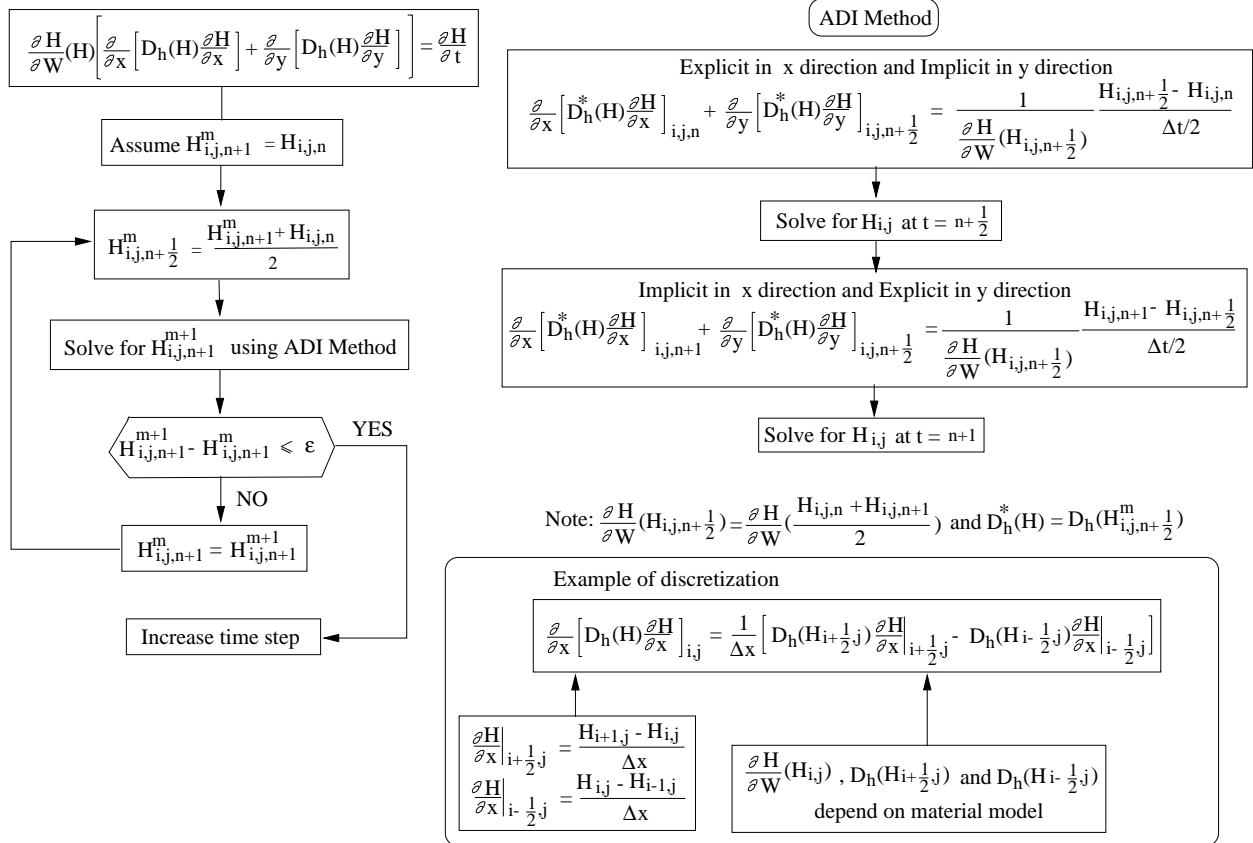


Fig. 1.17. Discretization of 2D Moisture Diffusion Equation using ADI Method

1. Homogeneous Material

$$\frac{dH}{dW} = \frac{1}{\frac{dW}{dH}}$$

$$\frac{dW}{dH} = \frac{C k V_m + W k [1 + (C-1)k H] - W k (1-k H)(C-1)}{(1-k H)[1 + (C-1)k H]}$$

2 Heterogeneous Material

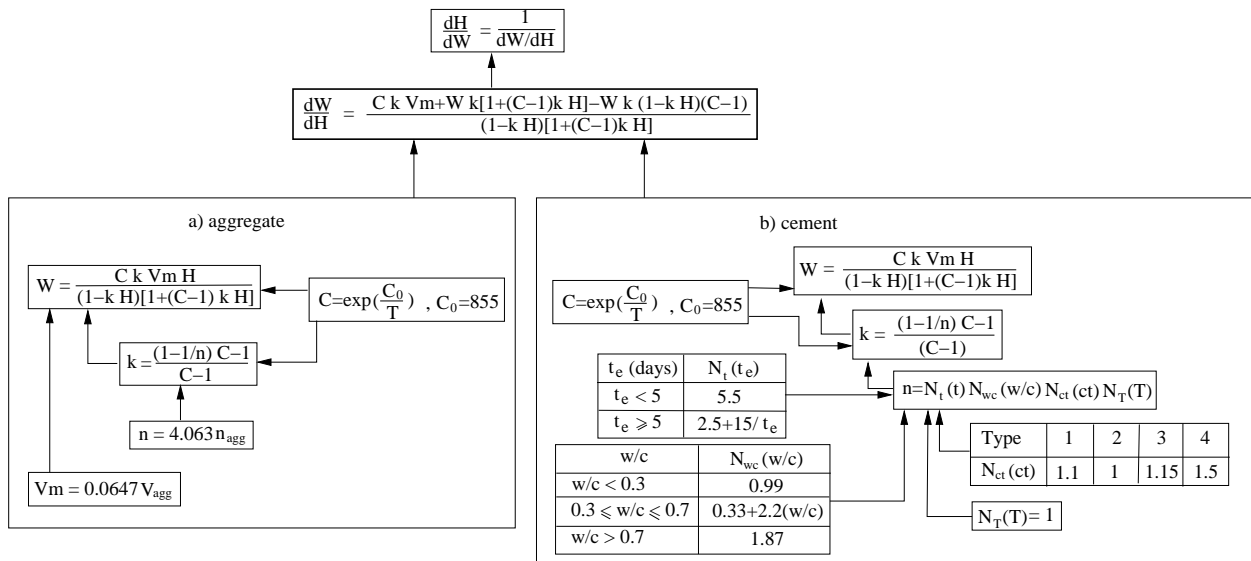


Fig. 1.18. Determination of $\frac{\partial H}{\partial W}(H)$

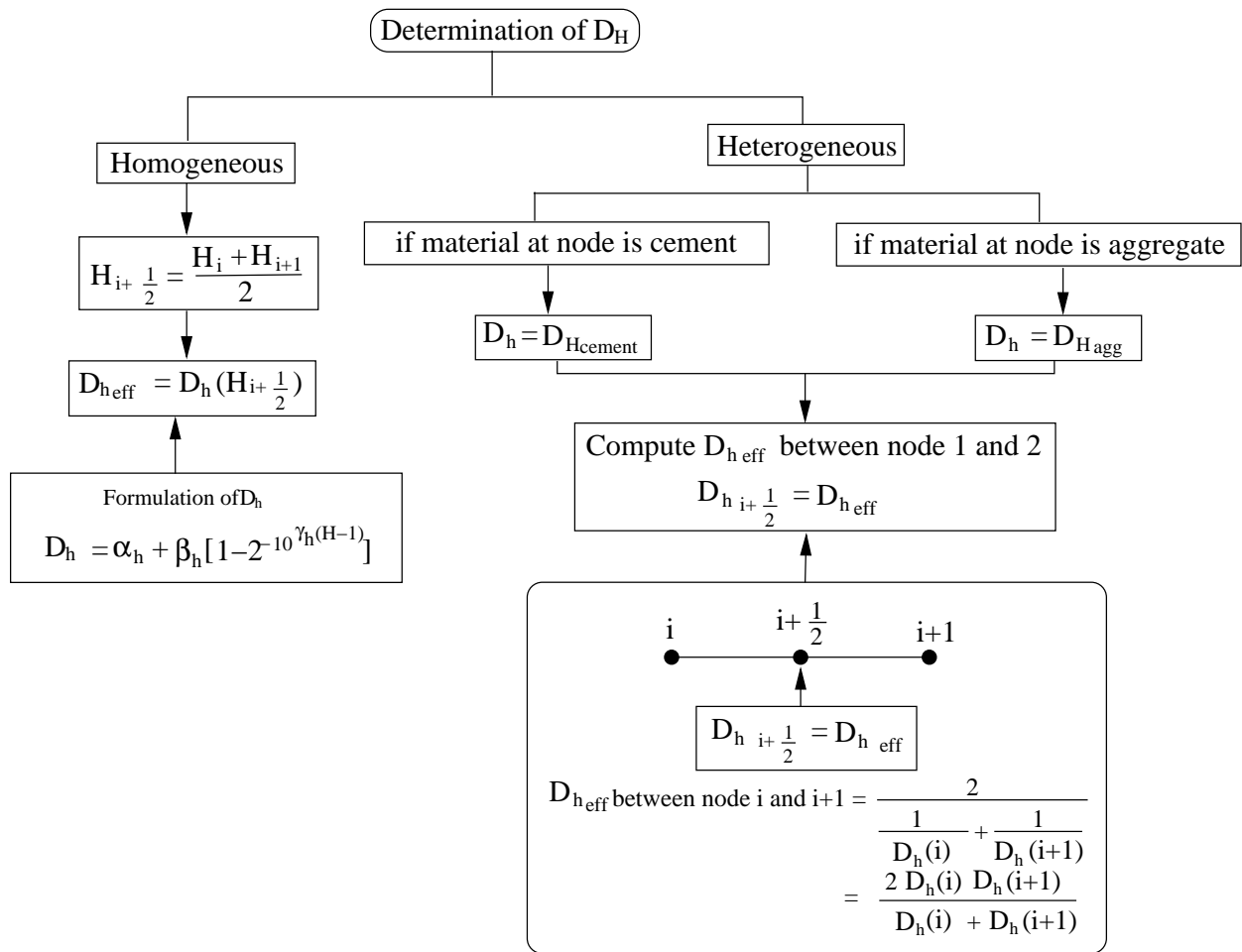


Fig. 1.19. Determination of Humidity Diffusivity D_h

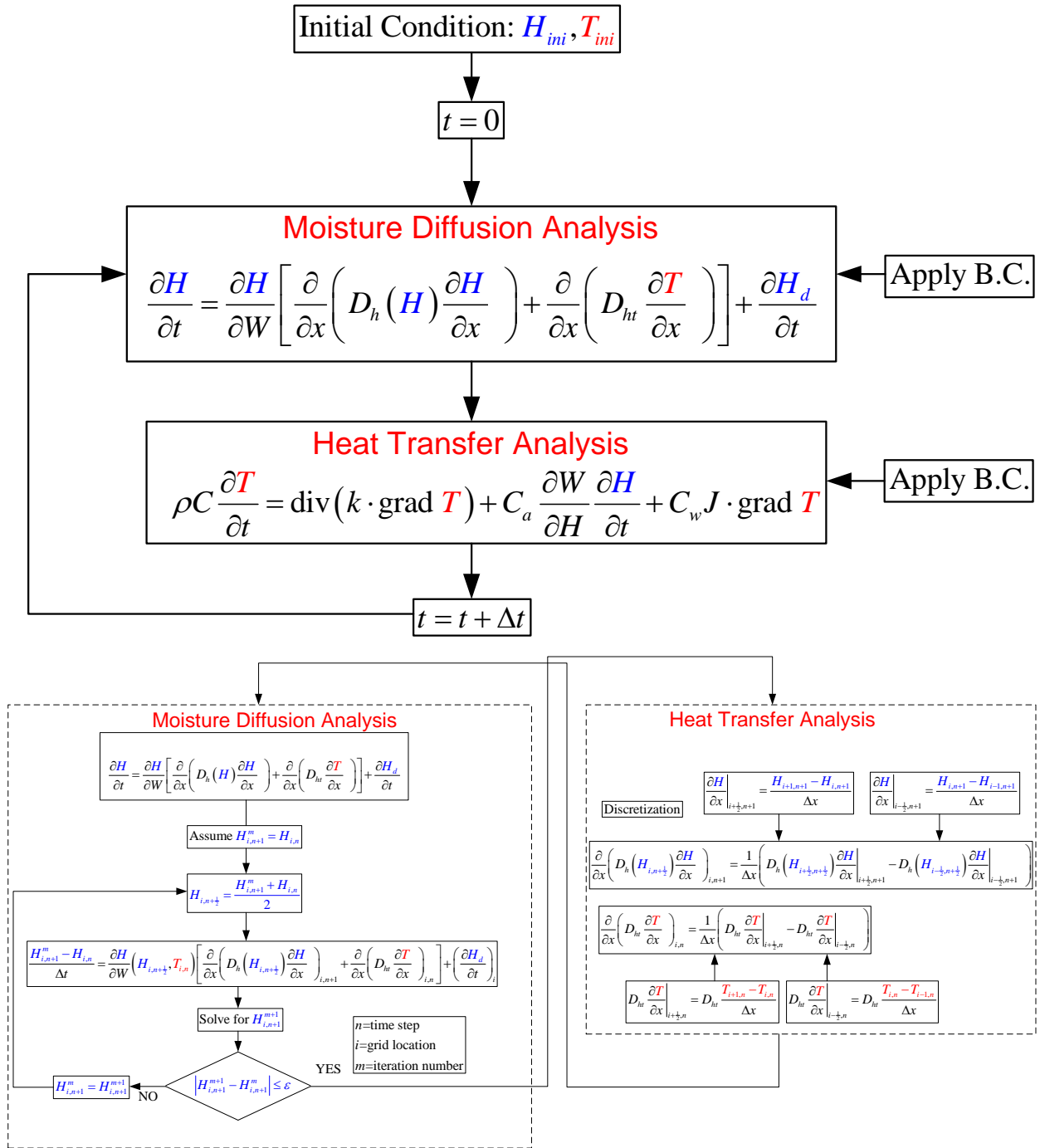


Fig. 1.20. Numerical solution of the coupled heat/moisture diffusion

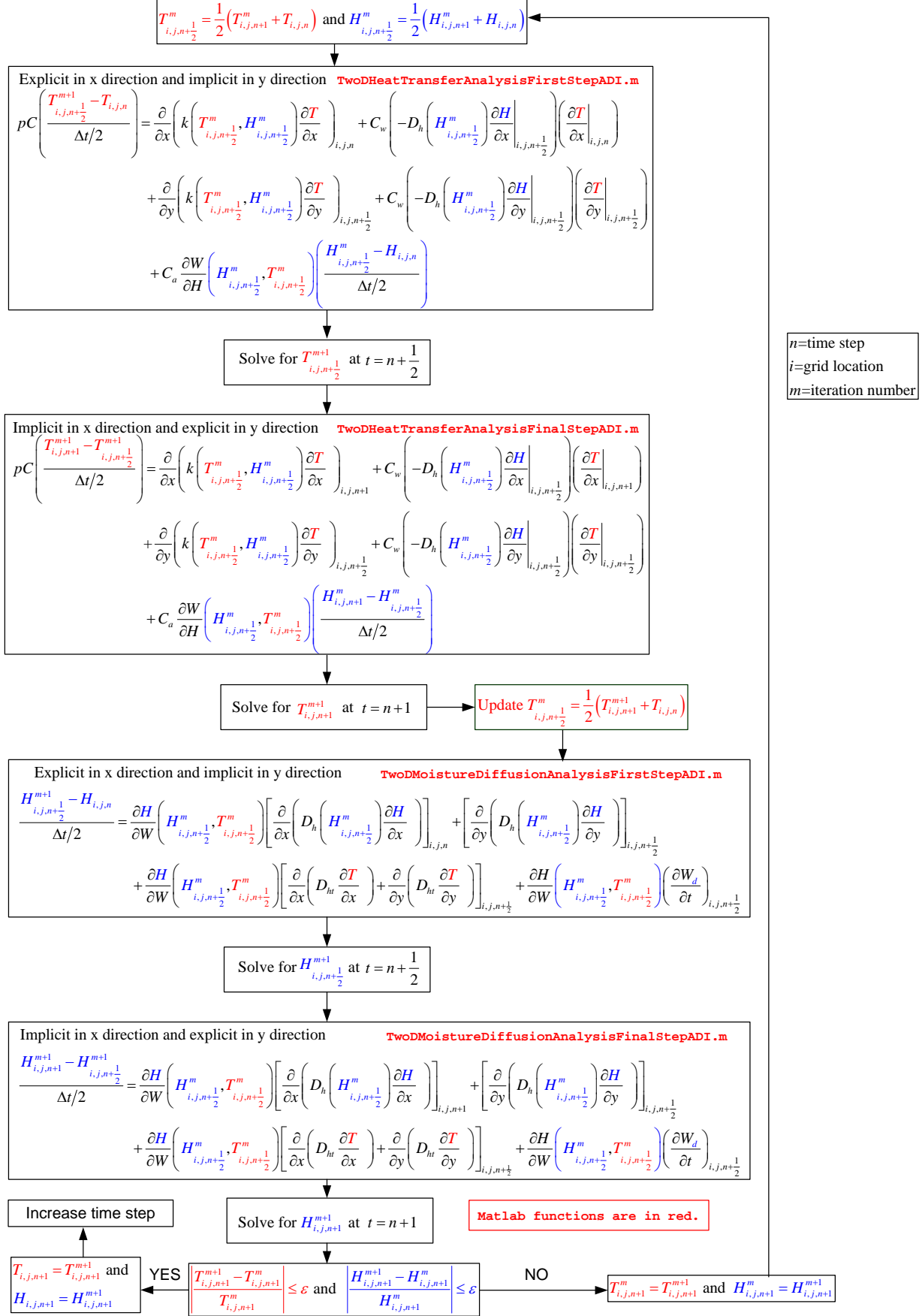


Fig. 1.21. Algorithm for Coupled Heat and MoistureDiffusion Analysis using ADI Method

1.3 PROBLEM VALIDATION

The examples given in (Holman 2010) will be used to validate the results obtained from the simulation of HTMC as follows.

1.3.1 VALIDATION CASE 1: 2D TRANSIENT HEAT CONDUCTION AND CONVECTION

1.3.1.1 Problem Description

A 1 by 2 cm ceramic strip is embedded in a high-thermal-conductivity material so that the sides are maintained at a constant temperature of 300°C . The bottom surface of the ceramic is insulated, and the top surface is exposed to a convection environment with $h = 200 \text{ W/m}^2 \cdot ^\circ\text{C}$ and ambient convection temperature on the top surface $T_a = 50^\circ\text{C}$. At time zero, the ceramic is uniform in temperature at 300°C . This transient heat transfer validation case can be shown in Fig. 1.22. We want to find the temperature distribution of the ceramic after a time of 12 s. For the ceramic, $\rho = 1,600 \text{ kg/m}^3$ and $C = 800 \text{ J/kg} \cdot ^\circ\text{C}$ and $k = 3 \text{ W/m} \cdot ^\circ\text{C}$.

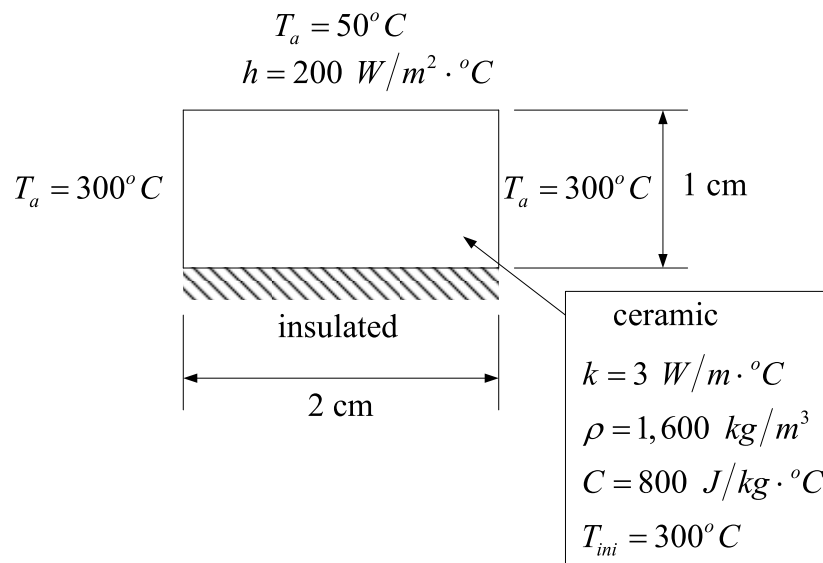


Fig. 1.22. Validation case 1: 2D Transient Heat Conduction and Convection

1.3.1.2 Numerical Solution

The ceramic strip was modeled using a 41 by 21 finite difference grids. By using a time step of 2 seconds, the temperature distribution at a time 12 seconds obtained from HTMC can be shown in Fig. 1.23.

After 12 seconds, the results of the temperature distribution at a distance of 0.5 cm and 1 cm from left side boundary of the ceramic obtained from HTMC were then compared with the results given in (Holman 2010) as shown in Table 1.7.

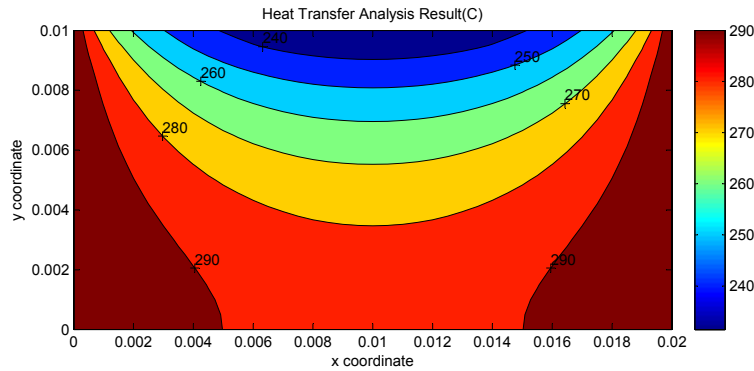


Fig. 1.23. Temperature distribution of the ceramic strip at a time 12 seconds

1.3.2 VALIDATION CASE 2: 2D TRANSIENT HEAT CONDUCTION, CONVECTION AND SURFACE IRRADIATION

1.3.2.1 Problem Description

A 1 by 2 cm ceramic strip is embedded in a high-thermal-conductivity material so that the sides are maintained at a constant temperature of 900 K. The bottom surface of the ceramic is insulated, and the top surface is exposed to a convection environment with $h = 50 \text{ W/m}^2 \cdot ^\circ\text{C}$ and ambient convection temperature on the top surface $T_a = 50^\circ\text{C}$. At time zero, the ceramic is uniform in temperature at 900 K. This heat transfer validation case can be shown in Fig. 1.24. We want to find the temperature distribution of the ceramic at the steady state. For the ceramic, $\rho = 1,600 \text{ kg/m}^3$ and $C = 800 \text{ J/kg} \cdot ^\circ\text{C}$, $k = 3 \text{ W/m} \cdot ^\circ\text{C}$ and the emissivity coefficient of the ceramic $\epsilon = 0.7$. Given: Stefan-Boltzman constant $C_s = 5.669 \times 10^{-8} \text{ W/m}^2 \cdot \text{K}^4$.

Table 1.7. Validation Summary of Case 1

Position	Grid Temperature (K)					
	0.5 cm from left boundary			1 cm from left boundary		
	Ref.	HTMC	% difference	Ref.	HTMC	% difference
Top surface	243.32	239.42	-1.602	231.97	231.47	-0.216
Center of the strip	279.87	279.29	-0.207	273.95	273.03	-0.336
Bottom surface	289.71	289.96	0.086	286.32	286.26	-0.021

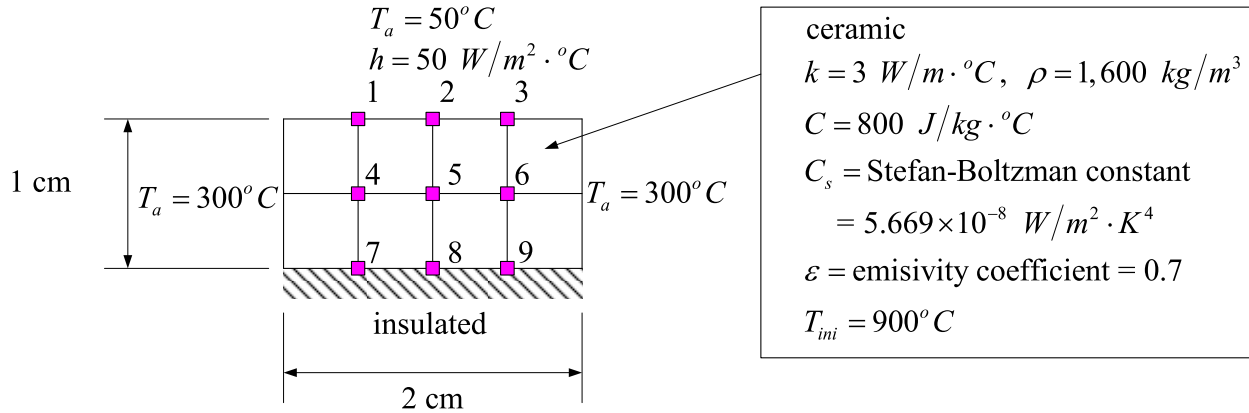


Fig. 1.24. Validation case 2: 2D Transient Heat Conduction, Convection and Surface Irradiation

1.3.2.2 Numerical Solution

The ceramic strip was modeled using a 5 by 3 finite difference grids. By using a time step of 2 seconds and simulate HTMC until the solution reaches the steady state. At steady state, the temperature distribution of the ceramic obtained from HTMC were then compared with the results given in (Holman 2010) as shown in Table 1.8.

Table 1.8. Validation Summary of Case 2

Grid No.	Grid Temperature (K)		% different
	Ref.	HTMC	
1	1020.879	1020.873	-5.88E-6
2	984.313	984.304	-9.14E-6
4	1092.369	1092.366	-2.75E-6
5	1064.212	1064.208	-3.76E-6
7	1111.384	1111.381	-2.70E-6
8	1087.798	1087.794	-3.68E-6

1.3.3 VALIDATION CASE 3: COUPLED HEAT AND MOISTURE DIFFUSION ANALYSIS MODEL

1.3.3.1 Problem Description

In this section, we will verify the developed numerical model (and code) by analyzing the large scale heated reinforced concrete experiment(MAQBETH) performed by the French Atomic Energy Commission (CEA Saclay) (Ranc et al. 2003). It models a prototype of a ring enclosing nuclear wastes in a typical waste disposal concept. This structure is constituted of a hollow cylinder with external diameter of 2.2 m and height of 3 m, Fig. 1.25 and 1.26, and it has undergone a thermal loading at 200 °C during several hundreds of hours.



Fig. 1.25. General view of MAQBETH mock-up (left) and cylindrical steel reinforcement (right) (Ranc et al. 2003)

1.3.3.2 Numerical Solution

Due to the geometrical and loading symmetry conditions, only half of the structure is modelled in a 2D axisymmetric model used in the htmc program which is the same way as the one in Benoit et al. (2012). The initial temperature inside the concrete is 20°C and initial relative humidity inside the concrete is 0.96. The boundary conditions imposed in the simulations and the thermal loading applied on the inner surface are indicated on Fig. 1.27 Benoit et al. (2012). The constant vapour pressure prescribed at both internal and external surfaces are equal to 2500 Pa. The loading temperature indicated on Fig. 1.27 is directly applied on the internal surface as constant boundary conditions, while a constant exterior temperature of $T_{ext} = 20^{\circ}\text{C}$ and an equivalent convective (h) condition prescribed at the external one is equal to $10\text{W}/\text{m}^{\circ}\text{C}$.

After running the simulation, the result shows that the moisture diffusivity of concrete model proposed by Bazant and Najjar (1972), using the parameters list in Table 1.9, gives the best fit of the experimental results Ranc et al. (2003) as shown in Fig.1.28 to 1.31.

Table 1.9. Parameter used in the moisture diffusivity of concrete model proposed by Bazant and Najjar (1972)

Parameter	Value
D_1 (m^2/s)	3×10^{-10}
n	6
Mass of (anhydrous) cement per m^3 of concrete	388

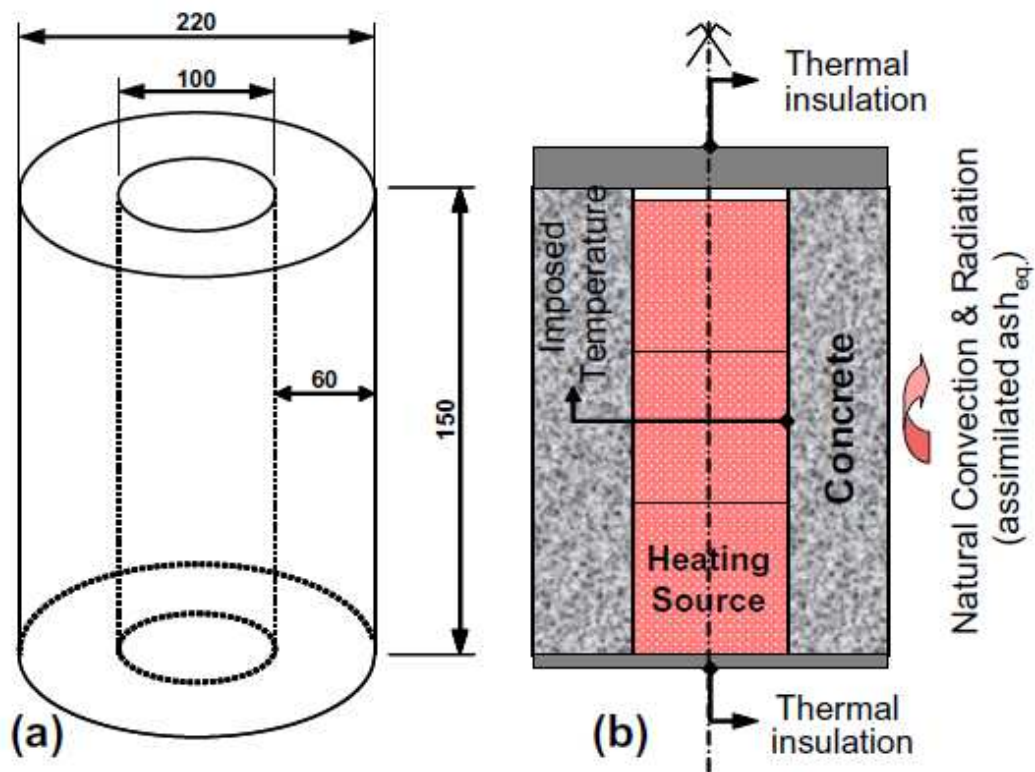


Fig. 1.26. Geometrical characteristics of MAQBETH mock-up (concrete hollow cylinder) (a), schematic description of experimental conditions (b) (Ranc et al. 2003)

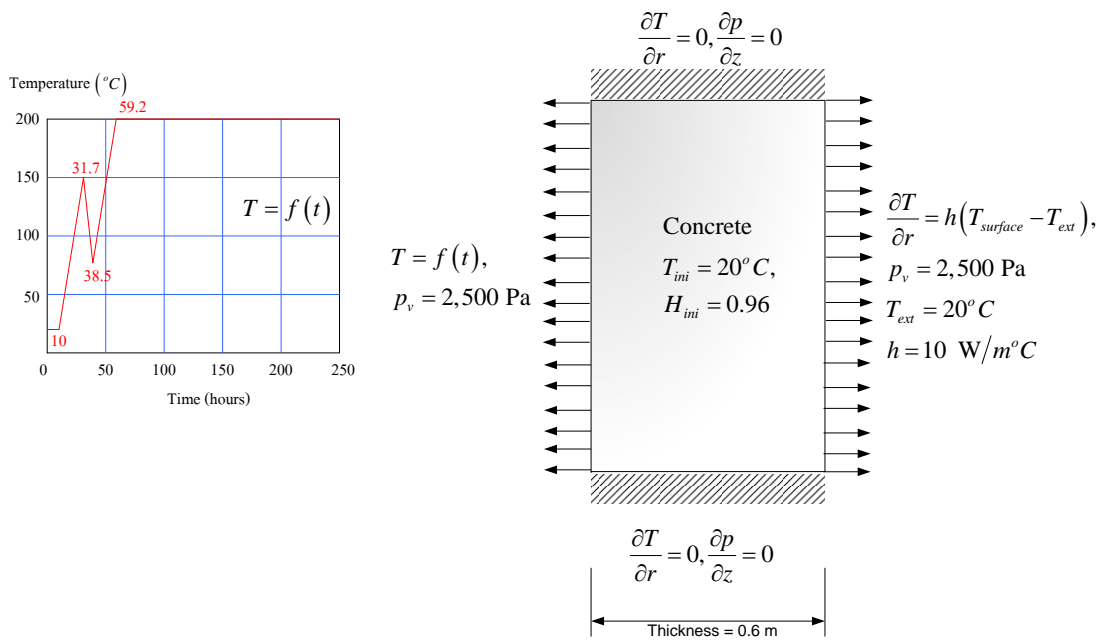


Fig. 1.27. Scheme of axisymmetrical numerical model

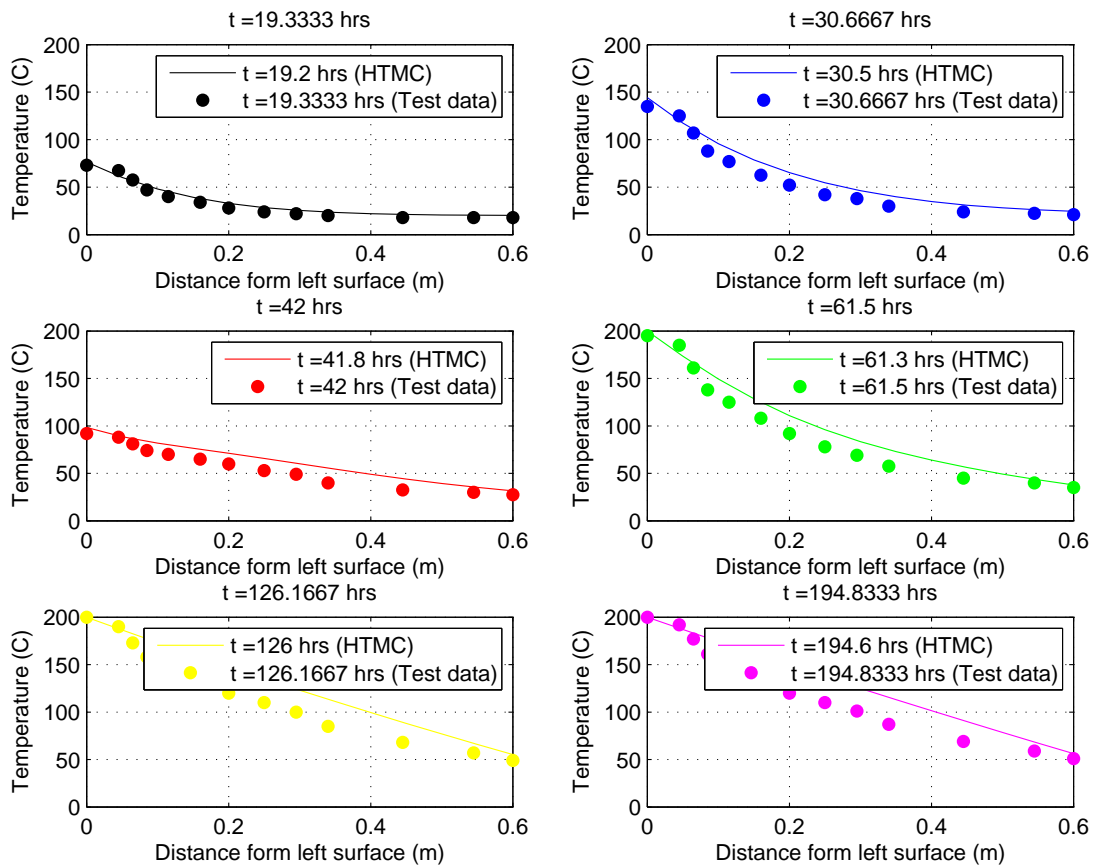


Fig. 1.28. Experimental and numerical profiles of temperature as a function of the distance from the left concrete surface at different times.

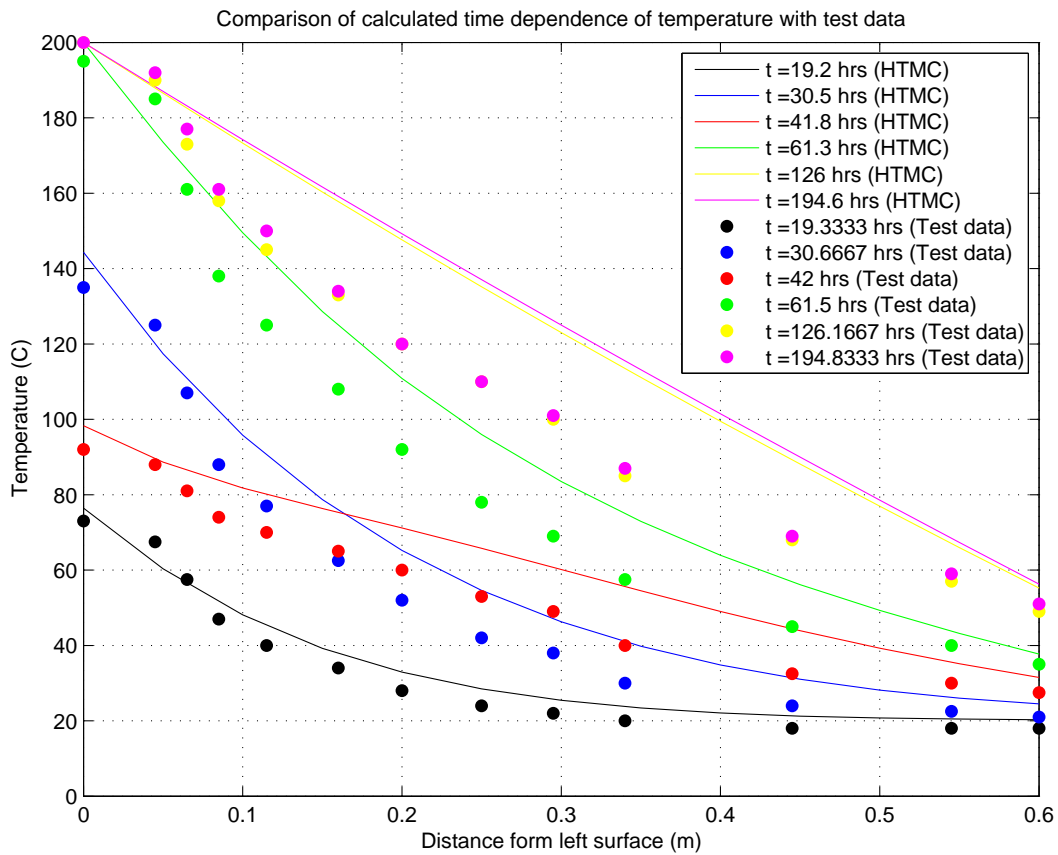


Fig. 1.29. Experimental and numerical profiles of temperature as a function of the distance from the left concrete surface at different times.

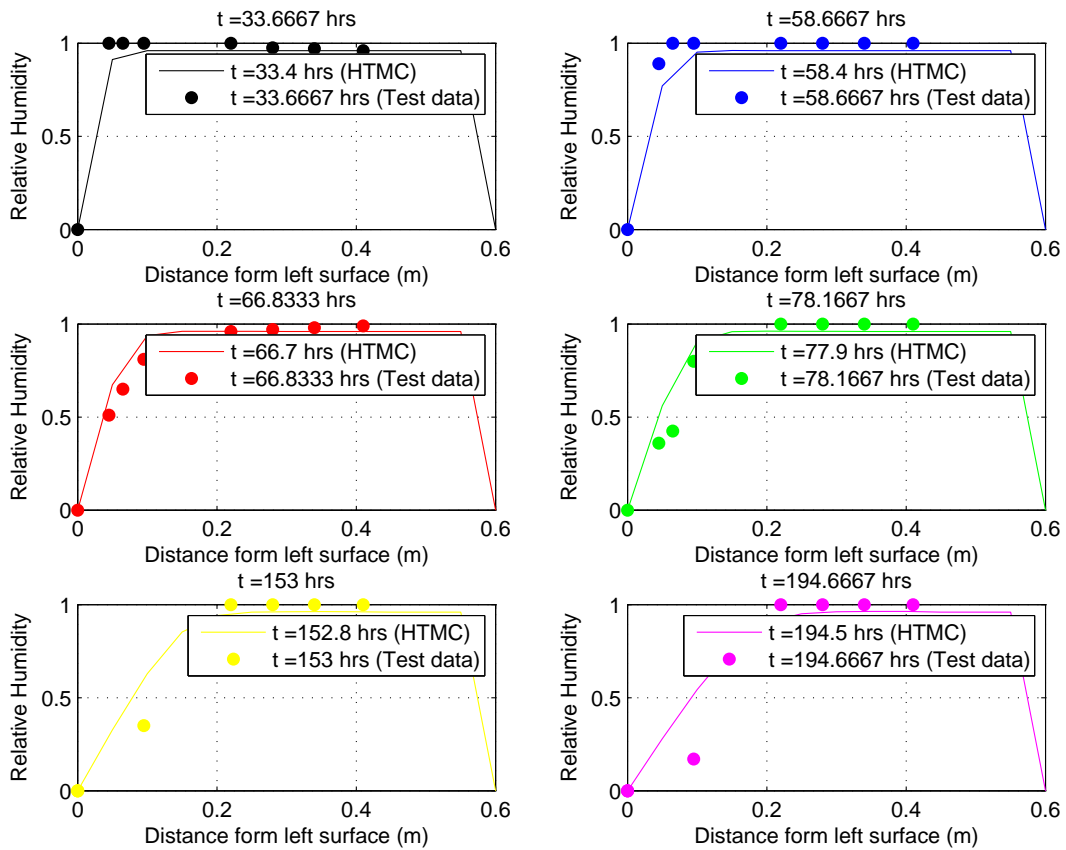


Fig. 1.30. Experimental and numerical profiles of relative humidity as a function of the distance from the left concrete surface at different times.

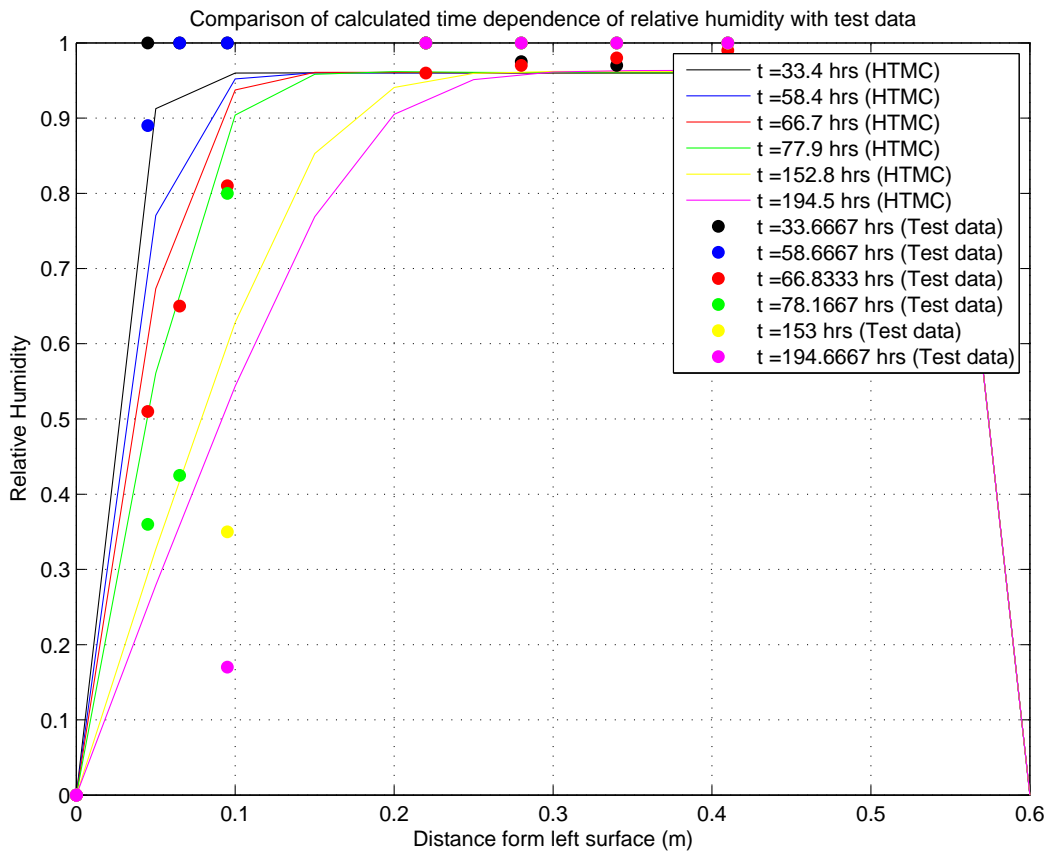


Fig. 1.31. Experimental and numerical profiles of relative humidity as a function of the distance from the left concrete surface at different times.

1.4 USER'S MANUAL

This manual is for the `htmc` program (Heat Transfer and Moisture diffusion analysis in Concrete). It is the matlab code used for performing

1. Heat transfer analysis in concrete
2. Moisture diffusion analysis in concrete
3. Coupled heat transfer and moisture diffusion in concrete

1.4.1 PROGRAM OPERATION

To execute the `htmc` code, the user must:

1. Copy the folder of the `htmc` code into the directory where the user wants it to be.
2. Run Matlab program.
3. Set Matlab directory to be the one where the `htmc` code is located in the first step (Fig.1.32).
4. Open the `input.xls` which is in the same directory as the code to edit the input data and then save the `input.xls` file.
5. Type `htmc` on the Command Window in the Matlab program as shown in Fig.1.32 to run the program.
6. Matlab will then call `htmc` code to run.
7. After finish running the code, the Matlab will show the resulting plot. The user can obtain the results of the simulation from the output files and also its figures in the same directory where the code is.

1.4.2 INPUT FILE PREPARATION

The input file of the `htmc` code is an excel file named 'input.xls' which locates in the same folder where the `htmc` is. To edit the input file, first open the `input.xls` file from Windows Explorer. There are 8 sheets inside this input file. The `htmc` is coded in the way that Matlab will read each input at specific location of the cell in the excel file. Therefore, the user should not insert or delete any line in the excel input file. Table 1.10 shows the list of the m-file which read the specific sheet in the `input.xls` file.

`input.xls` is shown in Fig.1.33. From Fig.1.33, there are 4-5 columns in each sheet of the input file. The first column gives the description of the parameters used in the analysis models. The second column of the sheet gives the name of the Matlab variable used in the code. The third column is the value of the parameter used in the analysis model. All cells in this column will be in yellow. This is where the user needed to edit the value of the parameters used in the models. The forth column shows the unit of each parameter. Finally, the last column explains the option that the user can edit the value of each parameter.

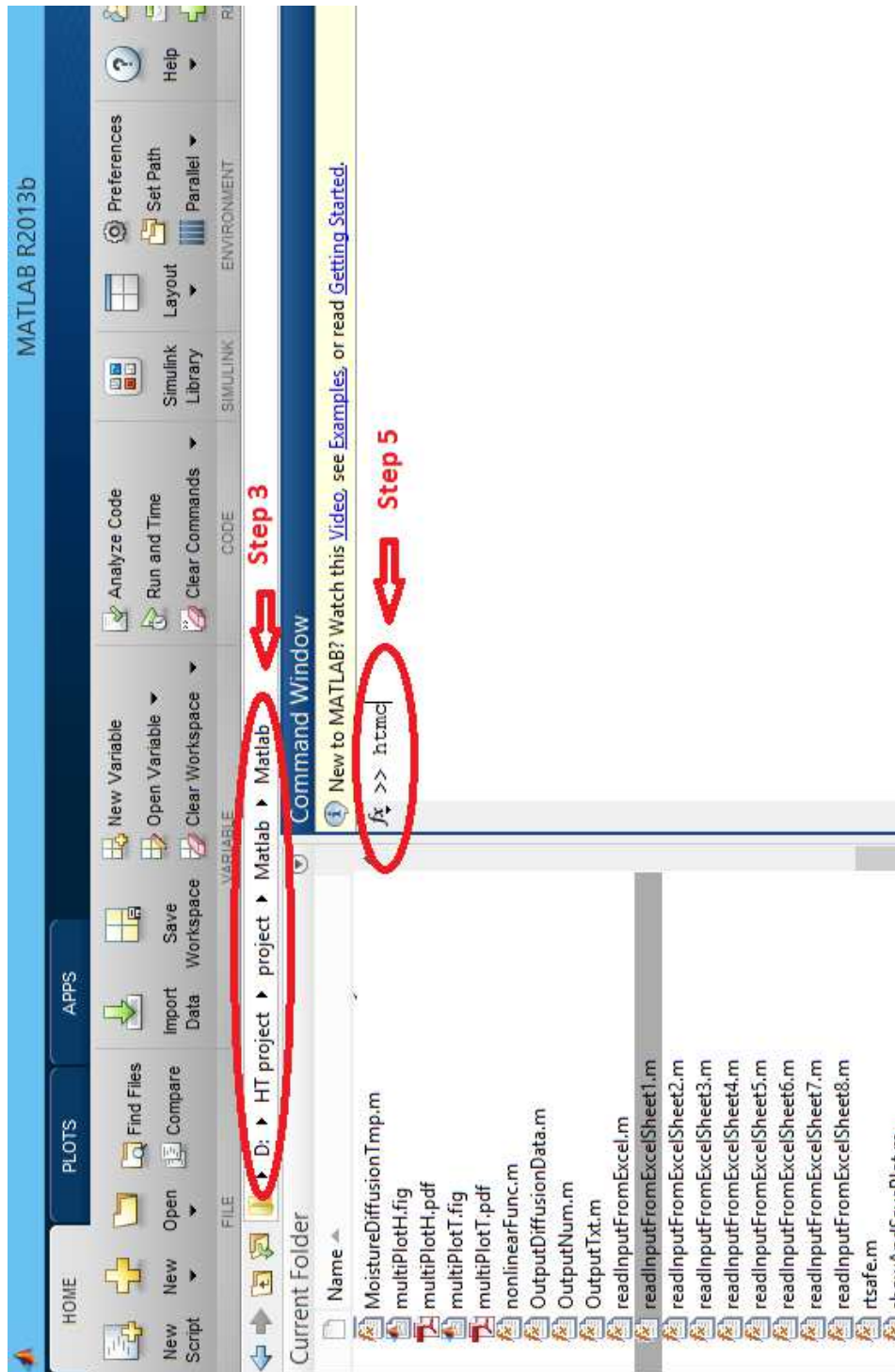


Fig. 1.32. How to run htmc code

input [Compatibility Model] - Microsoft Excel

Home Insert Page Layout Formulas Data Review View Developer Add-Ins Acrobat

Clipboard: Paste, Cut, Copy, Format Painter, Font (Tahoma, 11, Bold, Italic, Underline, Color, Background Color, Paragraph (Align, Indent, Bullets, Numbering, Merge & Center), Styles (Conditional Formatting, Format, Cell, Table, Styles), Cells (Insert, Delete, Format, Fill, AutoSum, Sort & Find & Filter, Select, Editing)

A73 Type of relative humidity at the boundary (if Einput.m_env_h_bc_boundary = 1), if defined value of Einput.m_envHBoundaryType is 1, please prepare values in

1	A	B	C	D	E	
name	variable name in matlab	value	unit	remark		
2	Finite Difference Input Data					
3	Analysis model	Einput.m_model	3	1 -> heat transfer analysis, 2 -> moisture diffusion analysis, 3 =		
4	Width of the rc structure	Einput.m_W	0.6	m		
5	Height of the rc structure	Einput.m_H	0.6	m		
6	No. of grid in the horizontal direction	Einput.m_N	13			
7	No. of grid in the vertical direction	Einput.m_M	13			
8	Time step	Einput.m_timeStep	600	seconds		
9	No. of time steps	Einput.m_numberOfTimeStep	1200	steps		
10	Convergence criteria	Einput.m_convergenceCriteria	0.1	%		
11	Total number of iteration	Einput.m_totalNumberOfIteration	100			
12	Heat Transfer Analysis Input Data					
13	Select thermal capacity model	Einput.m_TDiffModel	2	0->k and rhoC are constant, 1->normal strength concrete (NSC, A 1992),2->High strength concrete (HSC,Kodur et al, 2004),3->NSC 2, 2004, 4-> user 's defined (Kim's model for k)		
14	Density of concrete	Einput.m_rho	2360	kg/m^3		
15	Specific heat of concrete	Einput.m_C	1100	J/(kg.C)		

Ready

Experiment Result H Experiment Result T Experiment Result T Experiment Result H

Mensis Model Xi's model Bazant's Model

Output and Plot

11:16 5/9/2557

Fig. 1.33. Input.xls file

Table 1.10. List of the m-file which read the specific sheet in the input .xls file

Sheet No.	Sheet Name	Matlab File
1	Input	readInputFromExcelSheet1.m
2	Define b.c.	readInputFromExcelSheet2.m
3	Xi's Model	readInputFromExcelSheet3.m
4	Mensi's Model	readInputFromExcelSheet4.m
5	Bazant's Model	readInputFromExcelSheet5.m
6	Experimental Result T	readInputFromExcelSheet6.m
7	Experimental Result H	readInputFromExcelSheet7.m
8	Output and Plot	readInputFromExcelSheet8.m

1.4.2.1 Sheet 1: Input

There are 3 parts that the user can edit;

Finite Different Input: In this part the user must edit the value of each parameter in the yellow area:

1. Analysis Model: There are 3 options to be selected, i.e., 1 is for heat transfer analysis, 2 is for moisture diffusion analysis and 3 is for coupled heat transfer and moisture diffusion analysis.
2. Geometry of the structure: The user must specify the height and the width of the concrete structure to be modeled. The unit is in meter.
3. Finite different information: The user must specify the number of grids in horizontal and vertical, the time step (in seconds), the total number of time step used in the simulation. For moisture diffusion analysis and coupled problem, the convergence criteria and also the total number of iteration must be specified since both problems need iteration process.

Heat Transfer Analysis Input

1. Model of Heat Capacity: There are 5 options to be selected, i.e., 0 is for constant heat capacity (ρC is constant), 1 is for heat capacity of normal strength concrete (NSC, ASCE Manual 1992), 2 is for heat capacity of high strength concrete (Kodur et al. 2004) (ASCE 1992) (HSC, 3 is for heat capacity of normal strength concrete and high strength concrete (Eurocode 2004) and 4 is for user's defined (Kim et al. 2003) for k).
2. Concrete's Properties
3. Initial Condition of Temperature Inside The Concrete
4. Boundary Condition: There are 3 types of boundary conditions can be applied as follows;
 - No flux b.c.
 - Constant b.c.: For constant boundary condition, there are 2 options that the user can select. 1) Constant temperature at the boundary and 2) Varying temperature at the boundary. If varying temperature at the boundary is selected, the user must prepare the varying temperature data at each boundary in Sheet2: Define b.c.
 - Convection b.c.: For this type of boundary condition, the user can apply 1) convection 2) irradiation. The user can also, specify 2 options for convection coefficient and temperature at each boundary to be constant or varying. If either of them is set to be varying, the user must prepare the varying of that data at each boundary in Sheet2: Define b.c.

Moisture Diffusion Analysis Input

1. Diffusivity Model: There are 3 options of the moisture diffusivity models to be selected, i.e., 1 is for Xi, Bazant and Jennings (1994), 2 is for Mensi et al. (1988) and 3 is for Bazant's model (1972). User needs to prepare the input parameters in Sheet 3: Xi's Model, Sheet 4: Mensi's Model, and Sheet 5: Bazant's Model if the selected model is 1, 2 and 3, respectively.
2. Initial condition of relative humidity inside the concrete
3. Diffusivity factor for high strength concrete: This parameter is used for high strength concrete. The diffusivity of high strength concrete is equal to this factor multiplied by the diffusivity of the normal concrete.
4. Coefficient of moisture diffusion due to temperature gradient: This parameter is used in the coupled heat transfer and moisture diffusion in concrete.
5. Boundary Condition: There are 2 types of boundary conditions that can be applied as follows;
 - No flux b.c.
 - Constant b.c.: For constant boundary condition, there are 2 options that the user can select. 1) Constant relative humidity at the boundary and 2) Varying relative humidity at the boundary. If varying relative humidity at the boundary is selected, the user must prepare the varying relative humidity data at each boundary in Sheet 2: Define b.c.

1.4.2.2 Sheet 2: Define b.c.

When temperature, coefficient of convection and relative humidity is set to be varied at each boundary of the concrete in Sheet 1: Input, user must prepare the data at each time step to be applied at each boundary. User must prepare variable data and range of variable data which is the range of the excel cell containing each variable data at each boundary as shown in Fig.1.34.

1.4.2.3 Sheet 3: Xi's Model

This sheet contains all parameters used to compute the moisture diffusivity of the concrete using Xi's model.

1.4.2.4 Sheet 4: Mensi's Model

This sheet contains all parameters used to compute the moisture diffusivity of the concrete using Mensi's model.

1.4.2.5 Sheet 5: Bazant's Model

This sheet contains all parameters used to compute the moisture diffusivity of the concrete using Bazant's model.

1.4.2.6 Sheet 6: Experimental Result T

This sheet contains all information of the experimental data for temperature at specific location in concrete and at specified time. User must prepare this experimental data, location and time. Also, user must specify range of the cell containing all of those data as shown in Fig.1.35.

A		B		C		D		E	
Data for applying varying values at the boundary									
1	2	3	4	5	6	7	8	9	10
name	variable name in matlab	value	remark						
3	Define varying temperature at the boundary (if Einput.m_TaBoundaryType =1)								
4	Range of temperature values on left boundary (top boundary, boundary 1)	Einput.m_TaBoundary1Vector	B21:B1221						Please specified cell of varying temperature at the boundary (please prepare one data more
5	Range of temperature values on left boundary (top boundary, boundary 2)	Einput.m_TaBoundary2Vector	C21:C1221						Please specified cell of varying temperature at the boundary (please prepare one data more
6	Range of temperature values on left boundary (top boundary, boundary 3)	Einput.m_TaBoundary3Vector	D21:D1221						Please specified cell of varying temperature at the boundary (please prepare one data more
7	Range of temperature values on left boundary (top boundary, boundary 4)	Einput.m_TaBoundary4Vector	E21:E1221						Please specified cell of varying temperature at the boundary (please prepare one data more
20	time step	m_TaBoundary1Vector	m_TaBoundary2Vector	m_TaBoundary3Vector	m_TaBoundary4Vector				
21	1			20.0					
22	2			20.0					
23	3			20.0					
24	4			20.0					
25	5			20.0					
26	6			20.0					
27	7			20.0					
28	8			20.0					
29	9			20.0					
30	10			20.0					
31	11			20.0					
32	12			20.0					
33	13			20.0					

Fig. 1.34. Sheet 2: Define b.c.

	A	B	C	D	E	F	G	H	I	J	K	L	M	N	O
1	name	variable name in matlab	range of data	remark											
2	Experimental Results of T in C (Bary-2012)	Einput.T_at_vPt	B8:N13	need data in green cells											
3	Position from left surface (m)	Einput.m_vPt	B7:N7	need data in blue cells											
4	Time recorded (hrs)	Einput.m_tExp	A8:A13	need data in yellow cells											
5															
6															
7	Time (hrs) , Einput.m_tExp	0	0.045	nos from left surface (m)	Einput.m_vPt	0.115	0.16	0.2	0.25	0.295	0.34	0.445	0.545	0.6	
8	19.2	73	67.5	57.5	47	40	34	28	24	22	20	18	19	18	
9	30.5	135	125	107	88	77	62.5	52	42	38	30	24	22.5	21	
10	41.8	92	88	81	74	70	65	60	53	49	40	32.5	30	27.5	
11	61.3	195	185	161	138	125	108	92	78	69	57.5	45	40	35	
12	126	200	190	173	158	145	133	120	110	100	85	68	57	49	
13	194.6	200	192	177	161	150	134	120	110	101	87	69	59	51	
14															
15															
16															
17															
18															
19															
20															
21															
22															
23															
24															
25															
26															
27															

Fig. 1.35. Sheet 6: Experimental Result of Temperature

1.4.2.7 Sheet 7: Experimental Result H

This sheet contains all information of the experimental data for relative humidity at specific location in concrete and at specified time. User must prepare this experimental data, location and time. Also, user must specify range of the cell containing all of those data as shown in Fig.1.36.

1.4.2.8 Sheet 8: Output and Plot

This sheet contains the options for saving the output files, showing the results of the simulation using Matlab plot and saving the figure of the matlab plot.

1. Output Files: User have an option to save the output file and also can specify the name of the output files.
2. Record Data: User can specify the time step of where the user want to record the result of simulation and then verify with the experimental data from Sheet 6 and 7. User must prepare the time step that the user want to record the result of simulation and also provide the range of excel cell that contain all of the time steps prepared before as shown in Fig.1.37.
3. Matlab Plot: User can define the program to show or not to show the Matlab figure after the simulation finished. User can set the size of the Matlab figures, all information of the plot including title, label on the both axes, minimum and maximum values of both axes and the font size used in the plot. There are two types of plot can be generated. 1) Multiple plot shows individual plot at each specified time 2) Summary plot shows all all data at every specified time in one plot.
4. SavePlot: User can save the Matlab plot as figure files. The file extension of the figure can be .pdf, .bmp, .jpg, .eps and fig. The saving figures will be generated at the end of the simulation and will be in the same directory where the program locates.

1.4.3 OUTPUT

There are three types of output that htmc code can show as follows;

1.4.3.1 Output files

After finish running htmc code on Matlab, the code will generate the output files in the same folder where the code locates. The file extension of the output files is .out and they contain the results of the simulation at each finite different grid point in every time step. The user can later use notepad program to open them. An example of the output file can be shown in Fig.1.38

1.4.3.2 Matlab plots

User can show Matlab plots after finish running the htmc code by set the value of showing the Matlab plot to be 'on' in last excel sheet of the input.xls file. An example of the Matlab plots can be shown in Fig.1.39

	A	B	C	D	E	F	G	H	I	
1	name	variable name in matlab	range of data	remark						
2	Experimental Results of H (Bary-2012)	Einput.rh_at_vrPt(Einput.m_rtExp,Einput.m_vrPt)	B8:I13	need data in purple cells					Data for Einput.m_vrPt	
3	Position from left surface (m)	Einput.m_vrPt	B7:I7	need data in orange cells						
4	Time recorded (hrs)	Einput.m_rtExp	A8:A13	need data in pink cells						
5										
6										
7	Time (hrs) , Einput.m_rtExp	0	pos from left surface (m), Einput.m_vrPt	0.045	0.065	0.095	0.22	0.28	0.34	0.41
8	33.4	0	1	1	1	1	1	0.975	0.97	0.96
9	58.4	0	0.89	1	1	1	1	1	1	1
10	66.7	0	0.51	0.65	0.81	0.96	0.97	0.97	0.98	0.99
11	77.9	0	0.36	0.425	0.8	1	1	1	1	1
12	152.8	0			0.35	1	1	1	1	1
13	194.5	0			0.17	1	1	1	1	1
14										
15										
16										
17										
18										
19										
20										
21										
22										
23										
24										
25										
26										
27										

Fig. 1.36. Sheet 6: Experimental Result of Relative Humidity

	A	B	C	D
13	Set Figure Windows Size	<code>Einput.m_setFigSize</code>	1	0->Screen size, 1->user's define
14	Set Width of Figure Windows Size (if m_setFigSize = 1)	<code>Einput.m_figWidth</code>	25	Unit in centimeters
15	Set Height of Figure Windows Size (if m_setFigSize = 1)	<code>Einput.m_figHeight</code>	20	Unit in centimeters
16	2.2 Temperature Plot Options			
17	Specified Time Step for recording temperature data	<code>Einput.m_recordStepT</code>	B18:G18	Cell containing range of specified time step
18	Specified Time step for recording temperature data, <code>Einput.m_recordStepT</code>	115	183	fill time step in the orange area
19	Specified Time for recording temperature data (hrs)	19.17	30.50	41.83
20	Title	<code>Einput.m_titleT</code>	Comparison of calculated time dependence of temperature with test data	
21	Label on x axis	<code>Einput.m_xlabelT</code>	Distance form left surface (m)	
22	Label on y axis	<code>Einput.m_ylabelT</code>	Temperature (C)	
23	Font size	<code>Einput.m_fontSizeT</code>	14	Specified time step for recording simulation daat
24	Minimum value of x axis	<code>Einput.m_Xmin_T</code>	0	
25	Maximum value of x axis	<code>Einput.m_Xmax_T</code>	0.6	
26	Minimum value of y axis	<code>Einput.m_Ymin_T</code>	0	
27	Maximum value of y axis	<code>Einput.m_Ymax_T</code>	250	
28	2.3 Relative humidity Plot Options			
29	Specified Time Step for recording relative humidity data	<code>Einput.m_recordStepH</code>	B30:G30	fill time step in the orange area

Fig. 1.37. Sheet 6: How to prepare the input for saving the result at specified time step in Sheet 8: Output and Plot

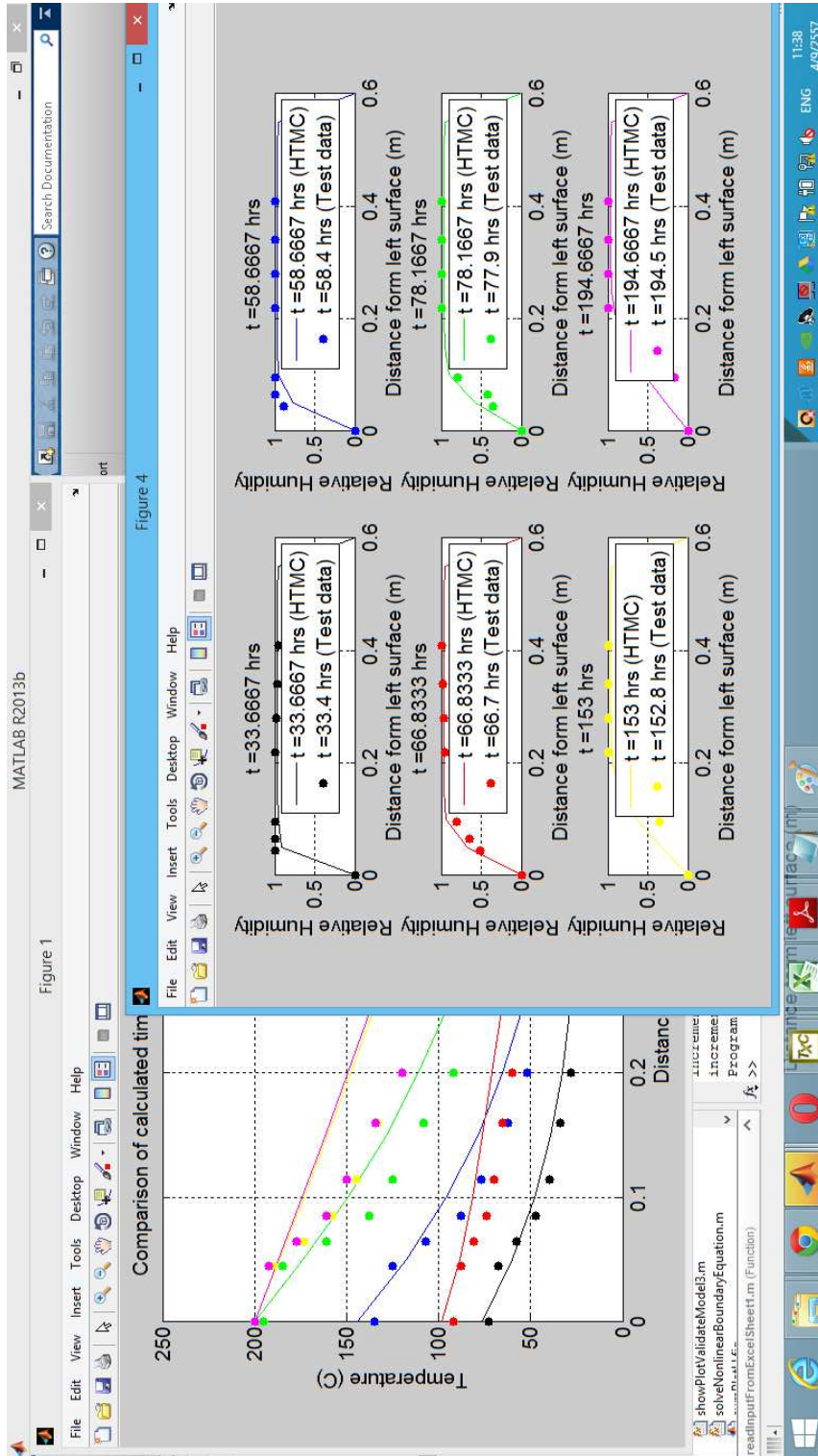


Fig. 1.39. Example of the Matlab plots generated by htmc code

1.4.3.3 Figure files

User can save the results of the simulation from Matlab plots into files. There are five types of figure's file extension which can be saved. There are pdf, bmp, jpg, eps and fig. The figure will be saved in the same folder where the code locates.

2 FINITE ELEMENT SIMULATIONS OF ASR EXPANSION

2.1 INTRODUCTION

Alkali-Silica Reaction (ASR) is a deleterious reaction in concrete which causes long term swelling of the concrete and is very likely to affect the structural integrity of the structure (serviceability/cracking and/or strength).

While many concrete dams have been reported to be affected by Alkali-Aggregate Reaction (AAR), no instance of AAR in nuclear power plants has been reported until recently: Ikata No.1, Shihoku Electric Power, Japan (Murazumi et al., 2005), Gentilly 2, Canada (Orbovic, 2011), and Seabrook, NH (NRC, 2012). Yet, AAR has seldom, if ever, been investigated in connection with the safety of the reactor (as opposed to dams).

Addressing the complexity of nuclear structures requires a gradual approach. The aim of this report is to step by step analysis of a reinforcement concrete (RC) panel and a RC beam as part of a nuclear power plant suffering from ASR as shown in figure 2.1. Different models and assumption are considered for finite element modeling of the RC beam. In particular, the effects of biaxial confinement resulting from structural constraint is investigated. The results of the various models are then compared to each other.

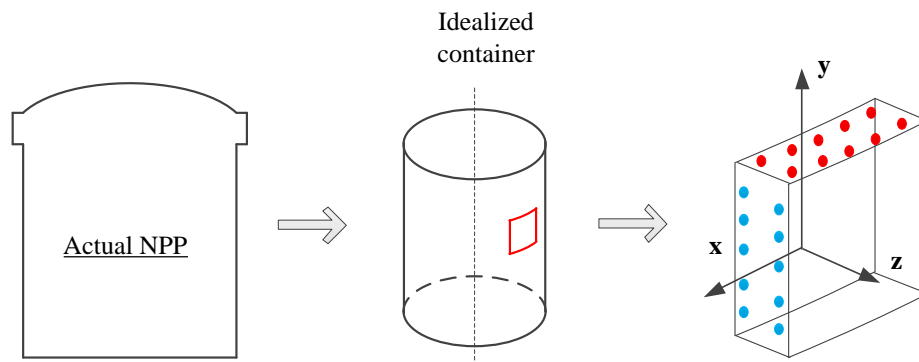


Fig. 2.1. Schematic view of the actual NPP, its idealized cylinder, and the cutted segment

2.2 CASE STUDY I: RC PANEL

The first case study is a RC panel with the dimensions as shown in figures 2.2 and 2.3. This structural member corresponds to the preliminary design of a structural mockup developed by the University of Tennessee in Knoxville. The aim of that mockup is to study the effect of structural confinement on the

expansion in the unconstrained direction and damage development of a thick reinforced concrete structure. Two groups of reinforcements are at the top and bottom of the panel in the y- and x-directions. Figure 2.4 shows the plan view of the testing frame. It includes the main specimen (RC panel in this case), concrete cushion ring, and the steel frame. The steel girder frame is designed to restrain the ASR-induced deformations in two directions although it cannot not fully prevent them practically. However strictly speaking, more stringent boundary conditions are applied for the simulation: The RC panel has a degree of restriction on x-z and y-z planes; but, it is free of external displacement boundary condition on the x-y plane. On the x-z and y-z planes the main RC panel is surrounded by a concrete cushion ring with the compressive strength of $f'_c=10000 \text{ psi}$ (68.948 MPa) as shown in figure 2.5. It should be noted that the rebars in the main specimen are continuous in the cushion ring.

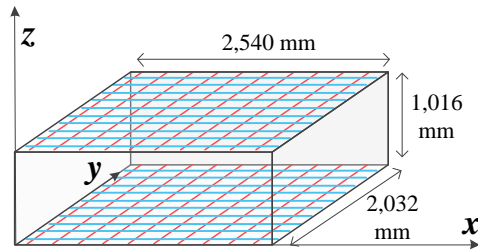


Fig. 2.2. General view of the RC panel

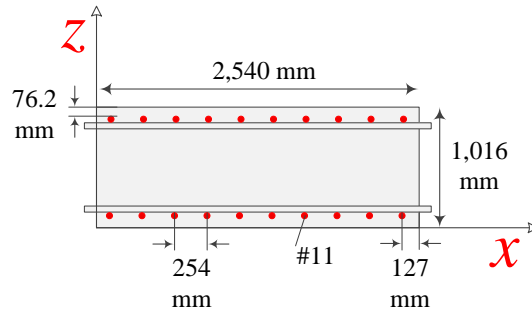


Fig. 2.3. Elevation view of panel in x-z plane

2.2.1 MATERIAL PROPERTIES

This section explains the material properties which are used in the current research for assessment of RC panel. In general, material properties and modeling characteristics can be divided into the following major groups:

- Concrete panel properties
- Cushion ring properties

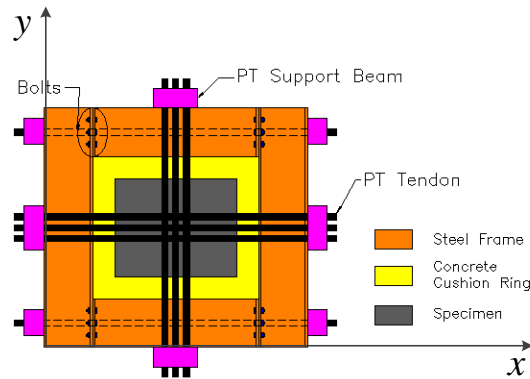


Fig. 2.4. Plane view of the test setup at UTK

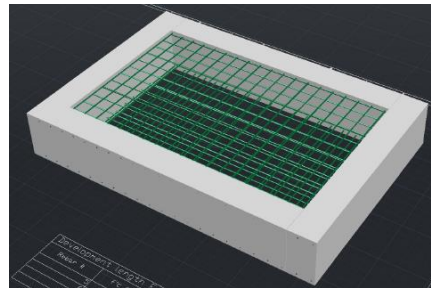


Fig. 2.5. Concrete cushion ring for the test at UTK

- Steel rebar properties
- ASR model properties

2.2.1.1 Concrete panel properties

General characteristics of the concrete used for the panel are summarized in table 2.1. Mass density of the concrete is obtained from the concrete formulation. The mix constituents are listed in table 2.2.

Table 2.1. General characteristics of concrete panel

Characteristics	Symbol	Unit	Mean	STD	min	max
Mass density	ρ	kg/m ³	2,250	225	1,800	2,700
Compressive strength	f'_c	MPa	-31	3.1	24.82	37.24
Tensile strength	f'_t	MPa	3.2	0.32	2.56	3.84
Elastic modulus	E	MPa	26,000	2,600	20,800	31,200
Poisson's ratio	ν	-	0.2	0.02	0.16	0.24

It is noteworthy that due to uncertainty in the material properties an appropriate range is considered for

them. It is assumed that the material properties follows the normal distribution. Thus, the properties are expressed using a mean and associated standard deviation. Also, an upper and lower bounds are limited the considered distributions. Obviously, sensitivity analysis is required to cover the relative importance of the parameters and also their property range.

Table 2.2. Concrete mixture for the RC panel.

Component	Quantity
Coarse aggregate (SSD)	917kg/m ³
Fine aggregate (SSD)	674kg/m ³
Cement (Type III)	420kg/m ³
Water	231kg/m ³
W/C ratio	0.55
NaOH added	2.43kg/m ³
Total Na ₂ O _e	5.25kg/m ³

The value of the concrete compressive strength is provided as 4500 psi or 31.03 MPa. Using this value, the elastic modulus of the concrete can be estimated using the approximate formulas proposed by ACI Building Code 318-83 as follows:

$$E_c = 4.7f'_c{}^{0.5} \Rightarrow \text{Normal weight concrete} \quad (2.1)$$

$$E_c = 43\rho^{1.5}f'_c{}^{0.5} \times 10^{-6} \Rightarrow 1500\text{kg/m}^3 < \rho < 2500\text{kg/m}^3 \quad (2.2)$$

Using the above formulations, the modulus elasticity of concrete is estimated around 26,000 MPa based on ACI method (ACI Building Code 318-83).

There are many equations from the literature which connect the concrete compressive to the tensile strength. In the present study the relations proposed by Raphael for static and dynamic loading conditions are used. These relations can be summarized as follows (also shown graphically in figure 2.6):

$$(f'_t)_{st} = 1.7(f'_c)^{2/3} \quad (2.3)$$

$$(f'_t)_{st}^{app} = 2.3(f'_c)^{2/3} \quad (2.4)$$

$$(f'_t)_{dyn} = 2.6(f'_c)^{2/3} \quad (2.5)$$

$$(f'_t)_{dyn}^{app} = 3.4(f'_c)^{2/3} \quad (2.6)$$

where both the f'_t and f'_c are represented in psi. We recall that 1 MPa = 145.04 psi. In the present study, static strengths are assumed.

2.2.1.2 Cushion ring properties

As mentioned before, the cushion ring is used only as a boundary condition for the main RC panel. The compressive strength of the concrete is $f'_c = 68.948$ MPa.

2.2.1.3 Steel rebar properties

In the United States, rebar is graded according to its physical characteristics. The higher the grade, the wider and heavier the rebar is. #11 rebar is among the widest and heaviest of the available standard grades,

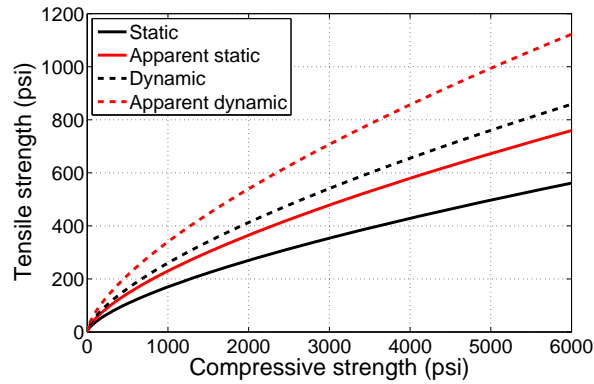


Fig. 2.6. Design chart for tensile strength adopted from Raphael (1984)

and is thus well-suited for use in heavy-duty and demanding construction projects. General characteristics of #11 rebar are summarized in table 2.3.

Table 2.3. General characteristics of rebar #11

Characteristics	Symbol	Unit	Quantity
Nominal diameter	d_N	mm	35.81
Nominal cross-sectional area	A_N	mm ²	1006
Mass per unit length	ρ_l	kg/m	7.924
Elastic modulus	E	MPa	207000
Poisson's ratio	ν	-	0.25
Yield stress	σ_Y	MPa	275

2.2.1.4 ASR model properties

In the present research, the Saouma et al. proposed model for modeling the ASR in concrete material is used. Detailed formulation of this model can be found in related papers (Saouma and Perotti 2006). The model requires some parameters to compute the strain due to AAR expansion. Table 2.4 summarizes these properties for the RC panel.

The ASR free expansion over time is characterized by a sigmoidal curve including a latency time, a characteristic time and an asymptotical deformation. Determining the values for characteristics and latency times requires the experimental test on the sample of concrete. In the absence of appropriate field information, it is still possible to use one of the experiments published already in literature which has the closed concrete mixture and test condition to the present model. Table 2.2 shows the concrete mixture for the current RC panel. Table 2.5 presents a summary of well documented concrete mixture used for ASR/AAR tests. It appears that the mix provided by Multon et al. (Multon et al. 2003, 2005, Multon and Toutlemonde 2006) has the closest similarities with the mix recommended for the fabrication of the studied wall panel.

Thus, model 2 and 3 are selected from Table 2.5. Model 2 shows the test on cylindrical specimen, while model 3 was conducted on prismatic specimen. Figure 2.7 shows the experimental test obtained by Multon et al. on these two types of specimen. Deformations were measured perpendicularly to the casting

Table 2.4. General parameters of the ASR model used in RC panel

Characteristics	Symbol	Unit	Mean	STD	min	max
Maximum volumetric strain at temperature T_0^{test}	$\varepsilon_{ASR}^{\infty}$	-	0.005	-	-	-
Characteristic time at temperature $\theta_0^{test}=273+T_0^{test}$	τ_C	ATU	37.9	3.8	-	-
Latency time at temperature $\theta_0^{test}=273+T_0^{test}$	τ_L	ATU	88.5	8.8	-	-
Activation energy associated with τ_C	U_C	$^{\circ}\text{K}$	5,400	500	4,900	5,900
Activation energy associated with τ_L	U_L	$^{\circ}\text{K}$	9,400	500	8,900	9,900
Residual reduction factor	Γ_r	-	0.5	0.1	0.3	0.7
Fraction of ε_t prior to reduction of AAR expansion due to macro cracking	γ_t	-	0.5	0.1	0.3	0.7
Compressive strength	f'_c	MPa	-31	-	-	-
Tensile strength	f'_t	MPa	3.2	-	-	-
Shape parameter	a	-	0	-	-	-
Reference temperature	T_0	$^{\circ}\text{C}$	35	-	-	-
Upper compressive stress beyond which there is no more AAR expansion	σ_U	MPa	-8	-0.8	-7.2	-8.8
Reduction fraction for Young's Modulus when AAR reaction ends	β_E	-	0.5	0.1	0.4	0.6
Reduction fraction for tensile strength when AAR reaction ends	β_f	-	0.5	0.1	0.4	0.6

direction on the prismatic specimens (Perp-Prisms) and parallel to the casting direction on the cylindrical ones (Par-Cyl). Some of the measurements were directly performed on the original casting specimens. Some other measurements were carried out on cylindrical cores (diameter: 110 mm and length: 220 mm) drilled from the prisms (Perp-Cores) and cylinders (Par-Cores) 28 days after casting. Ninety-eight days after casting, cores were also drilled from other prisms (R-Perp) and cylinders (R-Par) in order to carry out and analyze residual expansion tests.

Figure 2.7 shows a set of observations obtained from experimental tests by Multon et al. for the specimens kept at air in 100% of relative humidity and 38 $^{\circ}\text{C}$. The mean data for two measurement methods, i.e. perpendicular to casting and parallel to casting, were digitized and a curve was fitted to each one using the Larive's model. Figures 2.8 and 2.9 show the fitted curves and mean data points. Least square method was used for curve fitting. The computed values of ε^{∞} , τ_L and τ_C for the specimens with measurement in the parallel direction are 0.26%, 67 days, and 31 days, respectively. Similar values can be obtained for the measurement in the perpendicular direction, i.e., 0.137%, 65 days, and 33 days respectively.

Based on Figure 2.10 the values of the latency and characteristics times are not sensitive to the asymptotic strain. Thus, it is possible to use the value of the τ_L and τ_C obtained from Multon test for any other analysis assuming similar concrete mixture and testing conditions.

Table 2.5. Concrete mixture models used in the literature for AAR and ASR tests

Model no.	1	2	3	4	5	6	7	8	9
Coarse agg.	1050 kg/m ³	1120 kg/m ³	1120 kg/m ³	1071 kg/m ³	1067 kg/m ³	1047 kg/m ³	-	-	1078 kg/m ³
Coarse agg. Type	siliceous limestone	reactive siliceous limestone	reactive siliceous limestone	-	-	-	-	-	Fine gravel
Fine agg.	700 kg/m ³	620 kg/m ³	620 kg/m ³	776 kg/m ³	773 kg/m ³	759 kg/m ³	-	-	719 (+53.91) kg/m ³
Fine agg. Type	siliceous limestone	non-reactive sand	non-reactive sand	Sand	Sand	Sand	-	-	Sand (+Filler)
Cement	410 kg/m ³	410 kg/m ³	410 kg/m ³	475 kg/m ³	430 kg/m ³	356 kg/m ³	-	-	410 kg/m ³
Cement type	Ordinary Portland	-	-	-	-	-	-	-	Portland cement CEM I 52.5 CE PM-CP2
Water	196.8 kg/m ³	-	-	162 liter	171 liter	166 liter	-	-	196.8 kg/m ³
W/C ratio	-	-	-	0.34	0.4	0.47	-	-	0.48
Alkali (Initial)	1.13% Na ₂ O _{eq}	0.92% Na ₂ O _{eq}	0.92% Na ₂ O _{eq}	-	-	-	-	-	0.79% Na ₂ O _{eq}
Alkali (Total)	1.25% Na ₂ O _{eq} (5.125 kg/m ³)	1.25% Na ₂ O _{eq} (5.125 kg/m ³)	1.25% Na ₂ O _{eq} (5.125 kg/m ³)	-	-	-	-	-	1.25% Na ₂ O _{eq}
Speciman type	cylinders	cylinders	prisms	prisms	prisms	prisms	cylinders	cylinders	cylinders
Speciman dimension	240 mm high, 130 mm diameter	320 mm high, 160 mm diameter	140 x 140 x 280 mm	70 x 70 x 280 mm	70 x 70 x 280 mm	70 x 70 x 280 mm	160 x 320 mm	160 x 320 mm	160 x 320 mm
Cured period	-	28 days	28 days	-	-	-	-	-	-
RH-storage	different (Refer to explanations)	different (Refer to explanations)	different (Refer to explanations)	100%	100%	100%	ambient humidity	73%, 87.5%, 92.5%, 100%	38oC
Test temp.-Storage	38oC	38oC	38oC	60oC	60oC	60oC	23oC, 38oC, 60oC	38oC	38oC
Explanations	(1) immersed in water (2) in saturated humidity (100% RH) (3) in high but not saturated humidity (RH between 95 and 99%) (4) wrapped in aluminium foils (no or low water loss)	(1) 100% RH, (2) totally immersed in water, (3) under aluminum sealing at 30% RH,	(1) 100% RH, (2) totally immersed in water, (3) under aluminum sealing at 30% RH,	-	-	-	-	-	-
Authors	Larive et al.	Multon et al.	Multon et al.	Cyr and Carles-Gibergues	Cyr and Carles-Gibergues	Cyr and Carles-Gibergues	Larive	Larive	Mohamed et al.
Title	THE ROLE OF WATER IN ALKALI-SILICA REACTION	Estimation of the Residual Expansion of Concrete Affected by Alkali Silica Reaction	Estimation of the Residual Expansion of Concrete Affected by Alkali Silica Reaction	Normalized age applied to AAR occurring in concretes with or without mineral admixtures	Normalized age applied to AAR occurring in concretes with or without mineral admixtures	Normalized age applied to AAR occurring in concretes with or without mineral admixtures	PhD thesis	PhD thesis	Influence of composite materials confinement on alkali aggregate expansion
Year	2000	2008	2008	2002	2002	2002	1998	1998	2005

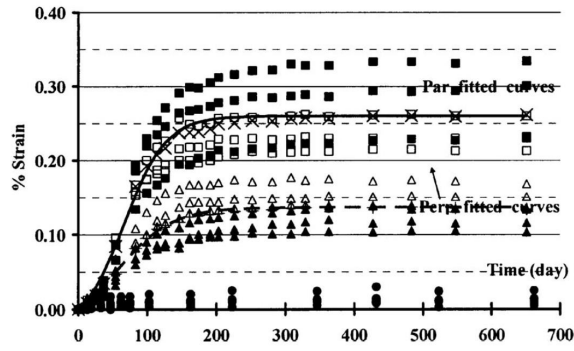


Fig. 2.7. Experimental test by Multon et al.; specimens kept in air at 100% RH and 38°C

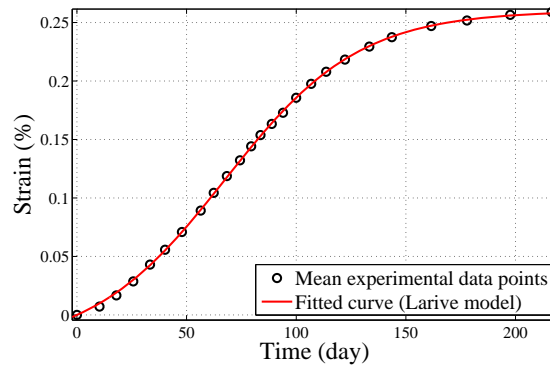


Fig. 2.8. Fitted curve to the data points based on measurement in parallel direction

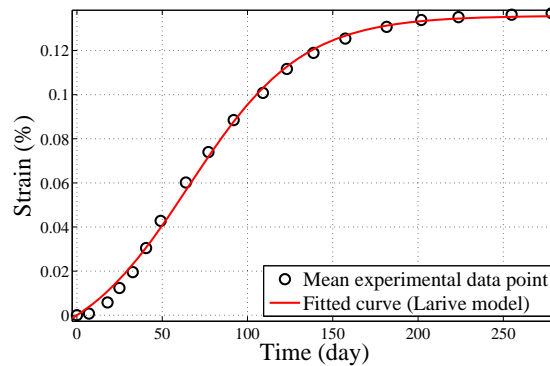


Fig. 2.9. Fitted curve to the data points based on measurement in perpendicular direction

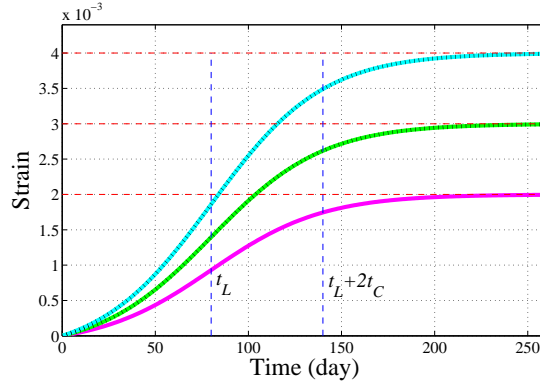


Fig. 2.10. Comparison of expansion curves with different asymptotic strains and same latency and characteristics times

2.2.2 STRUCTURAL ASSESSMENT OF THE RC PANEL

In this section the RC Panel is analyzed. No expansion is allowed in the directions perpendicular to the side walls; however, expansion in vertical direction is permitted. Table 2.6 describes the various models studied for different boundary conditions and constitutive models. The finite element model performed using Merlin Finite Element code consists of totally $N=1001$ node and $E=720$ quadrilateral elements as shown in figure 2.11. Two sets of reinforcements are modeled at the top and the bottom of the specimen. In Merlin, the rebars can be modeled easily by defining the the start and end nodes. Then, Merlin automatically applies the mesh on the rebars. The finite element mesh of the rebars for the panel is shown in figure 2.12.

Table 2.6. Different types of the models for the panel

ID	Reinf.	Loading	BC on xz plane	BC on yz plane	Material model
P1	No	ASR	$x=y=z=0$	$x=y=z=0$	Linear Elastic
P2	No	ASR	$x=y=0$	$x=y=0$	Linear Elastic
P3	Yes	ASR	$x=y=z=0$	$x=y=z=0$	Linear Elastic
P4	Yes	ASR	$x=y=0$	$x=y=0$	Linear Elastic
P5	Yes	ASR	$x=y=z=0$	$x=y=z=0$	Non-Linear
P6	Yes	ASR	$x=y=0$	$x=y=0$	Non-Linear

In all models, the panel is experienced only the ASR expansion and no external load (directly or indirectly) is applied to the panel. The models are expected to expand only in z direction. Figure 2.13 compares the un-deformed and deformed shape of the panel assuming two different boundary conditions as explained in table 2.6. Based on figure 2.13 (middle), restricting the side-walls in all three directions leads to expansion of the panel in the z direction. The maximum deformation is found at the central point of the upper and lower faces.

When the sides are free from “sliding” vertically (right figure), i.e., side-walls deformations are restricted in x and y directions (not z), uniform vertical expansion in both +z and -z direction is obtained.

Considering the symmetry of the panel, in both boundary models the panel shows the same responses along the positive and negative z axis.

In order to investigate the structural responses of the panel, two index points are selected in an attempt

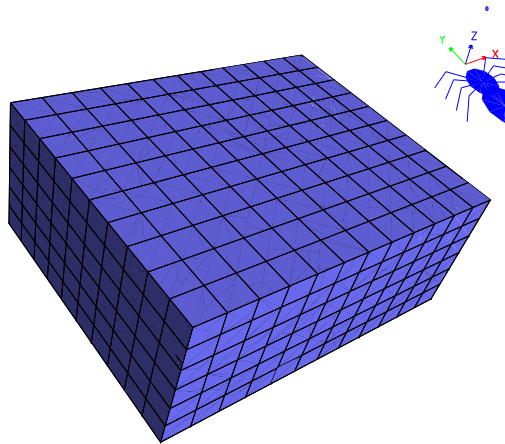


Fig. 2.11. 3D finite element model of the RC panel

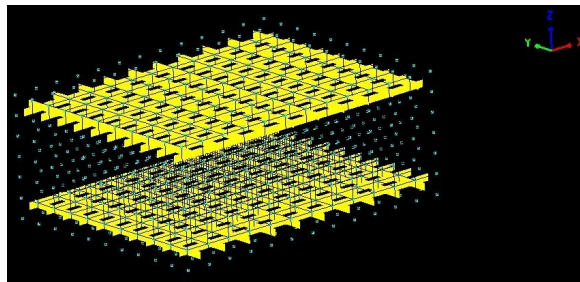


Fig. 2.12. 3D finite element model of the reinforcement for panel

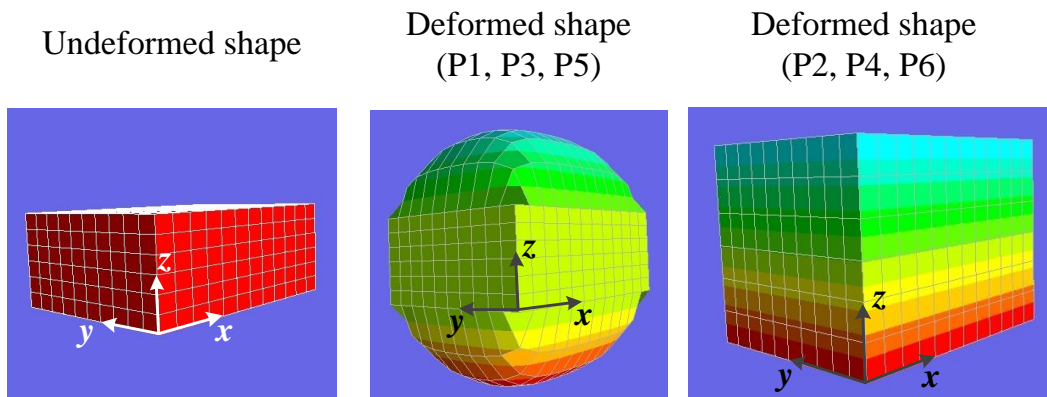


Fig. 2.13. Comparison of the deformed and un-deformed shapes of the panel

to illustrate the general behavior of the panel. Figure 2.14 shows the spatial location of the index points and

also different layers of the panel model. Index-1 is located on the middle of the top layer and Index-2 is located right in the center of the panel. Maximum ASR expansion is observed at Index-1 point.

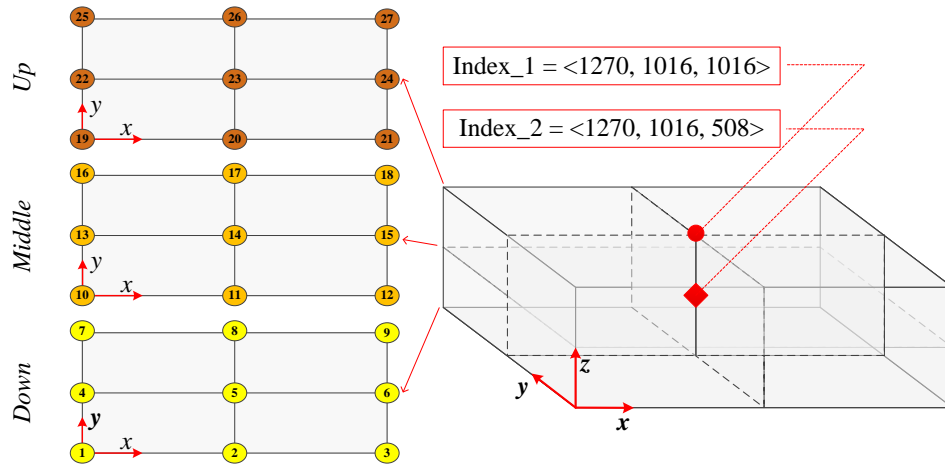


Fig. 2.14. Spatial location of index points and layers of the panel

2.2.2.1 Model P1

In this model, the side-walls are restricted in all three directions and thus no expansion is permitted near the side-walls. The panel is modeled without considering the reinforcements. The concrete is modeled as linear elastic material. Fine mesh is used in the finite element model to capture all the details.

Figure 2.15 shows the response of the considered specimen for the two index points showed in figure 2.14. The responses are only shown in vertical direction (z-direction), because we are mainly interested in out-of-plane response of the concrete block. It is noteworthy that the responses in other two directions, i.e. x- and y-directions are almost the same (considering the dimensions of the panel). Based on this figure, the maximum vertical displacement of the Index-1 is about 2.62 mm, while Index-2 has no displacement due to symmetry of the model.

Both the index points show vertical strain (ϵ_{zz}); however, the maximum vertical strain of the Index-1 is about 5 times of the Index-2. Also, it seems that the curve associated with Index-2 reaches earlier to the flat position than to the Index-1.

The vertical stress (σ_{zz}) plots for both the index points do not follows the conventional sigmoid-like curves (in spite of the displacement and strain curves). The maximum vertical stress values are very close in both the index points; however, Index-1 is a bit more. Index-2 shows a considerable initial vertical stress that can be attributed to the self-weight of the model.

Finally, comparison of the volumetric AAR strain (ϵ_{AAR}^{vol}) reveals that none of the index points reach the maximum volumetric strain (ϵ_{AAR}^{∞}), 0.005, at the end of the analysis. The curves associated with Index-1 and Index-2 have almost the same trend up to Inc = 100; however, for higher increments the Index-1 shows the higher ϵ_{AAR}^{vol} .

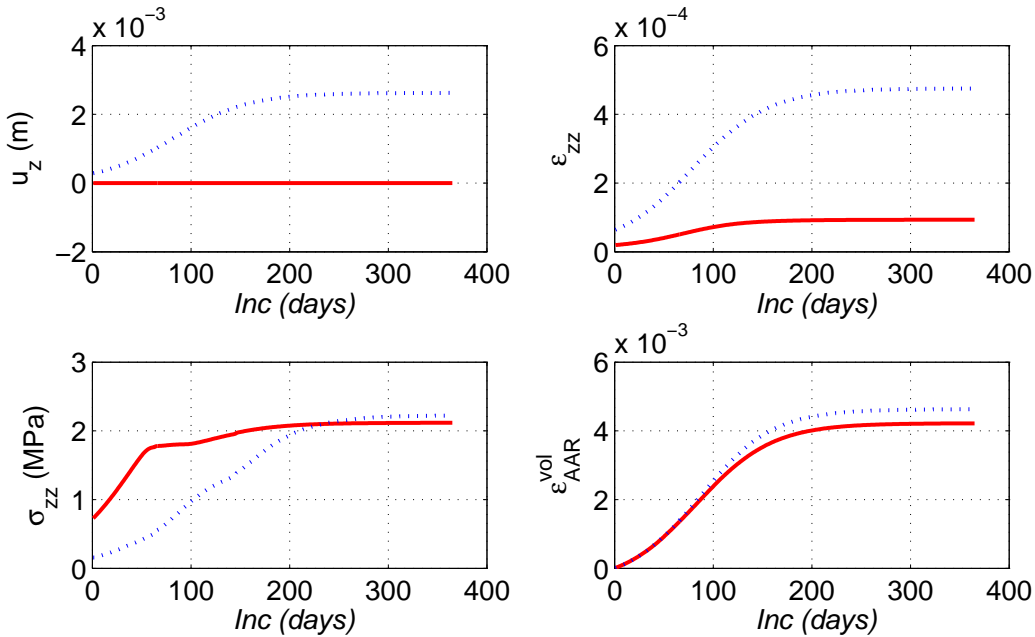


Fig. 2.15. Response of model P1 at Index-1 (blue dotted line) and Index-2 (solid red line)

2.2.2.2 Model P2

In this model, the side-walls are restricted only in two directions $x=y=0$ and the model is permitted to expand freely in z direction. The panel is modeled without considering the reinforcements. The concrete is modeled as linear elastic material.

Figure 2.16 shows the response of the considered specimen for the two index points showed in figure 2.14. Based on this figure, the maximum vertical displacement of the Index-1 is about 2.73 mm, while Index-2 has no displacement due to symmetry of the model. Compared to the model P1, having a free boundary condition in z direction increases the vertical displacement at the middle of the panel (most critical location).

In this model, both the index points have exactly the same vertical strain (ϵ_{zz}). The maximum ϵ_{zz} at the end of analysis reaches to about 0.0053 in the both index points. Comparing to the model P1, this model, P2, shows the higher strain values. Also, ϵ_{zz} has a uniform distribution along the thickness of the panel.

The vertical stress (σ_{zz}) plots for both the index points have a similar trend. The plots do not follow a specific form. the values of the σ_{zz} is negative for all increments which means that the panel is under compressive stresses. It should be noted that the value of the compressive stress is very negligible. The maximum absolute value of the vertical stresses reaches to about 0.05 MPa. Therefore, it is possible to assume that the panel is stress-free in vertical direction under ASR loading. This conclusion is in agreement with the assumed boundary condition for model P2.

Finally, comparison of the volumetric AAR strain (ϵ_{AAR}^{vol}) reveals that none of the index points reach the maximum volumetric strain (ϵ_{AAR}^{∞}), 0.005, at the end of the analysis. Both the index points have the same expansion. It means that the panel has a uniform volumetric AAR strain along its thickness.

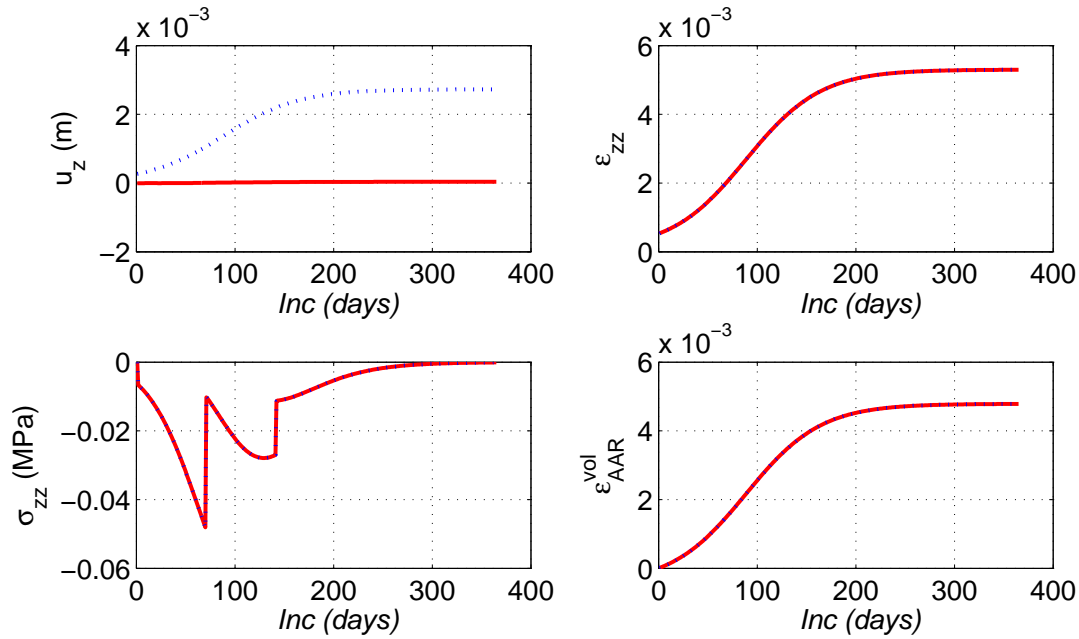


Fig. 2.16. Response of model P2 at Index-1 (blue dotted line) and Index-2 (solid red line)

2.2.2.3 Model P3

In this model, the side-walls are restricted in all three directions and thus there will be no expansion in the side-walls. The panel is modeled considering the reinforcements as shown in figure 2.12. The concrete is modeled as linear elastic material.

Figure 2.17 shows the response of the considered specimen for the two index points showed in figure 2.14. The responses are only shown in vertical direction (z -direction). Based on this figure, the maximum vertical displacement of the Index-1 is about 2.61 mm, while Index-2 has no displacement due to symmetry of the model. The u_{zmax} for this model, P3, is just a bit smaller than model P1 (the same model as P3 but without reinforcement).

Both the index points show vertical strain (ϵ_{zz}); however, the maximum vertical strain of the Index-1 is about 5 times of the Index-2. Also, it seems that the curve associated with Index-2 reaches earlier to the flat position than to the Index-1.

The vertical stress (σ_{zz}) plots for both the index points do not follow the conventional sigmoid-like curves (in spite of the displacement and strain curves). The maximum vertical stress values are close in both the index points; however, Index-1 is a bit more. Index-2 shows a considerable initial vertical stress that can be attributed to the self-weight of the model. Compared to the model P1, this model, P3, shows higher maximum vertical stress at the Index-1; however, it shows less stress at point Index-2.

Finally, comparison of the volumetric AAR strain (ϵ_{AAR}^{vol}) reveals that none of the index points reach the maximum volumetric strain (ϵ_{AAR}^{∞}), 0.005, at the end of the analysis. The curves associated with Index-1 and Index-2 have almost the same trend up to $Inc = 100$; however, for higher increments the Index-1 shows the higher ϵ_{AAR}^{vol} . Comparing to model P1, this model, P3, just has a bit smaller final strain value.

Figure 2.18 shows the non-concurrent maximum and minimum stresses experienced by rebars for all increments. As seen, at the first increment some of the rebars are under tension (mainly due to weight of

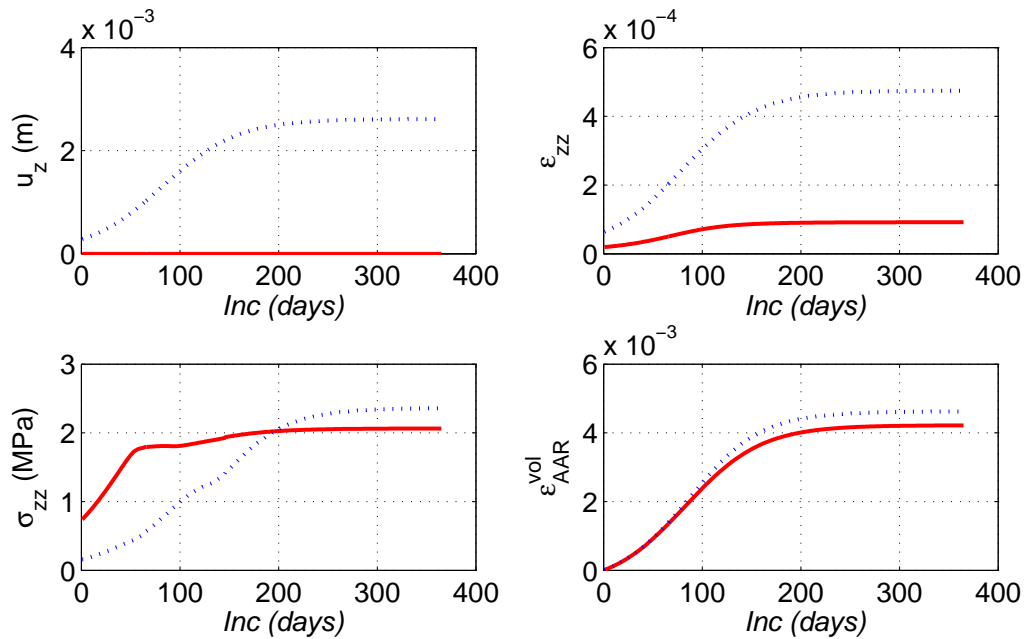


Fig. 2.17. Response of model P3 at Index-1 (blue dotted line) and Index-2 (solid red line)

concrete and steel) and some other are under compression. As seen, the maximum stress starts at about 7 MPa and increases to about 125 MPa. On the other hand, the minimum stress starts at about -9 MPa and increase up to -6 MPa, then decrease again to about -48 MPa at the end of analysis. It is noteworthy that based on table 2.3 the yield stress at the rebars is 275 MPa. Thus the rebars are not failed in this case. It is important to note that the linear elastic characteristics of the concrete is one of the main reasons that the rebars remain safe. In the case of nonlinear concrete material with the ability of cracking (based on smeared crack model, as it will be discussed later) the load carrying capacity of the whole RC panel is controlled by rebars after concrete cracking. This may leads to failure of the rebars.

Figure 2.19 shows stresses in the two most critical rebars in x and y directions. Based on figure 2.12 the longer rebar in x direction is divided into 12 segments (elements), while the shorter rebar in y direction is divided into 10 segments.

Based on figure 2.19, the most critical rebar belongs to the x direction (because it is longer). The maximum and minimum stresses in this case are in agreement with those already obtained in figure 2.18 for whole the panel.

According to figure 2.19, the maximum stresses (in the form of tensile stress) are occurred near the two ends of the rebar. Also, the minimum stresses (in the form of compressive stress) are occurred in middle of the rebar. Based on this figure increasing the number of increments (expansion of the panel), leads to increasing the stresses in vicinity of the ends; however, it has almost negligible effect in middle of the rebar.

2.2.2.4 Model P4

In this model, the side-walls are restricted only in two directions $x=y=0$ and the model is permitted to expand freely in z direction. The panel is modeled considering the reinforcements as shown in figure 2.12. The concrete is modeled as linear elastic material.

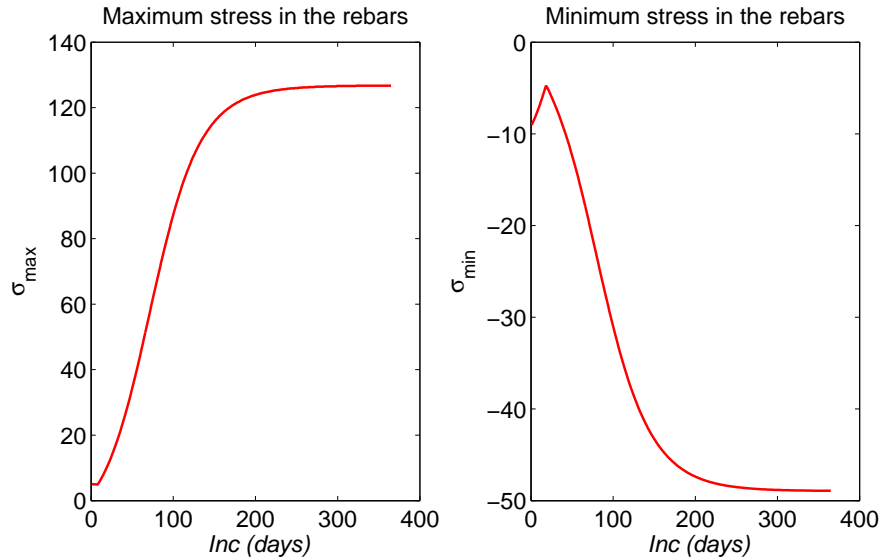


Fig. 2.18. Non-concurrent maximum and minimum stresses in rebars for model P3

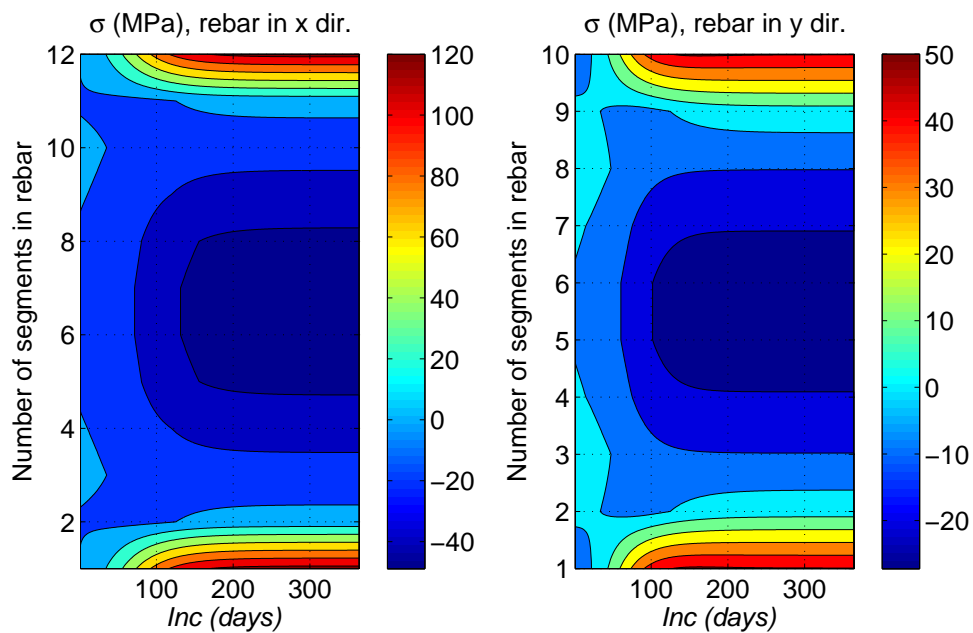


Fig. 2.19. Stress at the most critical rebars in x and y directions for model P3

Figure 2.20 shows the response of the considered specimen for the two index points showed in figure 2.14. Based on this figure, the maximum vertical displacement of the Index-1 is about 2.96 mm, while the Index-2 shows a maximum displacement about 0.27 mm. Compared to the model P2, modeling the reinforcement increases the vertical displacement in both the index points. It is noteworthy that none of the P1, P2, and P3 models had the vertical displacement at the Index-2; however, model P4 shows some responses in this point.

In this model, both the index points have exactly the same vertical strain (ϵ_{zz}). The maximum ϵ_{zz} at the end of analysis reaches to about 0.0053 in the both index points. Comparing to the model P2, this model, P4, shows exactly the same response.

The vertical stress (σ_{zz}) plots for both the index points have a similar trend. The plots do not follow a specific form. The values of the σ_{zz} is negative for all increments which means that the panel is under negligible compressive stresses. The maximum absolute value of the vertical stresses reaches to about 0.05 MPa. Therefore, it is possible to assume that the panel is stress-free in vertical direction under ASR loading. This behavior is in agreement with the model P2.

Finally, comparison of the volumetric AAR strain (ϵ_{AAR}^{vol}) reveals that none of the index points reach the maximum volumetric strain (ϵ_{AAR}^{∞}), 0.005, at the end of the analysis. Both the index points have the same expansion. It means that the panel has a uniform volumetric AAR strain along its thickness.

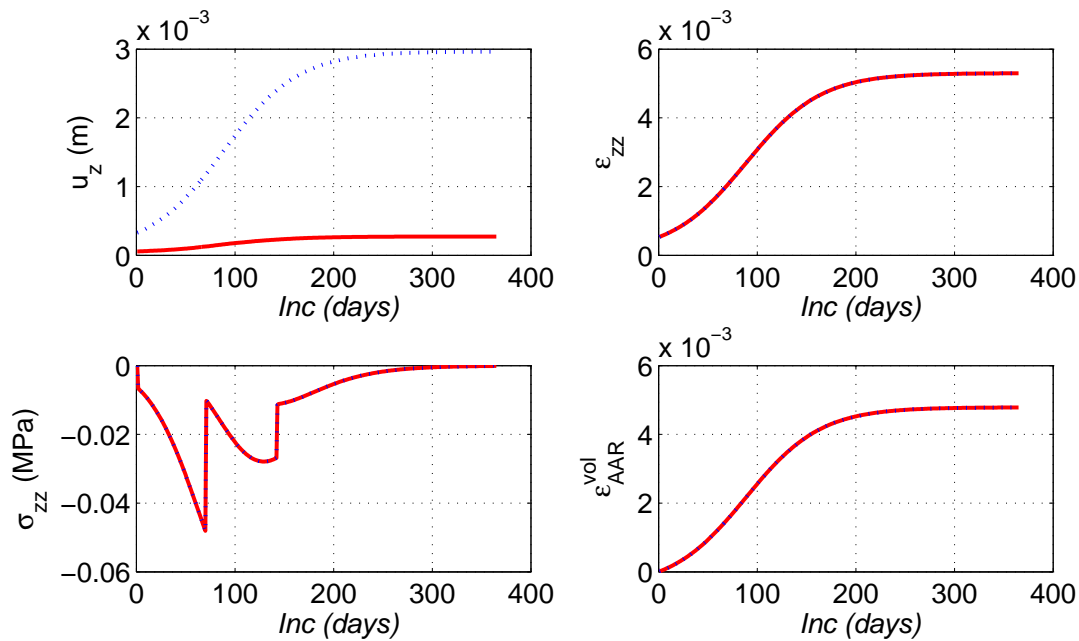


Fig. 2.20. Response of model P4 at Index-1 (blue dotted line) and Index-2 (solid red line)

Figure 2.21 shows the non-concurrent maximum and minimum stresses experienced by rebars for all increments of model P4. Although there is fluctuation in stress response of the rebars, all the values are very small and negligible. This model proves that the rebars have no effect when the panel is modeled based on free boundary condition in vertical (z) direction.

2.2.2.5 Summary and Observations

Table 2.7 summarizes the maximum and minimum responses obtained from figures 2.15, 2.16, 2.17 and 2.20. Following are some of the highlighted points when comparing different models:

- Maximum expansion for the models with fixed walls in vertical (z) direction (models P1 and P3) is occurred at the point Index-1.

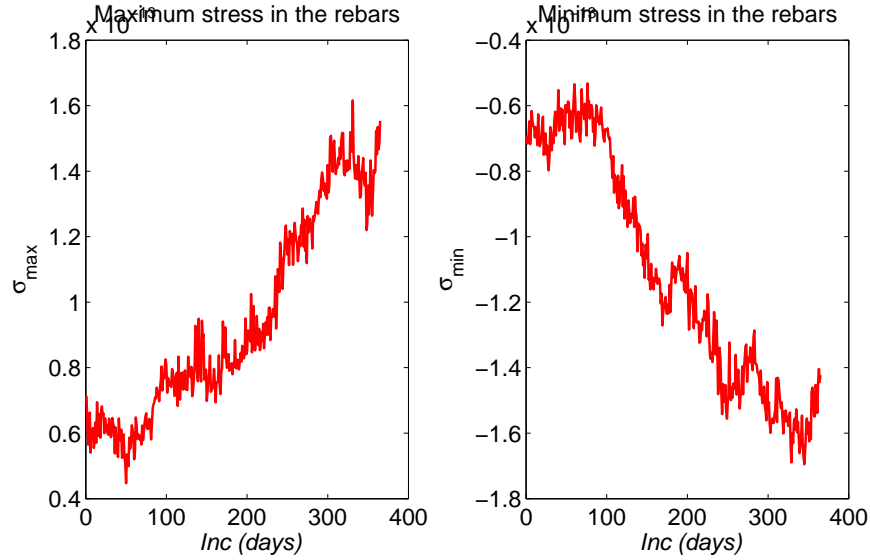


Fig. 2.21. Non-concurrent maximum and minimum stresses in rebars for model P4

Table 2.7. Comparison of the panel models based on linear elastic material

Model	Location	u_{zmax} (mm)	ϵ_{zz}	$ \sigma_{zzmax} $ (MPa)	ϵ_{AAR}^{vol}
P1	Index-1	2.623	4.75e-4	2.223	4.63e-3
	Index-2	0	9.32e-5	2.117	4.22e-3
P2	Index-1	2.727	5.29e-3	0.048	4.78e-3
	Index-2	0	5.29e-3	0.048	4.78e-3
P3	Index-1	2.613	4.75e-4	2.359	4.62e-3
	Index-2	0	9.18e-5	2.063	4.22e-3
P4	Index-1	2.964	5.29e-3	0.048	4.78e-3
	Index-2	0.273	5.29e-3	0.048	4.78e-3

- For the models with free walls in vertical direction (models P2 and P4) the expansion is uniform in thickness.
- In none of the models, the maximum ASR-induced volumetric strain reaches to the limit value, 0.005.
- The stress profile of the models P1 (or P3) and model P2 (or P4) has substantial differences. In the former one, the stress increases as the strain increase. However, in the later one, there is almost no stresses in the index points (there is some negligible compressive stresses).
- Based on model P3, the maximum tensile stress in the rebars never reaches to the yield stress of the steel. This is mainly due to contribution of the concrete even in higher swellings. Modeling the concrete with smeared crack approach can be provided a realistic vision about the stresses in rebars at higher expansions.

2.3 CASE STUDY II: BENDING BEAM

The second case study is a three-point bending beam. The beam is subjected to both ASR expansion and vertical applied displacement. Figure 2.22 shows the dimensions of the beam and the boundary conditions. Figures 2.23 and 2.24 show the type and location of the longitudinal and transverse reinforcements in the beam. It is noteworthy that the information about the longitudinal reinforcements are provided to the authors, and the transverse reinforcements are computed based on the minimum required reinforcements recommended by ACI code. Distance between the transverse reinforcements, s , are computed based on:

$$s = \begin{cases} \frac{A_v f_y}{50b} \\ s < 24'' \\ s < d/2 \end{cases} \quad (2.7)$$

where A_v is the cross-section of each stirrup, f_y is the yield stress, and b and d are the width and the depth of the beam, respectively. Rebars # 11 are used as longitudinal reinforcements, while rebars # 4 are used as transverse reinforcements.

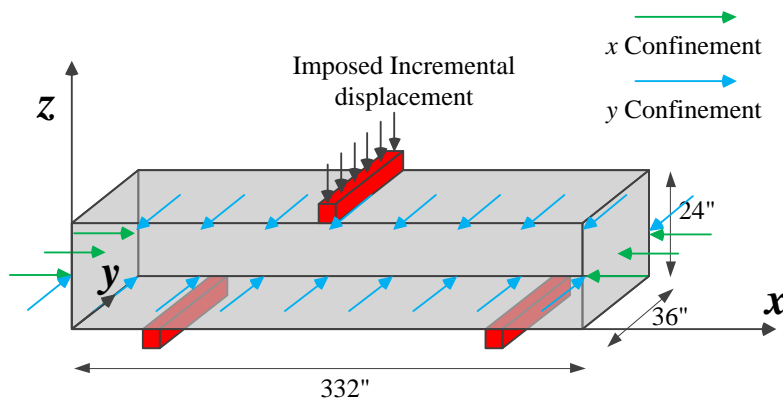


Fig. 2.22. General view, dimensions and boundary condition of the three-point bending beam

2.3.1 MATERIAL PROPERTIES

This section explains the material properties which are used for assessment of three-point bending beam. Material properties can be divided into the following major groups:

- Concrete properties
- Longitudinal rebar properties
- Transverse rebar properties
- ASR model properties

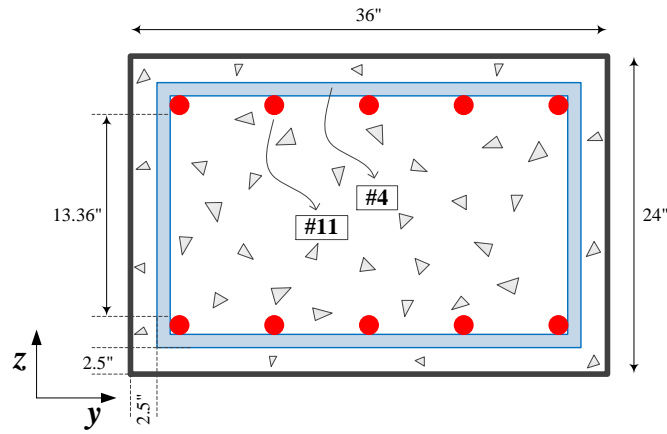


Fig. 2.23. Reinforcements in the beam, y-z plan view

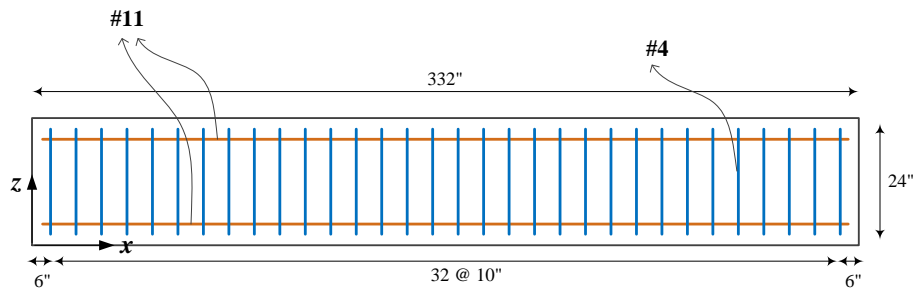


Fig. 2.24. Reinforcements in the beam, x-z plan view

2.3.1.1 Concrete properties

General characteristics of the concrete are summarized in table 2.8.

Table 2.8. General characteristics of concrete for beam

Characteristics	Symbol	Unit	Mean	STD	min	max
Mass density	ρ	kg/m ³	2,250	225	1,800	2,700
Compressive strength	f'_c	MPa	-31	3.1	24.82	37.24
Tensile strength	f'_t	MPa	3.2	0.32	2.56	3.84
Elastic modulus	E	MPa	26,000	2,600	20,800	31,200
Poisson's ratio	ν	-	0.2	0.02	0.16	0.24

2.3.1.2 Steel properties

Rebar #11 is used as longitudinal reinforcement. General characteristics of this rebar are summarized already in table 2.3. On the other hand, rebar #4 is used as transverse reinforcement. General characteristics of this rebar are summarized in table 2.9.

Table 2.9. General characteristics of rebar #4

Characteristics	Symbol	Unit	Mean
Nominal diameter	d_N	mm	12.70
Nominal cross-sectional area	A_N	mm ²	109
Mass per unit length	ρ_l	kg/m	0.996
Elastic modulus	E	MPa	207000
Poisson's ratio	ν	-	0.25
Yield stress	σ_Y	MPa	275

2.3.1.3 ASR model properties

Table 2.10 summarizes the properties used for calculation of the ASR expansion in the beam.

Table 2.10. General parameters of the ASR model for beam

Characteristics	Symbol	Unit	Mean	STD	min	max
Maximum volumetric strain at temperature T_0^{test}	$\varepsilon_{ASR}^{\infty}$	-	0.005	-	-	-
Characteristic time at temperature $\theta_0^{test}=273+T_0^{test}$	τ_C	ATU	37.9	3.8	-	-
Latency time at temperature $\theta_0^{test}=273+T_0^{test}$	τ_L	ATU	88.5	8.8	-	-
Activation energy associated with τ_C	U_C	°K	5,400	500	4,900	5,900
Activation energy associated with τ_L	U_L	°K	9,400	500	8,900	9,900
Residual reduction factor	Γ_r	-	0.5	0.1	0.3	0.7
Fraction of ε_t prior to reduction of AAR expansion due to macro cracking	γ_t	-	0.5	0.1	0.3	0.7
Compressive strength	f'_c	MPa	-31	-	-	-
Tensile strength	f'_t	MPa	3.2	-	-	-
Shape parameter	a	-	0	-	-	-
Reference temperature	T_0	°C	35	-	-	-
Upper compressive stress beyond which there is no more AAR expansion	σ_U	MPa	-8	-0.8	-7.2	-8.8
Reduction fraction for Young's Modulus when AAR reaction ends	β_E	-	0.7	0.1	0.6	0.8
Reduction fraction for tensile strength when AAR reaction ends	β_f	-	0.7	0.1	0.6	0.8

2.3.2 ASSESSMENT OF BEAM

In this section the three-point bending beam is analyzed. Table 2.11 describes all the models and their characteristics used for analysis of beam. In the conducted analyses, the side walls of the beam can be modeled either free or restricted. Linear or nonlinear (based on smeared crack model) material can be considered for the concrete.

Table 2.11. Different types of the models for the beam

ID	Reinf.	Loading	BC on xz plane	BC on yz plane	Material model
B1	Yes	Displ	-	-	Linear (original prop.)
B2	Yes	ASR+Displ	y=0	x=0	Linear (original prop.)
B3	Yes	ASR+Displ	Free	Free	Linear (original prop.)
B4	Yes	Displ	-	-	Nonlinear (original prop.)
B5	Yes	Displ	-	-	Nonlinear (reduced prop.)
B6	Yes	ASR+Displ	y=0	x=0	Nonlinear (degradation)
B7	Yes	ASR+Displ	Free	Free	Nonlinear (degradation)

In the case of 'ASR + Displ' loading, first the beam is subjected to ASR expansion and, subsequently, the incremental displacement is applied on top of the beam. In the nonlinear models, the analysis is terminated at the load step in which the beam is cracked. However, in the linear models, there is no internal criteria and the responses should be controlled externally by comparing the computed stresses and the material strength.

Figure 2.25 shows the different steps toward the assessment of the beam affected by ASR expansion. (1) The specimen is concreting, (2) It is kept under the specific condition and the ASR phenomenon is let to develop, (3) The beam is rested on the ground (or a stiff material) by the end of ASR expansion. In this condition, the numerical model of the beam has uniform restraint in vertical direction, (4) The deformed shape of the beam is monitored at the end of expansion, (5) The shear capacity of the ASR-affected beam is tested, (6) The shear deformation of the beam is measured.

Figures 2.26 and 2.27 show the finite element model of the beam and reinforcement. Fine mesh is used in the finite element model to capture all the details. The model consists of totally $N=2065$ nodes and $E=1392$ quadrilateral elements. However, in order to modeling the stress response of the beam as accurate as possible, the half of it is modeled. Finer mesh is used also. In addition, in order to prevent the stress concentration at the support point, a rectangular elastic beam with higher elastic modulus than the main beam (at least 5 times higher) is modeled. Figure 2.28 shows the finite element model of the half-beam and the support.

In order to investigate the structural responses of the beam, three index points are chosen. Figure 2.29 shows the spatial location of these three points. They are located in the top, middle and bottom of the beam on the vertical plane at mid-span of the beam. Also this figure shows the location of two index rebars which are located at the top and bottom of the beam.

2.3.2.1 Model B1

In this model only the incremental displacement is applied to the beam. ASR effect is not considered. This is a benchmark model for further comparisons.

Before further proceedings, first the accuracy of the finite element mesh is checked. The vertical displacement response of the beam at the mid-span (maximum displacement) is selected as the demand

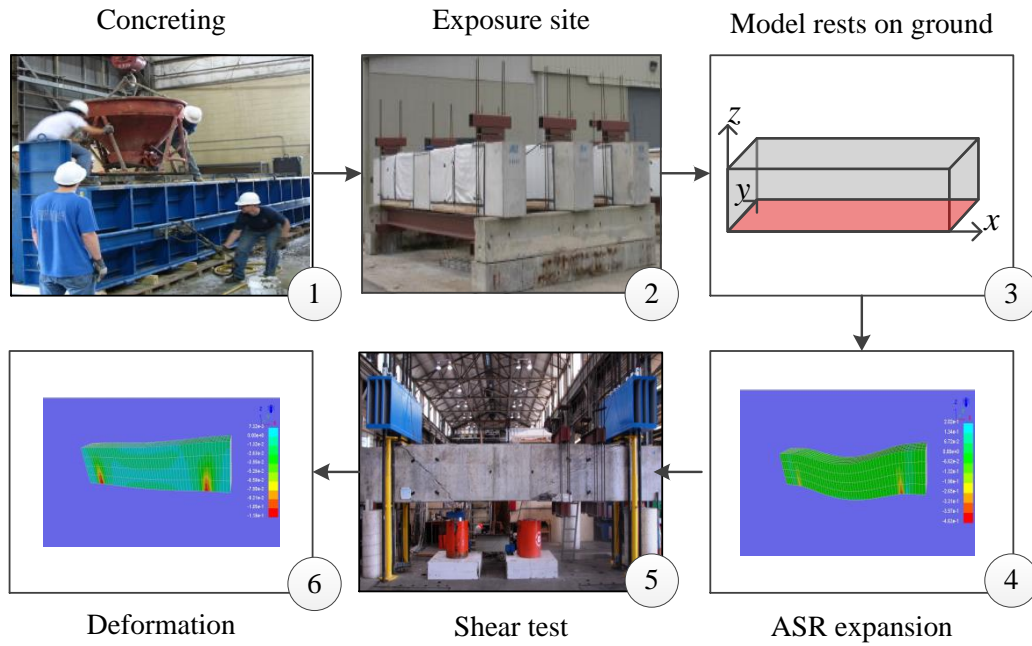


Fig. 2.25. Different steps towards shear test on ASR-affected beam

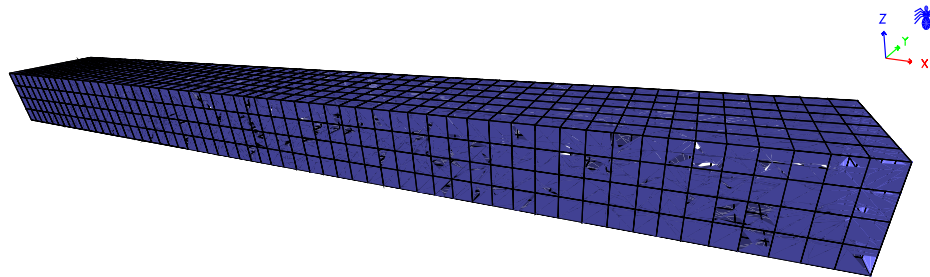


Fig. 2.26. 3D finite element model of the beam

parameter. Consequently, the finite element solution is compared by the approximate analytical solution.

Figure 2.30 shows the decomposition of the actual beam to two simplified models. In both simplified models, the maximum deflection occurs at the mid-span. It is easy to derive the deflection at the beam mid-span based on the double integration method.

For the beam under uniform load:

$$\Delta_{max}^1 = \frac{wL^2}{384EI} [24a^2 - 5L^2] \quad (2.8)$$

For the beam under concentrated load:

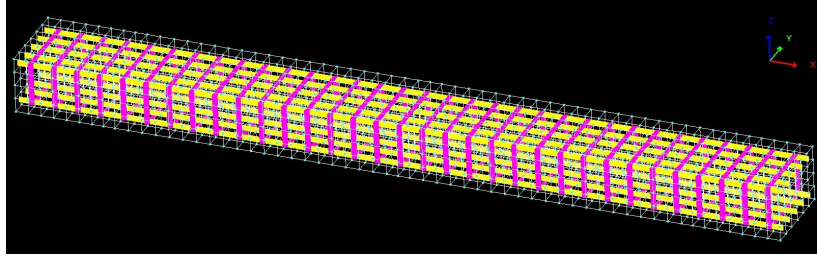


Fig. 2.27. 3D finite element model of the rebars in beam

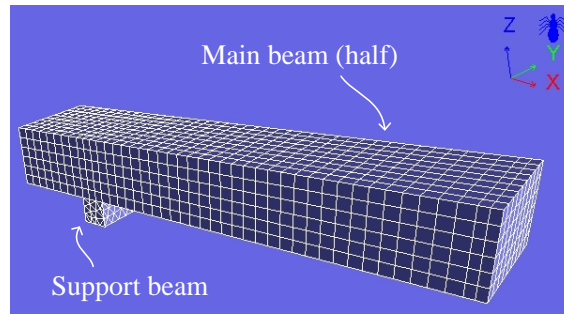


Fig. 2.28. 3D finite element model of the half beam with extra support beam

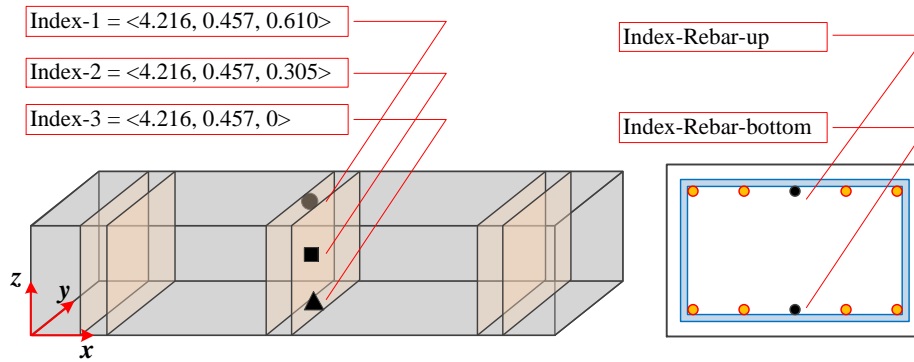


Fig. 2.29. Spatial location of index points and index rebars in the beam model

$$\Delta_{max}^2 = \frac{PL^3}{48EI} \quad (2.9)$$

All the material properties are provided already in tables 2.8 and 2.3. However, it should be noted that the area moment of inertia (I) of the RC beam deserve special attention. Considering the un-cracked cross-section for beam, the I parameter can be computed by converting the steel to the equivalent concrete.

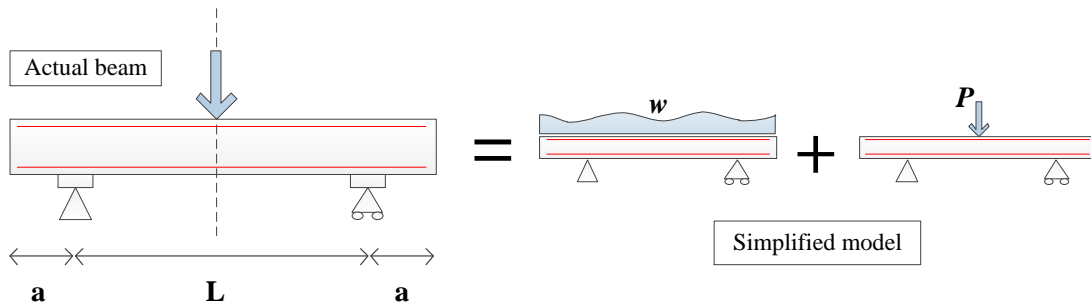


Fig. 2.30. Simplified analytical solution for beam

For this case, the modular ratio $n = \frac{E_s}{E_c}$ is about 8. Consequently, the equivalent moment of inertia (I_{eq}) is about 0.01959 m^3 .

Two load combinations are taken into account as:

1. Only the beam self-weight is considered. The point load is neglected. Based on analytical solution, $\Delta_{max}^1 = -5.03e - 4 \text{ m}$.
2. Only the unit point load (1 KN) is applied to the beam and the effect of self-weight is neglected. Based on analytical solution, $\Delta_{max}^2 = -0.01125 \text{ m}$.

Figure 2.31 shows the deformed shape, displacement contour in vertical direction for both cases. As seen, the extreme displacement in negative z-direction has very good consistency with those obtained from approximate analytical solution. It should be noted that the beam has some deformations that the analytical solution is not capable of capture them.

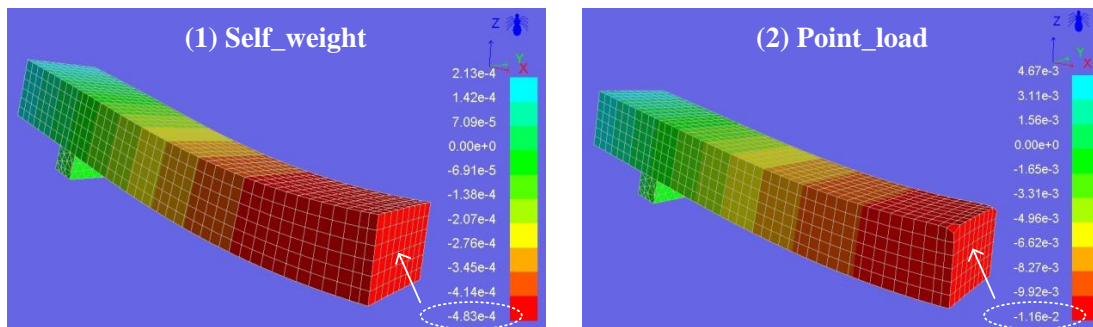


Fig. 2.31. Finite element response of the beam B1 for two load combinations

Figure 2.32 shows the response of the considered beam at three index points showed in figure 2.29. The responses are only shown in vertical direction (z-direction). As seen, the vertical displacement (u_z) varies linearly for three index points because of linear assumption model for the material. There is no differences among all three index points.

The ϵ_{zz} shows decreasing trend in the bottom and middle points (Index-3 and Index-2); however, it shows an increasing trend for the top point (Index-1).

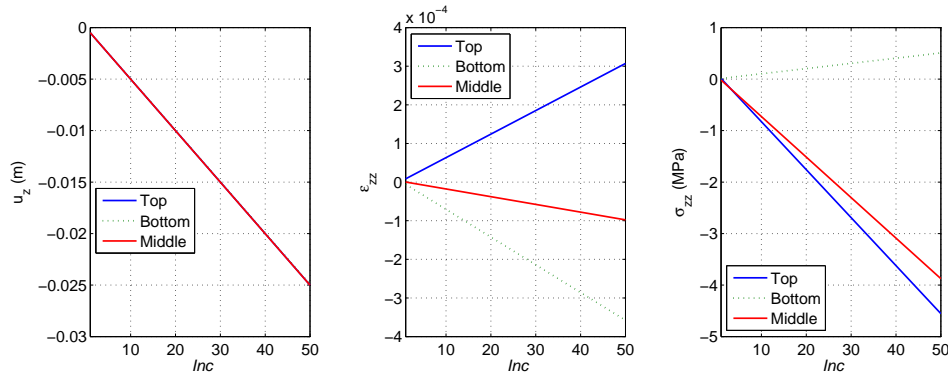


Fig. 2.32. Response of the beam B1 at three index points; Incremental displacement

Figure 2.33 shows the stresses at the two index rebars (as marked in figure 2.29) under the incremental displacement. Based on this figure applying the incremental displacement increases the tensile stresses in the bottom rebar (specially near the mid-span). Also, it increases the compressive stresses for the top rebar. The tensile stress reaches to 275 MPa, steel yield strength, at the increment $Inc = 49$ in the bottom rebar. This increment corresponds to the applied vertical displacement of 0.0245 m. This figure clearly shows that the beam first fails at the bottom rebar. The failure mode of the beam under nonlinear material will be studied later.

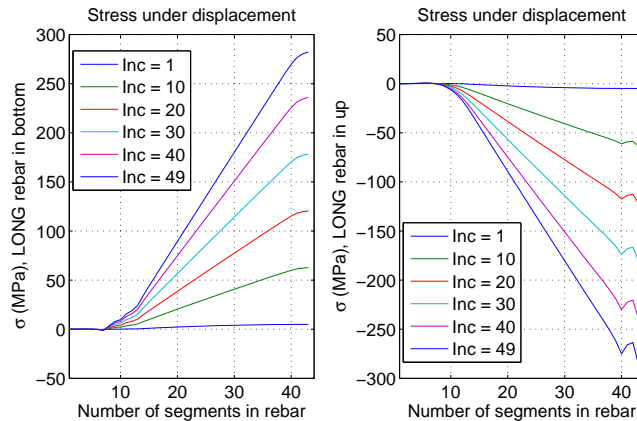


Fig. 2.33. Stress at the two index longitudinal rebars for half-beam B1; Under incremental displacement

2.3.2.2 Model B2

In this model, the side-walls are restricted in the direction perpendicular to the face. Thus, there will be no expansion in these directions. The beam is modeled considering the reinforcements effects. The concrete is modeled as a continuum linear elastic material.

Figures 2.34 and 2.35 shows the response of the considered beam at three index points showed in figure 2.29 under the ASR expansion and subsequently the incremental displacement. The responses are only shown in vertical direction (z-direction). Based on this figure, the maximum vertical displacement of the Index-1 is more than Index-2. The Index-3 point has no vertical displacement at the end of ASR expansion, as the beam is rested on the ground at this point.

Figure 2.35 only shows the response of the ASR-affected beam under the incremental displacement. As seen, the vertical displacement (u_z) varies linearly for three index points because of linear assumption model for material. Compared to figure 2.32, it can be seen that the different points along the thickness of the beam does not have a same displacement profile. This can clearly attributed to the ASR effects.

All the index points show almost the similar vertical strain (ϵ_{zz}) under the ASR expansion (Figure 2.34); however, there is a discontinuity in the time history of the strain curve when the loading type changes from ASR expansion to incremental displacement (Figure 2.35). The ϵ_{zz} shows decreasing trend in the bottom and middle points (Index-3 and Index-2); however, it shows an increasing trend for the top point (Index-1).

The vertical stress (σ_{zz}) plots for the three index points show negative values (meaning the index points are under compression) up to the end of ASR expansion. The final value of the vertical compressive stress for Index-3 is more than Index-2 and both more than Index-1. The value of the vertical stress at the location of the Index-1 is almost zero (it is on free face). Applying the incremental displacement decreases the vertical stress at the top and middle index points; however, it leads to a bit increasing at the bottom index point.

Finally, the volumetric AAR strain (ϵ_{AAR}^{vol}) reveals that none of the index points reach the maximum volumetric strain (ϵ_{AAR}^{∞}), 0.005, at the end of the analysis. The maximum expansion is about 0.00477 in all cases. The beam shows similar expansion curve in all index points.

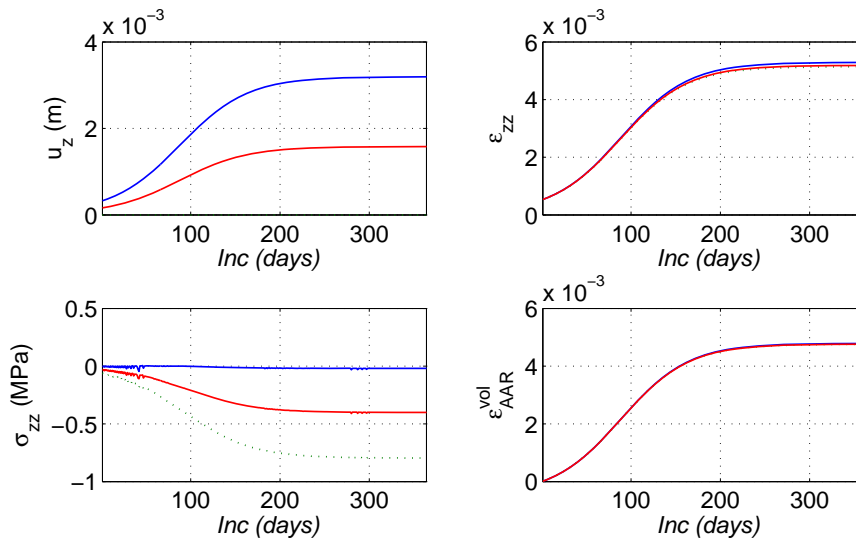


Fig. 2.34. Response of the beam B2 at three index points; Under ASR expansion

Figures 2.36 and 2.37 show the stresses at the two index rebars under the ASR expansion and incremental displacement, respectively. The plot of rebar stress are only shown for selected increments (for ASR expansion Inc = 1:50:365 and for incremental displacement Inc = 366:10:415).

Based on figure 2.36 ASR expansion increases the stresses. The half-beam experiences tensile stresses in the area far from end point and mid-span. However, it has compressive stresses near the left-end and also

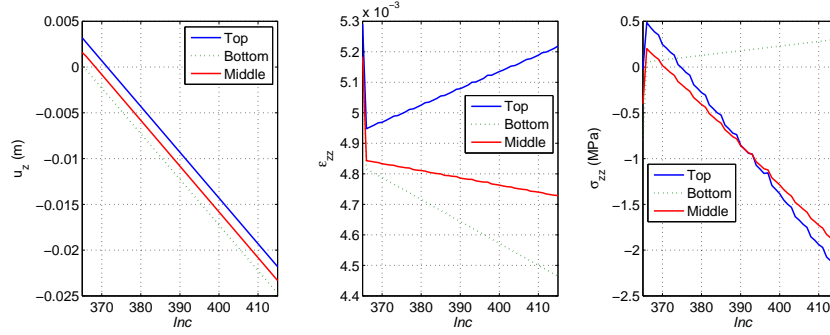


Fig. 2.35. Response of ASR-affected beam B2 at three index points; Under incremental displacement

mid-span. This rule is valid more or less for the both index rebars at the top and bottom. However, the bottom rebar experiences a bit higher stresses than the top one. It is noteworthy that the value of the stresses under ASR expansion, [-5.5, +1.5] MPa, are negligible compared to the yield strength of the steel, +275 MPa.

Based on figure 2.37 applying the incremental displacement increases the tensile stresses in middle section of the bottom rebar (between the support points). However, it increases the compressive stresses for the top rebar. The tensile stress reaches to +275 MPa, steel yield strength, at the increment $Inc = 400$ in the bottom rebar. This increment corresponds to vertical displacement of 0.0175 m. This figure clearly shows that the beam first fails at the bottom rebar. The failure mode of the beam under nonlinear material will be studied later. Compared to the figure 2.33, it can be concluded that the ASR expansion reduce the capacity of the beam and the bottom rebars fail under the smaller shear load.

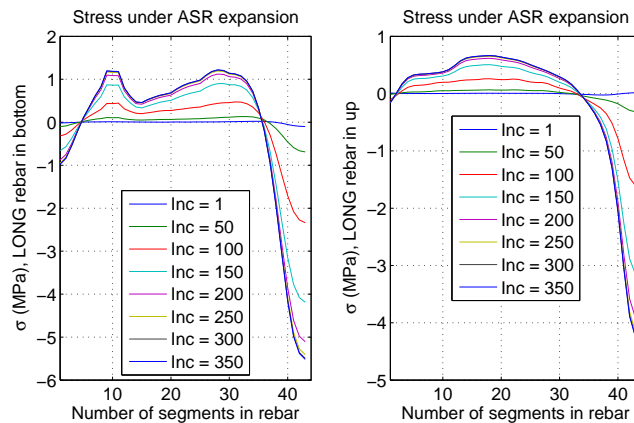


Fig. 2.36. Stress at the two index longitudinal rebars for beam B2; Under ASR expansion

Last but not least, the beam has almost uniform deformed shape under ASR expansion. The beam is expanded in vertical (z) direction considering that the other two directions are fixed. Figure 2.38 shows the deformed shape of the beam at the end of the ASR expansion. This figure also shows a close look of the top face of the beam at the end of the expansion. As seen, there are some small non-uniformity in deformation along the x -axis of the beam. Also, the top face shows higher deformation in middle than to the edges.

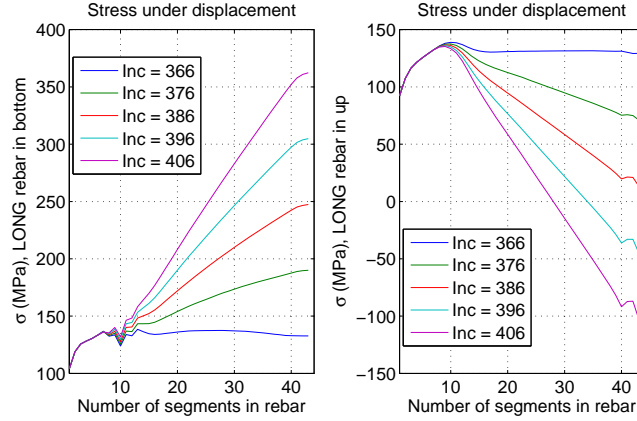


Fig. 2.37. Stress at the two index longitudinal rebars for beam B2; Under incremental displacement

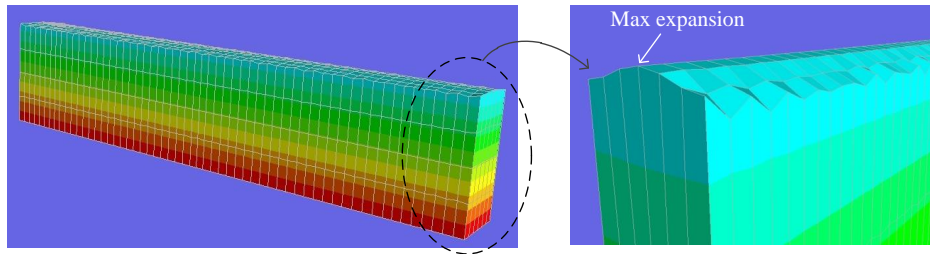


Fig. 2.38. Deformed shape of the beam at the end of ASR expansion, model B2

2.3.2.3 Model B3

In this model, all the side-walls (x - z plane and y - z plane) are free (see table 2.11). Thus, the expansion is allowed in perpendicular direction on these planes. The beam is modeled considering the reinforcements effects. The concrete is modeled as a continuum linear elastic material.

Figures 2.39 and 2.40 shows the response of the considered beam at three index points showed in figure 2.29 under the ASR expansion and subsequently the incremental displacement. The responses are only shown in vertical direction (z -direction). Based on this figure, the maximum vertical displacement of the Index-1 is more than Index-2. The Index-3 point has no vertical displacement at the end of ASR expansion, as the beam is rested on the ground at this point. Compared to beam Model B2, the beam model B3 has less vertical displacement (about 50% lower) in both Index-1 and Index-2 points.

Figure 2.40 only shows the response of the ASR-affected beam under the incremental displacement. As seen, the vertical displacement (u_z) varies linearly for three index points because of linear assumption model for material. Compared to figure 2.32, it can be seen that the different points along the thickness of the beam does not have a same displacement profile. This can clearly attributed to the ASR effects.

All the index points show almost the similar vertical strain (ϵ_{zz}) under the ASR expansion (Figure 2.39); however, the value of the final ϵ_{zz} in beam Model B3 is half of the Beam Model B2.

The vertical stress (σ_{zz}) plots for the index points Index-2 and Index-3 show negative values (meaning

the index points are under compression) up to the end of ASR expansion. However, the Index-1 shows a bit tension at the end of ASR expansion. Compared to beam Model B2, the beam Model B3 shows about 70% reduction in σ_{zz} for Index-3.

Finally, the volumetric AAR strain (ϵ_{AAR}^{vol}) reveals that none of the index points reach the maximum volumetric strain (ϵ_{AAR}^{∞}), 0.005, at the end of the analysis. The maximum expansion is about 0.0048 in all cases. The beam shows similar expansion curve in all index points.

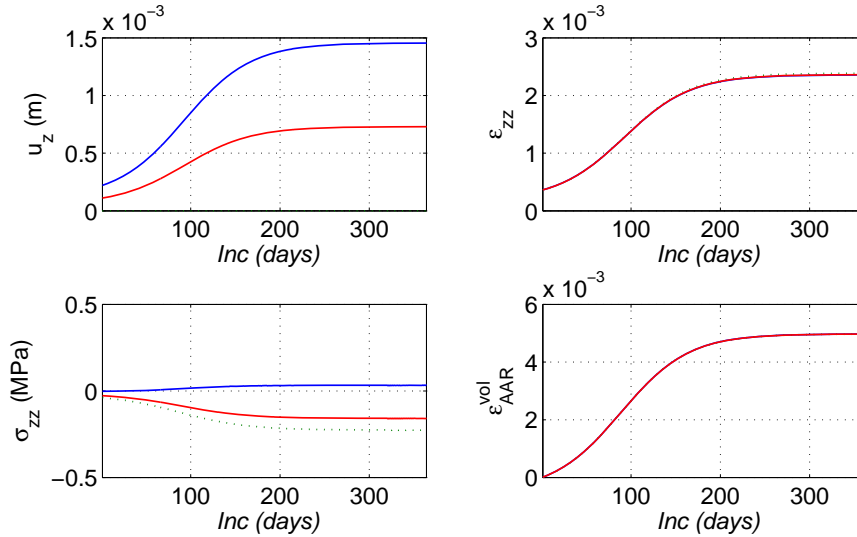


Fig. 2.39. Response of the beam B3 at three index points; Under ASR expansion

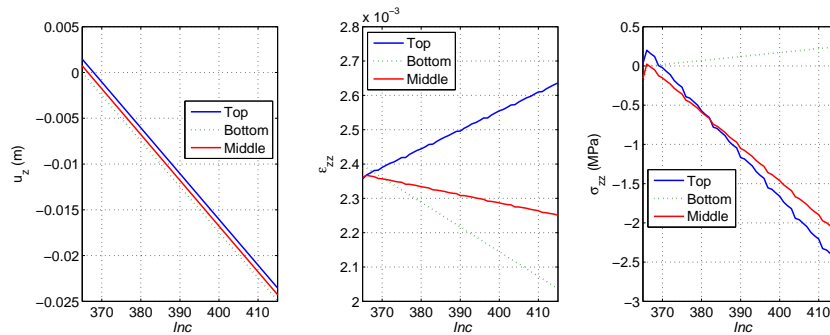


Fig. 2.40. Response of ASR-affected beam B3 at three index points; Under incremental displacement

Figures 2.41 and 2.42 show the stresses at the two index rebars under the ASR expansion and incremental displacement, respectively. The plot of rebar stress are only shown for selected increments (for ASR expansion $Inc = 1:50:365$ and for incremental displacement $Inc = 366:10:415$).

Based on figure 2.41 ASR expansion increases the tensile stresses. Considering that the no confinement is applied in this model and also the fact that there is a full bond between the concrete and steel rebars, any ASR-induced expansion leads to tension in the longitudinal reinforcements. Based on this figure, the beam experience considerable tension up to $Inc = 200$. The rate of the changes from $Inc = 200$

to $\text{Inc} = 365$ is negligible.

There are some localized high tensile stresses in the location of the support points. However, its effect is much palpable for bottom reinforcement than the top one. Based on figure 2.41, the stress in reinforcements almost reach to the yield strength of the steel at the end of ASR expansion. The average tensile stress in the rebars at the end of ASR expansion is about 250 MPa (for stress localized area this value is about 260 MPa). This means that the ASR-affected beam is highly vulnerable under any external load.

Based on figure 2.42 applying the incremental displacement increases the tensile stresses in middle section of the bottom rebar (between the support points). However, it decreases the tensile stresses for the top rebar. Thus, it means that for beam model B3, the incremental displacement plays a favorable role for the top rebars. The tensile stress reaches to +275 MPa, steel yield strength, at the increment $\text{Inc} = 370$ in the bottom rebar. This increment corresponds to vertical displacement of 0.0025 m. This figure clearly shows that the beam first fails at the bottom rebar. Compared to the figure 2.37, it can be concluded that the neglecting the confinement effect highly reduce the shear capacity of the beam and the bottom rebars fail under the smaller applied load.

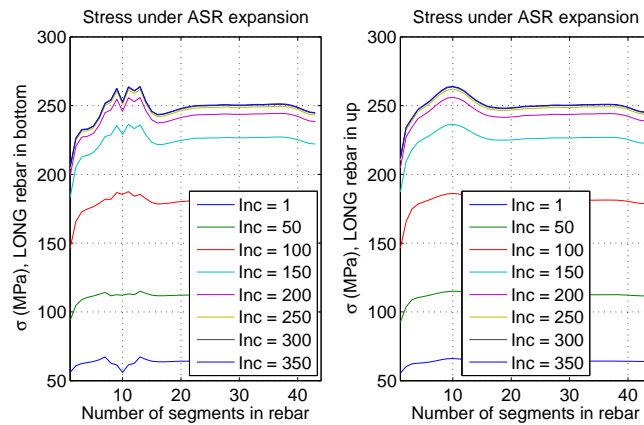


Fig. 2.41. Stress at the two index longitudinal rebars for beam B3; Under ASR expansion

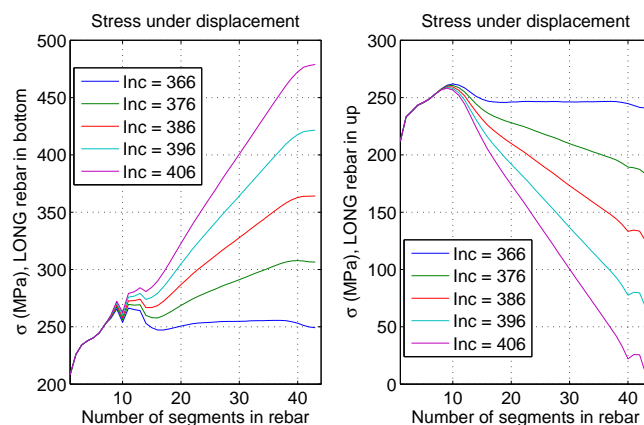


Fig. 2.42. Stress at the two index longitudinal rebars for beam B3; Under incremental displacement

2.3.2.4 Model B4

In this model only the incremental load (traction) is applied to the beam. ASR expansion is not considered. Both the concrete and steel are modeled with nonlinear behavior. The cracking in the concrete is modeled by smeared crack model. This is a benchmark model for further nonlinear analyses.

Figure 2.43 shows the response of the considered beam at three index points. The responses are only shown in vertical direction (z -direction). All the responses are shown up to one increment before failure. As seen, the vertical displacement (u_z) has nonlinear trend for three index points. There is no differences among all three index points. At the beginning, all the lines have a mild slope and cracking of beam make the slope very steep specially at the end increments.

The ϵ_{zz} shows also nonlinear behavior. However, it still has decreasing trend in the bottom and middle points (Index-3 and Index-2) and increasing trend for the top point (Index-1). This is similar to that observed for the linear model (figure 2.32).

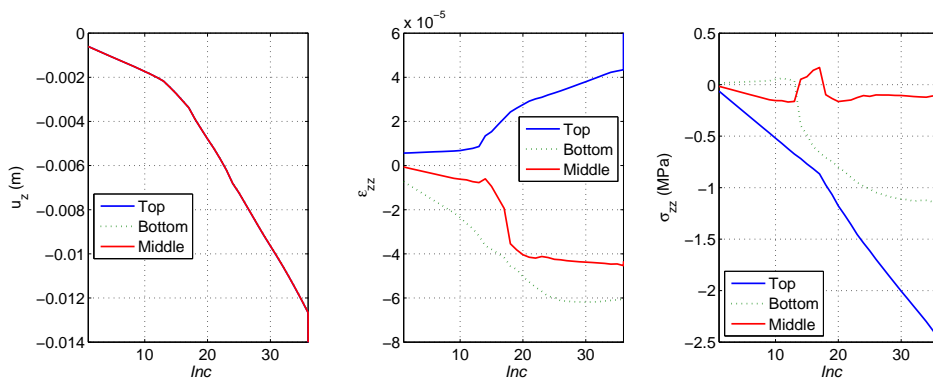


Fig. 2.43. Response of the beam B4 at three index points; Incremental load (traction)

Figure 2.44 shows the stresses at the two index rebars (as marked in figure 2.29) under the incremental load (traction). Based on this figure applying the incremental load (traction) increases the tensile stresses in the bottom rebar (specially near the mid-span). Also, it increases the compressive stresses for the top rebar. The tensile stress reaches to 275 MPa, steel yield strength, at the increment $Inc = 37$ in the bottom rebar. At this increment, the reinforcement yields. It is noteworthy that the elastic-perfectly-plastic model is considered for the steel in the present report. This figure shows that the beam first fails at the bottom rebar in mid-span area.

Figure 2.44 shows the progressive failure of the beam model B4 under incremental load (traction). As seen, the cracking first starts at the $Inc = 13$ at the bottom of the mid-span. This set of cracks propagate upwards. Another set of cracks also generates in vicinity of the initial ones and they also propagate upwards. Under the increasing applied load the cracks also are created far from mid-span. The final crack profile of the beam is also shown in $Inc = 36$. At this increment, most of the beam is cracked in the thickness. The instantaneous opening of the cracks are also shown in this figure.

2.3.2.5 Model B5

This model is exactly like the beam Model B4; however, the reduced material properties are used for concrete. The original concrete properties are already provided in table 2.8. In the beam Model B5 the modulus of elasticity and tensile strength of concrete are reduced by 30%. The incremental load (traction)

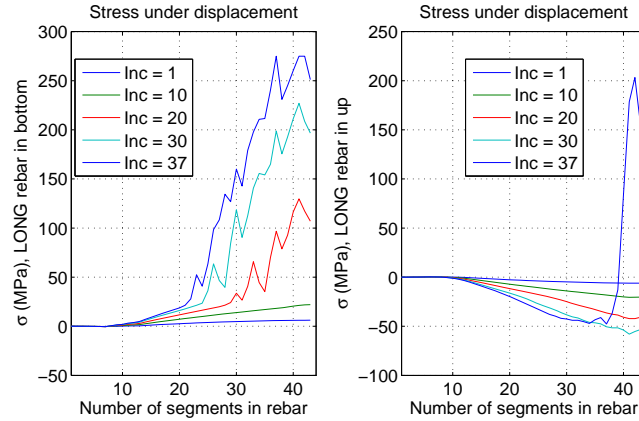


Fig. 2.44. Stress at the two index longitudinal rebars for half-beam B4; Under incremental load (traction)

is applied to the beam with the same protocol of the Model B4. ASR expansion is not considered. Both the concrete and steel are modeled with nonlinear behavior.

Figure 2.46 shows the response of the considered beam at three index points. The responses are only shown in vertical direction (z -direction). All the responses are shown up to one increment before failure. As seen, the vertical displacement (u_z) has nonlinear trend for three index points. Compared to the beam Model B4, the Model B5 fails at least one increments earlier (it means Model B4 fails under lower applied load (traction)). The ϵ_{zz} shows also nonlinear behavior. However, the general trend is the same for beam Model 4 and Model 5.

Figure 2.47 shows the stresses at the two index rebars (as marked in figure 2.29) under the incremental load (traction). Based on this figure applying the incremental load (traction) increases the tensile stresses in the bottom rebar (specially near the mid-span). Also, it increases the compressive stresses for the top rebar. The tensile stress reaches to 275 MPa, steel yield strength, at the increment Inc = 36 in the bottom rebar. At this increment, the reinforcement yields. The stress profile in beam Models 4 and 5 are very close to each other.

The progressive failure of the beam Model 5 is very similar to the Model 4 already shown in figure 2.44. However, as mentioned before, beam Model B5 fails one increment earlier.

2.3.2.6 Model B6

In this model, the side-walls are restricted in the direction perpendicular to the face. Thus, there will be no expansion in these directions. The beam is modeled considering the effect of yielding in the reinforcements. The concrete is modeled with the smeared crack model. It is noteworthy that in this model a 70% reduction fraction is applied for the Young's modulus and tensile strength at the end of ASR expansion and reported already in table 2.8 and shows also in figure 2.48.

Figures 2.49 and 2.50 shows the response of the considered beam at three index points showed in figure 2.29 under the ASR expansion and subsequently the incremental load (traction). The responses are only shown in vertical direction (z -direction). Based on this figure, the maximum vertical displacement of the Index-1 is more than Index-2. The Index-3 point has no vertical displacement at the end of ASR expansion, as the beam is rested on the ground at this point.

Figure 2.50 only shows the response of the ASR-affected beam under the incremental load (traction).

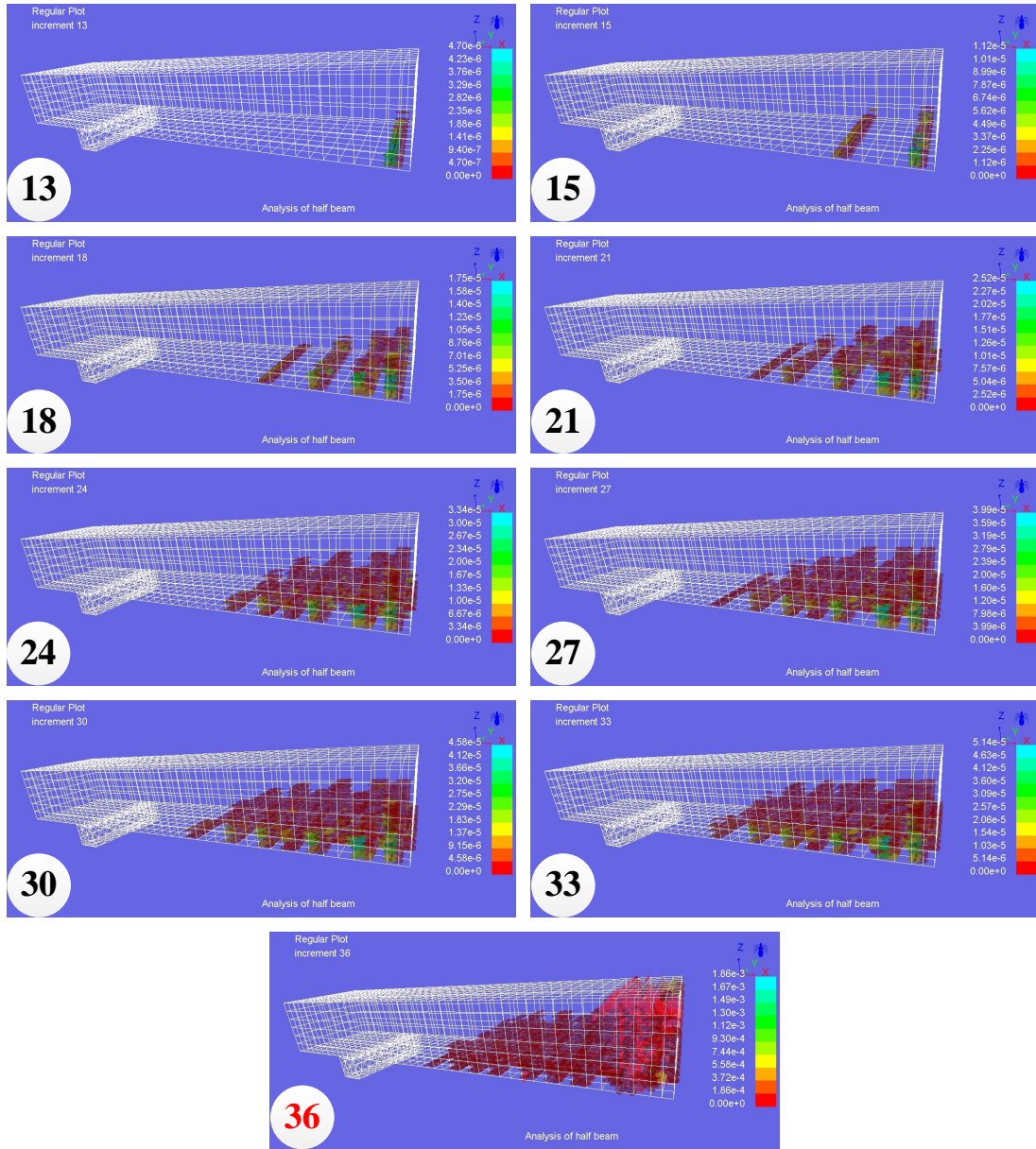


Fig. 2.45. Progressive failure in beam Model B4 under incremental load (traction)

As seen, the vertical displacement (u_z) has nonlinear trend in all three index points and finally it approaches to large values at the time of beam failure.

All the index points show almost the similar vertical strain (ϵ_{zz}) under the ASR expansion (Figure 2.49); however, there is a discontinuity in the time history of the strain curve when the loading type changes from ASR expansion to incremental traction (Figure 2.50). The ϵ_{zz} shows decreasing trend in the bottom and middle points (Index-3 and Index-2); however, it shows a nonlinear increasing trend for the top point (Index-1).

The vertical stress (σ_{zz}) plots for the three index points show negative values (meaning the index points

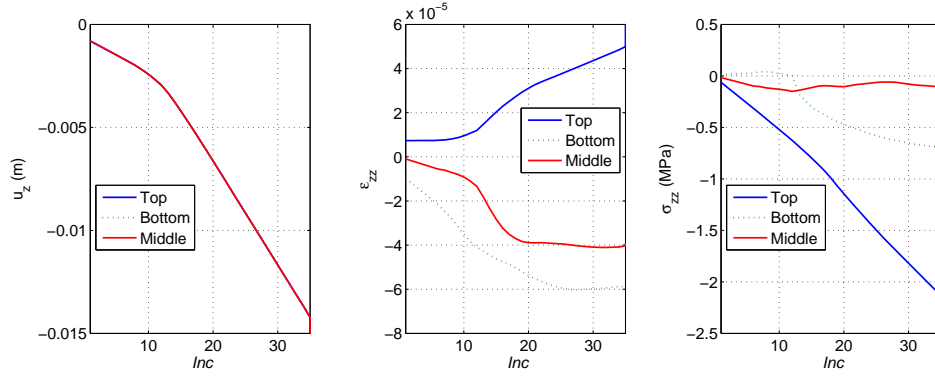


Fig. 2.46. Response of the beam B5 at three index points; Incremental load (traction)

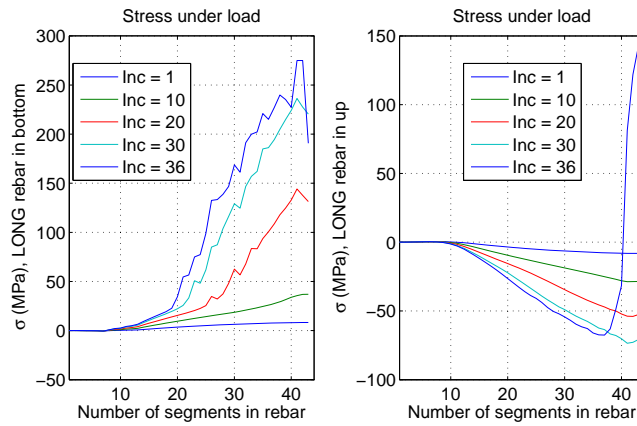


Fig. 2.47. Stress at the two index longitudinal rebars for half-beam B5; Under incremental load (traction)

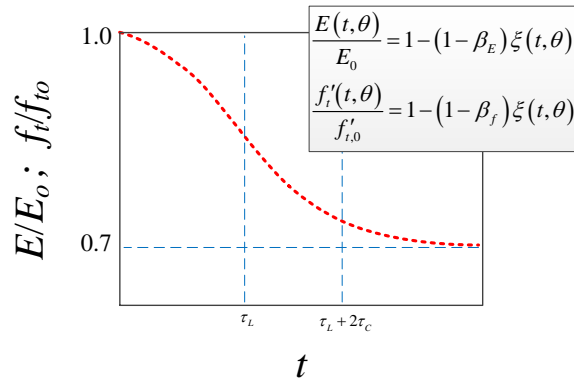


Fig. 2.48. Degradation of Young's modulus and tensile strength with ASR expansion

are under compression) up to the end of ASR expansion. However, compared to the model B2 with smooth stress curve (which is linear elastic version of B6) in figure 2.34, the Model B6 experiences extensive stress

fluctuations.

Finally, the volumetric AAR strain (ϵ_{AAR}^{vol}) reveals that none of the index points reach the maximum volumetric strain (ϵ_{AAR}^{∞}), 0.005, at the end of the analysis. The maximum expansion is about 0.0048 in all cases.

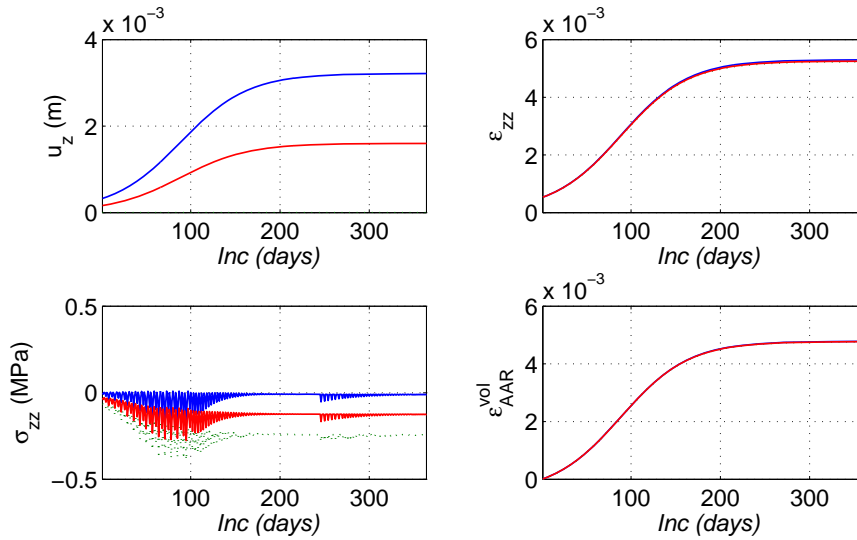


Fig. 2.49. Response of the beam B6 at three index points; Under ASR expansion

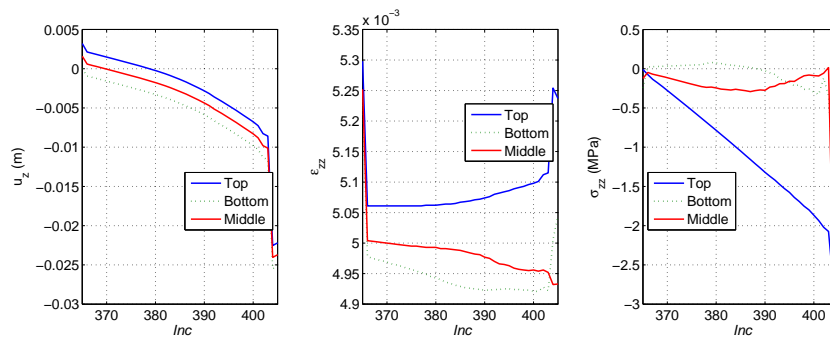


Fig. 2.50. Response of ASR-affected beam B6 at three index points; Under incremental load (traction)

Figures 2.51 and 2.52 show the stresses at the two index rebars under the ASR expansion and incremental load, respectively. The plot of rebar stress are only shown for selected increments (for ASR expansion $Inc = 1:50:365$ and for incremental load $Inc = 366:10:405$).

Based on figure 2.51 ASR expansion increases the stresses. The half-beam experiences tensile stresses in the area far from end point and mid-span. However, it has compressive stresses near the left-end and also mid-span. The value of the stresses under ASR expansion for beam Model B6 is about $[-2.2, +0.6]$ MPa which is less than the values reported already for linear elastic analysis $[-5.5, +1.5]$ MPa. It means that gradually degradation of the concrete material also affects on the steel stress.

Based on figure 2.52 applying the incremental load increases the tensile stresses in middle section of

the bottom rebar (between the support points). However, it increases the tensile stresses for the top rebar. Thus, it has a dual effect on the top and bottom rebars. The tensile stress reaches to +275 MPa, steel yield strength, at the increment Inc = 402 in the bottom rebar.

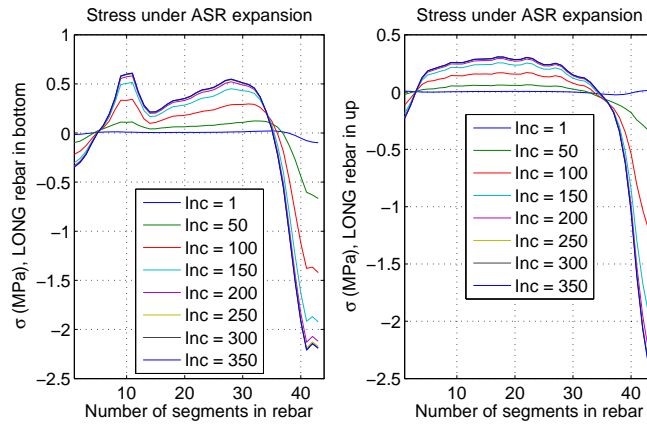


Fig. 2.51. Stress at the two index longitudinal rebars for beam B6; Under ASR expansion

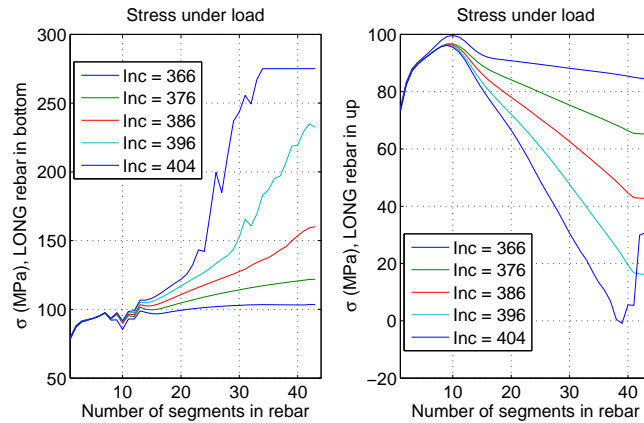


Fig. 2.52. Stress at the two index longitudinal rebars for beam B6; Under incremental load

The cracking pattern for the beam Model B6 is more or less similar to that reported already for the beam model B4. No direct cracking is generated under the ASR expansion in beam Model B6; however, it has an indirect effect on the degradation of the concrete material.

2.3.2.7 Model B7

In this model, all the side-walls (x-z plane and y-z plane) are free (see table 2.11). Thus, the expansion is allowed in perpendicular direction on these planes in addition to the parallel directions.

Figures 2.53 and 2.54 shows the response of the considered beam at three index points showed in figure 2.29 under the ASR expansion and subsequently the incremental load (traction). Based on this figure, the maximum vertical displacement of the Index-1 is more than Index-2. The Index-3 point has no vertical displacement at the end of ASR expansion.

Figure 2.54 only shows the response of the ASR-affected beam under the incremental load. All the three curves have a nonlinear trend; however, compared to the 2.50, the vertical displacements (u_z) have close values in the case of beam Model B7.

All the index points show almost the similar vertical strain (ϵ_{zz}) and the volumetric AAR strain (ϵ_{AAR}^{vol}) under the ASR expansion.

The vertical stress (σ_{zz}) plots for the index points under ASR expansion have extensive fluctuation, similar to that reported already for the beam Model B6. However, beam Model B7 experiences a bit larger stresses.

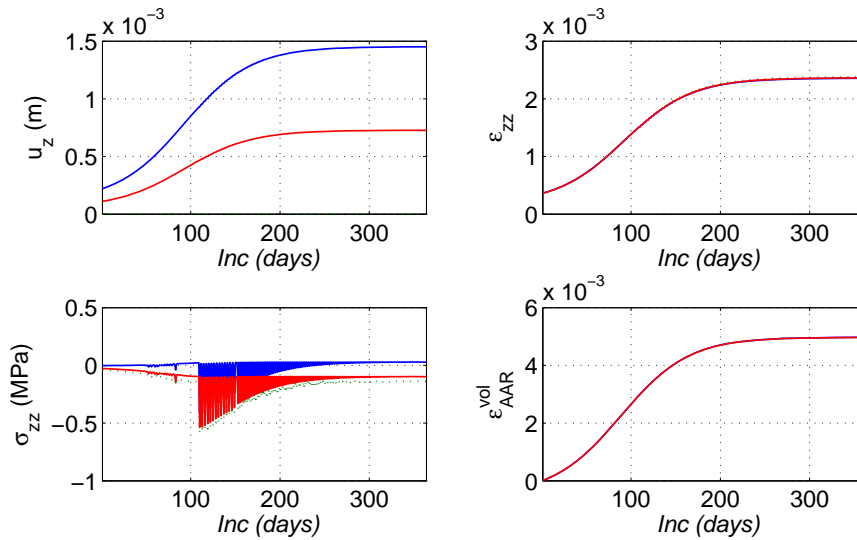


Fig. 2.53. Response of the beam B7 at three index points; Under ASR expansion

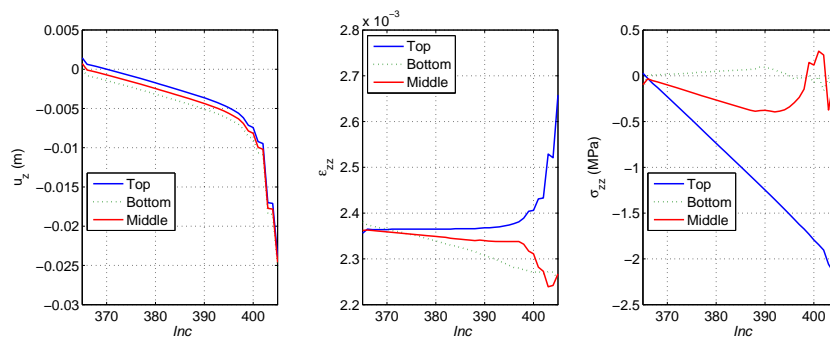


Fig. 2.54. Response of ASR-affected beam B7 at three index points; Under incremental load (traction)

Figures 2.55 and 2.56 show the stresses at the two index rebars under the ASR expansion and incremental load (traction), respectively. The plot of rebar stress are only shown for selected increments (for ASR expansion Inc = 1:50:365 and for incremental load Inc = 366:10:405).

Based on figure 2.55 ASR expansion increases the tensile stresses. Considering that no confinement is applied in this model and also the fact that there is a full bond between the concrete and steel rebars, any

ASR-induced expansion leads to high tensile stresses in the longitudinal reinforcements. Based on this figure, the beam experience considerable tension up to Inc = 250. The rate of the changes from Inc = 250 to Inc = 365 is negligible.

There are some localized high tensile stresses in the location of the support points. However, its effect is much palpable for bottom reinforcement than the top one. Based on figure 2.55, the stress in reinforcements almost reach to the yield strength of the steel at the end of ASR expansion. The average tensile stress in the rebars at the end of ASR expansion is about 250 MPa (for stress localized area this value is about 265 MPa). This means that the ASR-affected beam is highly vulnerable under any external load.

Based on figure 2.56, applying the incremental load increases the tensile stresses in middle section of the bottom rebar (between the support points). However, it decreases the tensile stresses for the top rebar. Thus, it means that for beam model B7, the incremental load (traction) plays a favorable role for the top rebars. The tensile stress reaches to +275 MPa, steel yield strength, at the increment Inc = 369 in the bottom rebar. For all the next increments the yielding in the bottom rebar propagates from the middle section toward the support. At the Inc = 404, about half of the half of the longitudinal reinforcements yield.

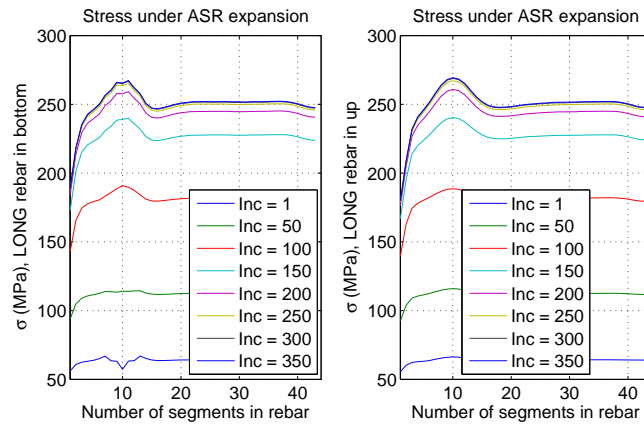


Fig. 2.55. Stress at the two index longitudinal rebars for beam B7; Under ASR expansion

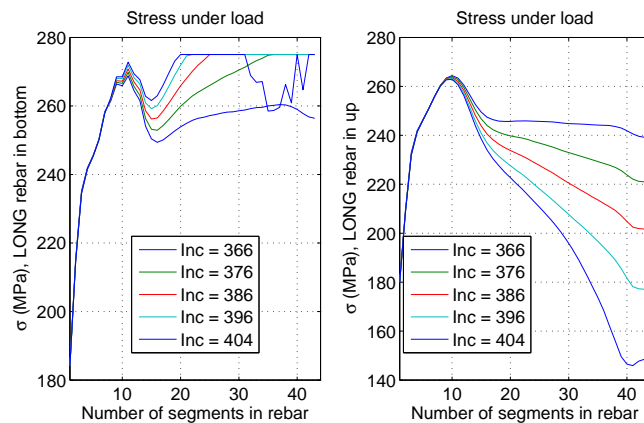


Fig. 2.56. Stress at the two index longitudinal rebars for beam B7; Under incremental load (traction)

2.3.2.8 Observations

Seven different models of a reinforcement beam were compared as reported in table 2.11. The aim of this section is to compare the shear capacity of a RC beam when it is subjected to the ASR expansion.

Linear elastic models were first studied in order to make sure about the accuracy of the finite element model, method of analysis, and to provide a bench-marking for those researchers that does not have access to the nonlinear models.

First, the load-displacement curve is compared for four nonlinear models (B4, B5, B6 and B7) and then the other observations are summarized. It is noteworthy that the load-displacement for the linear elastic models (B1, B2 and B3) is not provided as they are not capable of providing the beam capacity.

Figure 2.57 shows the load-displacement curves for nonlinear beam models. Let us take the beam Model B4 (only incremental load and original material properties) as a reference one. As seen, reducing the material properties (more specifically modulus of elasticity and tensile strength) by 30% in beam Model B5 leads to decreasing the shear capacity of the beam.

The other options (gradually reducing the material properties as shown already in figure 2.48) are also tested in this report (Models B6 and B7). Both these models also reduce the shear capacity of the beam. However, their mechanism is different from Model B5.

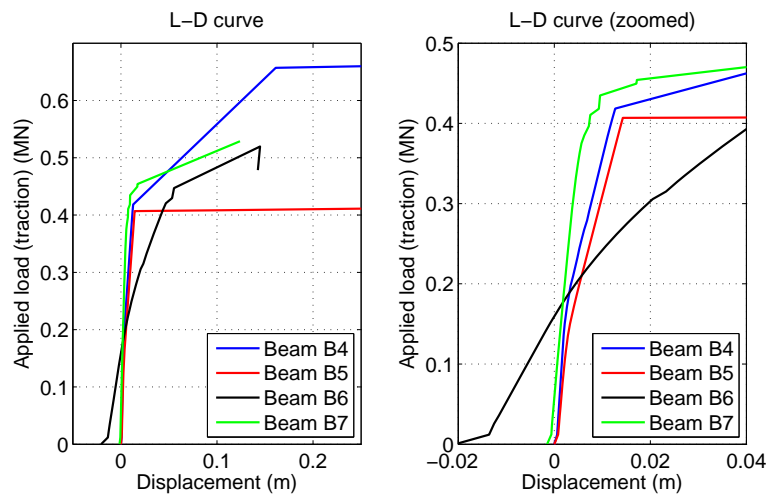


Fig. 2.57. Load-displacement curves for nonlinear beam models

Figure 2.58 shows the stress response of the central bottom rebar (the most critical one) at the first increment of applied load (traction) and also at the yielding increment respectively. The yielding increment is referred to the increments at which the rebar first reaches to the steel yield stress (+275 MPa).

Based on this figure, the beam Models B4 and B5 (those two without initial ASR expansion) has almost no tension at the first increment; while initial ASR expansion generates considerable tension in the rebars (Models B6 and B7). In the beam Model B7 (without confinement effect), the stress in the bottom rebar at the ASR expansion is very close to the steel yield stress. It means that any even small applied load can lead to rebar yielding in this model.

Also this figure shows that under the same protocol, the rebar in beam Model B7 yields earlier (at Inc = 8). Beam Models B5 and B6 yield at the almost same increment; however, the tensile stress along the rebar for beam Model B6 is higher than the beam Model B5.

This figure clearly shows that the assumption of: “reducing material property by 70% instead of applying the real mechanism of the ASR expansion” in a RC beam, can not be a perfect idea.

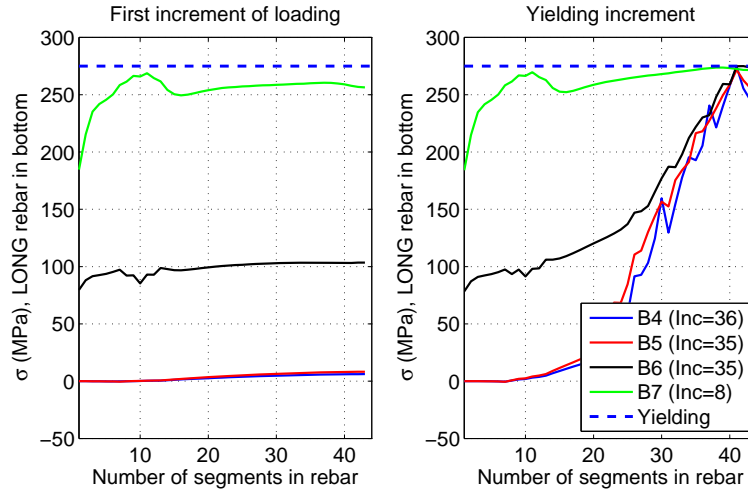


Fig. 2.58. Stress distribution in bottom rebar for nonlinear models

In addition, figure 2.59 shows the same plots of figure 2.58 but for the central top rebar. As seen, the ASR expansion has inverse effect on the top rebars. It means that it moderates the effect of the later applied load.

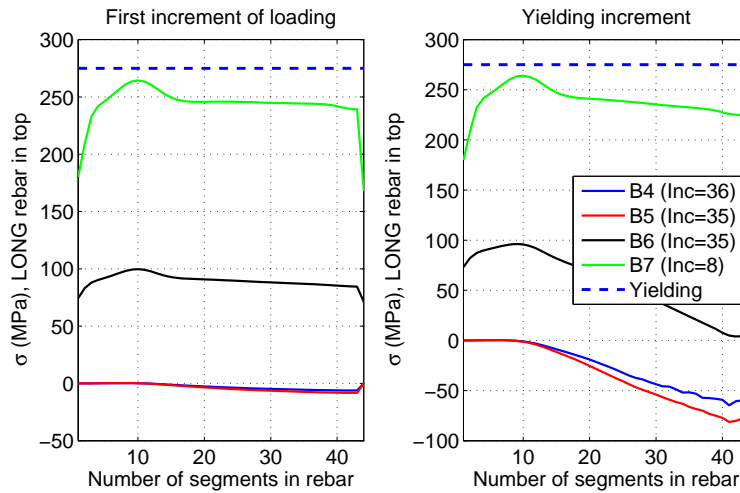


Fig. 2.59. Stress distribution in top rebar for nonlinear models

Bibliography

- Ababneh, A., Benboudjema, F. and Xi, Y.: 2002, Chloride penetration in non-saturated concrete, *ASCE Journal of Materials in Civil Engineering (in Press)* .
- ASCE: 1992, *Structural Fire Protection*, ASCE Committee on Fire Protection, Structural Division, American Society of Civil Engineers, New York, NY, USA.
- Bažant, Z., Chern, J. and Thonguthai, W.: 1981, Finite element program for moisture and heat transfer in heated concrete, *Nuclear Engineering and Design* **68**, 61–70.
- Bažant, Z. and Thonguthai, W.: 1979, Pore pressure in heated concrete walls: theoretical prediction, *Magazine of Concrete Research* **31**, 67–76.
- Bazant, Z. and Najjar, L.: 1972, Nonlinear water diffusion in nonsaturated concrete, *Matériaux et Constructions* **5**(25), 3–20.
- Bazant, Z. and Thonguthai, W.: 1978, Pore pressures and drying of concrete at high temperature,, *Proc. ASCE* **104**, 1059–1079.
- Benoit, B., Marcus, M., Stephane, P. and Sabine, D.: 2012, Simulations of the thermo-hydro-mechanical behaviour of an annular reinforced concrete structure heated up to 200 °c, *Engineering Structures* **36**, 302–315.
- Christensen, R.: 1979, *Mechanics of Composite Materials*, Wiley Interscience, New York.
- Eurocode: 2004, *EN, 1992-1-2: Design of concrete structures. Part 1-2: general rules – structural fire design*, European Committee for Standardization, Brussels, Belgium.
- Holman, J.: 2010, *Heat Transfer*, McGraw-Hill, Inc, New York.
- Kim, K., Jeon, S., Kim, J. and Yang, S.: 2003, An experimental study on thermal conductivity of concrete, *Cement and Concrete Research* **33**, 363–371.
- Kodur, V., Wang, T. C. and Cheng, F. P.: 2004, Predicting the fire resistance behaviour of high strength concrete columns, *Cement and Concrete Composites* **26**(2), 141–153.
- Kreider, J. and Rabl, A.: 1994, *Heating and Cooling of Buildings*, McGraw-Hill, Inc, Hightstown, NJ.
- Luikov, A.: 1975, Systems of differential equations of heat and mass transfer in capillary-porous bodies (review), *International Journal of Heat and Mass Transfer* **18**, 1–14.
- Mensi, R., Acker, P. and Attolou, A.: 1988, Séchage du béton : analyse et modélisation, *Materials and structures* **21**, 3–10.

- Multon, S., Seignol, J.-F. and Toutlemonde, F.: 2003, Large girders subjected to alkali-silica reaction, *ACI Special Publication* **212**(20), 299–318.
- Multon, S., Seignol, J.-F. and Toutlemonde, F.: 2005, Structural behavior of concrete beams affected by alkali-silica reaction, *ACI Materials Journal* **102**(2), 67–76.
- Multon, S. and Toutlemonde, F.: 2006, Effect of applied stresses on alkali-silica reaction-induced expansions, *Cement and Concrete Research* **36**, 912–920.
- Ranc, G., Sercombe, J. and Rodrigues, S.: 2003, Comportement à haute température du béton de structure, *Revue française de Génie civil* **7**, 397–424.
- Rosenburg, D.: 1969, *Methods for Numerical Solutions of Partial Differential Equations*, American Elsevier Publishing Company, Inc, Newyork.
- Saouma, V. and Perotti, L.: 2006, Constitutive model for alkali-aggregate reactions, *ACI Materials Journal* **103**(3), 194–2002.
- Takatura, T., Ishikawa, T., Matsumoto, N., Mitsuki, S., Takiguchi, K. and Masuda, Y.: 2005, Investigation of the expanded value of turbine generator foundation affected by alkali-silica reaction, *Proceedings of the 18th International Conference on Structural Mechanics in Reactor Technology (SMIRT18)*, number SMIRT18-H03-7, Beijing, China, pp. 2061–2068.
- Tamsir, M. and Sivastava, K.: 2011, A semi-implicit finite-difference approach for two-dimensional coupled burgers equations, *International Journal of Scientific & Engineering Research* **2**(6), 1–6.
- Tariku, F., Kumaran, K. and Fazio, P.: 2010, Transient model for coupled heat, air and moisture transfer through multilayerd porous media, *International Journal of Heat and Mass Transfer* **53**, 3035–3044.
- Tcherner, J. and Aziz, T.: 2009, Effects of aar on seismic assessment of nuclear power plants for life extensions, *Proceedings of the 20th International Conference on Structural Mechanics in Reactor Technology (SMIRT 20)*, number SMIRT20-Division 7 Paper 1789., Espoo, Finland.
- Xi, Y.: 1995, A model for moisture capacities of composite materials - formulation, *Computational Materials Science* **4**, 65–77.
- Xi, Y., Bažant, Z. and Jennings, H.: 1994, Moisture diffusion in cementitious materials; adsorption isotherms, *J. of Advanced Cementitious Material* **1**, 248–257.
- Xi, Y., Bažant, Z., Molina, L. and Jennings, H.: 1994, Moisture diffusion in cementitious materials; moisture capacity and diffusivity, *J. of Advanced Cementitious Material* **1**, 258–266.
- Xi, Y., Willam, K. and Frangopol, D.: 2000, Multiscale modeling of interactive processes in concrete, *ASCE Journal of Engineering Mechanics* **126**(3), 258–265.